# Using SABRE in the Earth's Magnetic Field

**Ali Hassan Ali Alghamdi**

PhD

University of York

Psychology

February, 2017

# Abstract

This thesis investigates the use of SABRE as a hyperpolarisation method within the Earth's magnetic Field (EFNMR) and develops an EFNMR apparatus to optimise sensitivity, resolution and performance. A fundamental problem in NMR and MRI is the inherent low sensitivity of the techniques due to the nature of the normal spin distribution at room temperature and in currently available magnets.This Boltzmann distribution means that few nuclear magnetic moments contribute to the detected signal. Hyperpolarisation is a method used to counter this by enhancing the NMR signal. SABRE, a new hyperpolarisation method for creating a very skewed distribution in the population of spins in a substrate does so without changing its chemical structure and offers the potential to make measurements at lower concentrations previously thought possible. Moreover, this method achieves its novel spin distribution in low field, and therefore provides an opportunity to also detect signals in low field thus, obviating the need for a high field magnet for specific applications.

This project is concerned with the investigation and use of a low field magnetic resonance device to optimize the detection and imaging of nuclear spin from molecules that have been subject to SABRE hyperpolarisation. It includes the description of the background for the investigations, the creation of an optimal devices for imaging and detection as well as for a study of the optimization of hyperpolarisation for molecules that are of biological significance.

The thesis focuses on optimising the SABRE technique in the earth's magnetic field and the primary results show how the signal enhancement is affected by several factors such as the amplitude of the pre-polarisation field, its duration, and the flip angle of the excitation pulse. The relationship between signal enhancement and a range of dependencies such as the parahydrogen pressure in the test tube, the effect of multiple shakes of the sample and the possibility of achieving 2D imaging by using SABRE in the earth's field have been investigated.

The improvement of the hardware and the software of a purpose-built system employed to produce a versatile earth's field spectrometer is described. Therefore, instead of being limited to a hard excitation pulse it is possible to employ this new system to generate trains of sine excitation pulses. In particular it is possible to create long sequences of, differing, arbitrary shapes (composite pulses).

The observations shown in the final chapter highlight the efforts made to progress the SABRE technique into advanced measurements in the earth's magnetic field such as polarising the sample in one place and performing the excitation/detection in another location. In addition, dedicated measurements were done to observe the long lived states of Aminothiazole and Fluoropyridine in the earth's magnetic field. However, these initial studies did not reveal evidence of a long-lived states, but a proposed plan to complete the long-lived SABRE measurement is given as future work.

# Contents


Abstract . . . . . 2

Contents . . . . . 3

List of tables . . . . . 7

List of figures . . . . . 8

List of symbols . . . . . 19

Acknowledgement . . . . . 20

Declaration . . . . . 22

**1 Introduction** **23**

1.1 Aims and objectives . . . . . 27

**2 Nuclear Magnetic Resonance** **29**

2.1 Nuclear spin . . . . . 29

2.1.1 Alignment . . . . . 31

2.1.2 Precession . . . . . 33

2.1.3 Resonance . . . . . 34

2.1.4 Free Induction Decay (FID) . . . . . 35

2.1.5 $T_1$ recovery and $T_2$ decay . . . . . 36

2.1.6 Chemical shift . . . . . 37

2.1.7 Scalar coupling . . . . . 37

2.2 Gradients . . . . . 39
2.2.1 Slice selection . . . . . 40
2.2.2 Frequency encoding . . . . . 41
2.2.3 Phase encoding . . . . . 42
2.3 Pulse sequence . . . . . 43
2.3.1 Spin Echo (SE) sequence . . . . . 44
2.3.2 Gradient Echo (GE) sequence . . . . . 46
2.4 Encoding and image formation . . . . . 48
2.4.1 Introduction . . . . . 48
2.4.2 k-space description . . . . . 48
2.4.3 k-space filling . . . . . 49
2.4.4 Fast Fourier Transform (FFT) . . . . . 53
2.5 Signal enhancement using Hyperpolarisation methods . . . . . 54
2.5.1 Brute-force . . . . . 54
2.5.2 Optical Pumping . . . . . 56
2.5.3 Dynamic Nuclear polarization (DNP) . . . . . 58
2.6 Parahydrogen . . . . . 60
2.6.1 Parahydrogen Induced Polarization (PHIP) . . . . . 63
2.6.2 Signal Amplification By Reversible Exchange (SABRE) 67
2.7 Using parahydrogen *in-vivo* . . . . . 71
2.8 Catalyst . . . . . 72
2.9 Substrate (Pyrazine) . . . . . 73

**3 Earth's field NMR** **76**

3.1 Introduction . . . . . 76
3.2 Recent developments in low field and earth's field NMR . . . . 78

3.3 The low field apparatus . . . . . 91
3.3.1 Theoretical approach . . . . . 91
3.3.2 Design and operation . . . . . 92
3.4 Set up of the EFNMR instrument . . . . . 96
3.5 Homogeneity of earth magnetic field . . . . . 98
3.6 Optimising the Free Induction Decay (FID) . . . . . 99
3.6.1 Tuning the $B_1$ coil . . . . . 99
3.6.2 Shimming . . . . . 101

**4 Factors affecting SABRE signal enhancement in EFNMR 103**

4.1 Introduction . . . . . 103
4.2 Parahydrogen production . . . . . 105
4.3 Exploring the pyrazine signal enhancement from single shake and drop experiments . . . . . 106
4.3.1 Flip dependency . . . . . 108
4.3.2 Polarisation field dependency . . . . . 112
4.3.3 Parahydrogen in solution following a dissolving shake . 120
4.3.4 $^1$H NMR signal enhancement . . . . . 122
4.3.5 SABRE signal decay . . . . . 126
4.3.6 The effect of releasing parahydrogen from the test tube 127
4.3.7 The effect of multiple shakes of the sample . . . . . 129
4.3.8 The effect of heart tissue of a rat on the signal decay . . 131
4.3.9 Two dimensional imaging . . . . . 132
4.4 Conclusions . . . . . 134

**5 Automated pulse sequences in low field and SABRE 136**

5.1 Introduction . . . 136

5.2 Architecture and hardware . . . 139

5.2.1 Agilent U2353A . . . 139

5.2.2 Transmitting the excitation pulse . . . 142

5.3 Software and Processing . . . 149

5.4 Experiments to optimise NMR signal using Automated EFNMR system . . . 152

5.4.1 Tailored transmit pulse for earth's field NMR/MRI . . . 152

5.4.2 Flip angle calibration . . . 158

5.4.3 Preamplifier Gain . . . 160

5.4.4 Signal Averaging . . . 161

5.4.5 Sample size . . . 163

5.4.6 Signal dependence on position inside polarisation and detection coils . . . 164

5.5 Conclusions . . . 165

**6 Advanced SABRE measurements in the earth's magnetic field 167**

6.1 Introduction . . . 167

6.2 Probing SABRE using an NMR flow system . . . 168

6.2.1 results . . . 170

6.3 Long-lived states to sustain SABRE in earth's magnetic field . 171

6.3.1 Observing long lived states of Aminothiazole in the earth's magnetic field . . . 174

6.3.2 Investigating long lived states of 3-Fluoropyridine in the earth's magnetic field . . . 177

6.4 Discussion and future work . . . 182

6.5 Conclusions . . . 183

**7 Conclusions and future work** **184**

7.1 Conclusions . . . . . 184

7.2 Future work . . . . . 186

.1 Appendix A. Python codes . . . . . 187

.1.1 The code to run the singlet to magnetisation experiment 187

.1.2 Analytical solution field along the axis of the B1 coil . 199

Glossary . . . . . 201

Bibliography . . . . . 203

# List of Tables

2.1 This table compares the polarization of selected nuclei in different magnetic field and temperatures. P1 is polarisation number one and P1 is polarisation number 2. Table from [Månsson, 2002]. 55

2.2 This table shows how the the amount of parahydrogen increases as the temperature decreases. Taken from [Adams et al., 2009b]. 63

3.1 This table shows the ${T_1}^{\mathrm{B0}}$ and ${T_1}^{\mathrm{Bp}}$ of different tissues. Data from [Inglis et al., 2013] . . . . . 81

3.2 Parameters of the typical coil from [Halse, 2006]. . . . . 93

4.1 Table comparing signal enhancements (per mole) of hyperpolarised samples compared to water at thermal equilibrium. . . . 124

# List of Figures

1.1 Signal amplitudes underlay thermal equilibrium and hyperpolarisation conditions. . . . . 26

2.1 Schematic representation of the nuclear and electronic magnetic momentum of an Atom. Image taken from [Levitt, 2008]. . . . 30

2.2 Schematic representation of the nuclear and electronic magnetic momentum of an Atom. Table from [Kraus Jr et al., 2014]. . . 31

2.3 Motions of the spinning particles before and after applying the magnetic field. . . . . 32

2.4 A representation of the satellites peak. . . . . 38

2.5 How gradient changes the magnetic field. . . . . 39

2.6 The difference between steep and shallow gradients. . . . . 40

2.7 Slice selection on X axis. . . . . 41

2.8 The frequency encoding. . . . . 42

2.9 The phase encoding. . . . . 43

2.10 Spin echo pulse sequence. . . . . 45

2.11 Gradient echo pulse sequence. . . . . 47

2.12 Example of k-space with phase and frequency data, image from [Westbrook and Roth, 2013]. . . . . 49

2.13 Characteristics of k space, image from [Westbrook and Roth, 2013]. 50

2.14 Phase matrix of k space, image from [Westbrook and Roth, 2013]. 51

2.15 Data points in frequency encoding, image from [Westbrook and Roth, 2013]. 52

2.16 Dynamic images acquired utilising a sliding window radial sequence (reference [Wild et al., 2003]). (a) Images from a healthy normal (128 views per frame) collected at equal intervals from the inhalation of 300 mL of 3-He polarized to 40%. The dynamic flow of the inhaled gas is clear down from the trachea to the lungs. (b) Dynamic time series collected from a patient with Chronic Obstructive Pulmonary Disease COPD demonstrating areas of ventilation obstruction specially in upper lobes and delayed emptying of gas in the left lower lobe, which may indicates an air trapping. image taken from reference [van Beek et al., 2004] . . . . . 57

2.17 This graph demonstrates the four spin combinations of dihydrogen split into two isomers of orthohydrogen and parahydrogen. The highlighted box refers to the lowest energy parahydrogen state. Image from (https://www.york.ac.uk/chym/parahydrogen/). 62

2.18 Rat images using 2.4 T field. a) Proton SE image with scan time of 5.40 min. b) Proton GE image with scan time of 5.40 sec. ) A $^{13}$C single-shot RARE image with 0.9 sec. The orange color represent the signal enhancement derived from $^{13}$C. Image taken from [Golman et al., 2001]. . . . . 64

2.19 The population models in case of two spin system of AX type (A) standard NMR spectrum (b) PASADENA (c) ALTADENA. Image taken from [Natterer and Bargon, 1997]. . . . . 66

2.20 Schematic representation of SABRE method in which polarisation transfers from parahydrogen to substrate without chemical incorporation of the molecules. Where the yellow color indicates the hyperpolarisation state. Image adapted from [Adams et al., 2009b]. 68

2.21 Schematic representation of the equatorial ligands in the octahedral complexes. $H_a$ and $H_b$ are the Hydrogen atoms derived from parahydrogen, $L_c$ is the substrate and $L_d$ is a second ligand. Image from reference [Adams et al., 2009b]. . . . . 69

2.22 The dependency of the longitudinal magnetisation and the mixing field in a model substrate containing a single spin. Image from [Adams et al., 2009b]. . . . . 71

2.23 The chemical structure of pyrazine which contains four hydrogen nuclei that are chemically equivalent. . . . . 74

2.24 The chemical structure of (a) Nicotinamide and (b) Aminothiazole. . . . . 74

3.1 (A) Free Induction Decay and (B) $^1$H spectra from water and frog tissues $B_p$ = 20 mT and $B_m$ = 10 $\mu$T, Averaged over 100 epochs is indicated. Image taken from [Matlachov et al., 2004]. 79

3.2 FID and spectra of $^1$H from water inside copper canister of 2 mm thickness using $B_p$ = 10 mT and $B_m$ = 2 $\mu$T, Averaged over 100 epochs. Image taken from [Matlachov et al., 2004]. . . 80

3.3 Experimental two dimensional COSY NMR spectra of a) Difluorobenzene and b) Trifluoroethanol. Both were observed at the range of audiofrequencies 2.28 kHz ($^{19}$F) labelled F, and 2.43 kHz ($^1$H) labelled H, while the cross peaks are indicated by x. The low frequency interference shown as streaks along $f_1$ Image taken from [Robinson et al., 2006]. . . . . 81

3.4 2D images of the brain tissue using CPMG sequence interleaved with an IR-CMPG sequence (D and E) with inversion recovery delays to generate a signal null for brain tissue. C and F are the result of A-B and D-E receptively while G= C-F. Image from [Inglis et al., 2013]. . . . . 82

3.5 Transient magnetic field $B_t$ after switching off the polarisation coil. $t$ represent the time after switching off the coil and $B_p$ is the polarising field measured at the center of the coil. Image taken from [Nieminen et al., 2011]. . . . . 83

3.6 $^{1}$H-NMR shows a signal to noise ratio of $1.6 \times 10^{3}$ in low field from 148 $\mu$ mol of Pyradine in 2 mM of catalyst using a 5.4 mT polarisation field. This shows that low concentration of analytes can be measured in a single acquisition. Image taken from [Hovener et al., 2014]. . . . . 84

3.7 Signal amplitudes from hyperpolarised pyridine in methanol-$d_4$ and ethanol, the transfer field $B_s$ varied from 0.5 to 22 mT. Where ($\times$ and $*$) are the signals detected at low magnetic field and ($\bigcirc$) are signals detected at 7 T. Image taken from [Hovener et al., 2014]. . . . . 85

3.8 NMR Amplitudes for [ $^{13}$C]-formic acid at zero-field. Firstly, the sample was prepolarised at 2 T and transported adiabatically into the zero field. Then, the magnetic field was applied along the z axis. (a) represents a square pulse of duration 1.0 ms; (b) illustrates a hyperbolic secant pulse of duration 100 ms, for adiabatic remagnetisation. Image from [Tayler et al., 2016] . . 86

3.9 Mixing field dependence of the spin states made for model complexes with different spin topologies. The relative signal intensities for the zero quantum coherences $ZQ_x$ and longitudinal two-spin order $\hat{R}_z\hat{T}_z$ are illustrated as a function of mixing field over the range 0 - 25 mT (a). The relative signal intensities for $\hat{R}_z$ and $\hat{T}_z$ are also demonstrated as a function of mixing field (b). Images from [Adams et al., 2009b]. . . . . 87

3.10 The resolution of magnetic field of different detectors Wire-wound resonant copper coil + RT amplifier (WCC), Printed (planar) resonant copper coil + RT ampl (PCC) Bare high-Tc rf SQUID (SQUID), WCC (w/o amplifier) + high-Tc rf SQUID (TSC1), High-Tc tape coil + high-Tc rf SQUID (TSC2)at different frequencies.Image taken from [Dong et al., 2010] . . . . . 88

3.11 Images show a comparison between different detection modalities (a) Noise (b) signal to noise ratio. . . . . 90

3.12 The Terranova-MRI Earth's Field Nuclear Magnetic Resonance (EFNMR) apparatus. Image from [Halse, 2006] . . . . . 92

3.13 The spectrometer and probe of the EFNMR system. Image from [Halse, 2006]. . . . . 96

3.14 The methods of connecting the cables of the probe . . . . . 97

3.15 (a) Using the compass to tilt the probe with the earth's magnetic field. (b) The best direction of the probe. . . . . 97

3.16 Illustrated is maps of magnetic flux density and directions . . 98

3.17 Signal from water sample as a result of incorrect tuning using 2 ms acquisition delay and 90 excitation pulse . . . . . 99

3.18 Plot indicates how the maximum of the sinc function and the centre of the sample peak coincide. Image from [Halse, 2006]. . 100

3.19 FID acquired for 5 seconds to show how the signal amplitude enhanced. Image from [Halse, 2006]. . . . . 100

3.20 The resultant FID, signal and signal integration of Autoshimming in different days . . . . . 102

4.1 Schematic representation of the parahydrogen generator used at the Hyperpolarisation Centre in the University of York. . . . 105

4.2 A picture of the in house developed parahydrogen generator used in this study. . . . . 106

4.3 The simple pulse and collect sequence. Image from [Halse, 2006] 107

4.4 Results showing the signal amplitude vs transmit gain from 0° to 360° for different molecules. Fitting a sinusoidal curve to the observed data showed a close agreement between the observed data and the fit line for water measured at thermal equilibrium. However, There is a clear deviation between observed data and sinusoidal line for the other three hyperpolarised samples. The deviation is at its maximum in the Aminothiazole sample while it is smaller for both pyrazine and nicotinamide. . . . . 110

4.5 A best sinusoidal line fitted to the observed data in the flip angle dependency experiments. . . . . 111

4.6 Four plots showing how the polarising field affects the $^{1}$H NMR signal amplitude observed from different molecules (water, nicotinamide , pyrazine and aminothiazole). The polarising field varied from 0 to 18.8 mT and data observed were compared. . . . 113

4.7 The effect of polarisation duration on signal intensity. . . . . 116

4.8 The calculated exponential decay of the signal in a function of time. It is clear that a larger amount of signal is consumed when using larger flip angles such as 90° and the signal decays faster than those derived from smaller flip angles 45° which are preserved for longer periods at greater levels. . . . . 118

4.9 The measured signal decays of the hyperpolarised sample in earth magnetic field using different flip angles with exponential decay fitting. There is close agreement between the calculated results in (figure 4.8) and the measured data. . . . . 119

4.10 The measured FID decays of the pyrazine at flip angles of 90°, 45° and 22.5° compared to water . . . . . 119

4.11 The log predicted decay of FIDs of pyrazine at flip angles of 90°, 45° and 22.5° compared to water. . . . . 120

4.12 Two plots showing the rate of parahydrogen loss following the shaking of the sample as a function of delay. . . . . 121

4.13 Two plots showing that applying the polarisation field for 60 s is not feasible in order to study the effect of polarisation loss immediately after shaking the sample because the process of loss occurs in a time much shorter than the optimal polarisation duration. . . . . 122

4.14 Four plots comparing 1H NMR signal enhancements of hyperpolarised (pyrazine, nicotinamde and aminothiazole) substrates to water at thermal equilibrium. . . . . 125

4.15 Signal decay from hyperpolarised pyrazine. . . . . 126

4.16 Signal decay of hyperpolarised pyrazine when the tube was opened after 2000 s. . . . . 128

4.17 Plot shows zoomed area where signal drops sharply due to releasing pressurised parahydrogen from the headspace of the test tube after 2000 s. . . . . 128

4.18 Signal decay from hyperpolarised pyrazine . . . . . 130

4.19 Signal decay from hyperpolarised pyrazine without shaking the sample. . . . . 131

4.20 Signal decay of heart tissue immersed in liquid hyperpolarisation sample. (a) with shaking the sample (b) without shaking. 132

4.21 Two dimensional imaging of SABRE in low magnetic field. . . 134

5.1 Purpose-built earth's field NMR transmite recieve system based on commercially available DAQ boards. . . . . 138

5.2 Functional block diagram of Agilent U2353. Image from (docs-europe.electrocomponents.com/webdocs/0d87/0900766b80d871b4.pdf)140

5.3 Positive and negative edges of trigger signals used for triggering the pulse sequence following the polarisation field. . . . . 142

5.4 The electronic schematic of a DAQ board (a) shows that pins arranged in the top and bottom are associated with different multifunction channels. The left part illustrates the Dsub connector which is used to offer a connection between the DAQ board and Agilent U2353 via a USB extension cable. The side view (b) shows the dimensions of the board. Image from (docs-europe.electrocomponents.com/webdocs/0d87/0900766b80d871b4.pdf). 143

5.5 The power supply device used to supply the two amplifiers used in the purposed-built system. . . . . 144

5.6 The design of the NPN transistor. . . . . 145

5.7 Electric amplifier circuit illustrates the path of transmit/received signal synchronised with control pulses. . . . . 146

5.8 Components and timing of the pulse sequence. . . . . 147

5.9 A schematic representation of (W171DIP) read relay. . . . . 148

5.10 Schematic representation of DAQ connection pins. Here, channel 502 of DAQ2 used as an output source for transmit production and channel 501 of DAQ1 used as a source for NMR signal input. Channel (AIO202) of DAQ2 was used as a pulse generator. Image from (docs-europe.electrocomponents.com/webdocs/0d87/0900766b80d871b4.pdf)

5.11 Comparison between frequency domain of Gaussian pulse (G) and Rectangular pulse (R), image from [Bauer et al., 1984]. . . 153

5.12 Numerical simulations of (a) Gaussian envelope transmit pulse and (b) signal after Fourier transformation (c) square envelope pulse and (d) signal after Fourier transformation. . . . . 155

5.13 Zoomed views of base lines of the square and Gaussian transmit pulses showing the difference between the size of side lobes. As the size of the lobes increases the pulse becomes less selective. 156

5.14 NMR signal as a function of transmit gain for rectangular and Gaussian pulses of 1.5 ms duration. . . . . 157

5.15 Flip dependency of (a) Water (rectangular envelope pulse) (b) Pyrazine using DAQ for transmit (Gaussian envelope pulse) and receiving. . . . . 159

5.16 NMR signal from water (blue) and hyperpolarised pyrazine (red) as a function of preamplifier gain. . . . . 160

5.17 Plots of NMR FID amplitude obtained from 500 ml of tap water as a function of the number of averages. . . . . 162

5.18 The effect of sample size on signal intensity. . . . . 164

5.19 Graph showing a high agreement between the calculated and measured $B_1$ efficiency. . . . . 165

6.1 Images show how the polarisation coil (a) is separated from the gradient and excitation coils (b). Here the polarising of the sample occurs in one place and the excitation and signal are collected in a different location . . . . . 169

6.2 Images show a comparison between the signal intensities of (a) water in thermal equilibrium and (b) hyperpolarised pyrazine using separated polarisation and excitation/detection coils. . . 171

6.3 Graphs demonstrating the $^{1}$H NMR signals of Aminothiazole at 400 MHz for (a) $^{1}$H NMR spectrum taken in a single shot at thermal equilibrium (b) a $S_0$ derived spectrum of Aminothiazole which is created and investigated 1 s later by the method of Levitt, (c) the relative 3a derived SABRE hyperpolarised Aminothiazole spectrum and (d) the $S_0$ state 1 s following it was created through SABRE and a spin-lock. image taken from [Olaru et al., 2016] . . . . . 173

6.4 (a) Hyperpolarised singlet order based NMR spectra as a function of spin-lock duration. (b) corresponding integrated values demonstrating the signal decay due to relaxation. The $T_{LLS}$ is 36.6 $\pm$ 4.2 s and $T_1$ is about 10 s for the same system according to the exponential fit of the data. image taken from [Roy et al., 2016b]. . . . . 174

6.5 Pulse sequence used to investigate the J-synchronization experiment.Image from [Roy et al., 2016a]. . . . . 175

6.6 Magnetisation to singlet M2S RF pulse sequence. The Python listing for composite pulse sequence will be in the Appendix in this thesis. . . . . 176

6.7 (a) $^{1}$H NMR based experimental spectra (b) expected signal amplitude with varying number of composite pulses while keeping $\tau$ at a constant value. Image from [Roy et al., 2016a]. . . . 176

6.8 Signal amplitude vs number of composite pulses . . . . . 177

6.9 A comparison between (a) 3-Fluoropyridine spectra and (b) water spectrum. . . . . 179

6.10 The M2S and S2M pulse sequence used to measure the singlet state lifetimes in a strongly coupled spin pair. Image from [Roy et al., 2016a]. . . . . 180

6.11 The M2S and M2S pulse sequence. All the components were fixed while the delay have been incremented from 100 ms to 2 s. 181

6.12 The effect of spin lock delay on the singlet state signal amplitude. 182

## List of symbols

| | |
|---|---|
| A | mass number ( sometimes refers to Amper) |
| E | energy |
| $B_0$ | External magnetic field |
| $B_1$ | Excitation pulse |
| $B_p$ | The polarisation field |
| $B_s$ | The transfer field |
| $\bar{h}$ | Planck's constant |
| I | Intensity (also refers to quantum spin number) |
| J | J-coupling |
| H | Hamiltonian |
| $H_Z$ | Hertz , cycles per second |
| L | Inductance |
| $\gamma$ | Gyromagnetic ratio |
| T | Tesla |
| $T_1$ | Spin-lattice relaxation time |
| $T_2$ | Spin-spin relaxation time |
| $T_2^*$ | Relaxation time due to spin spin interaction and inhomogeneity |
| M | Magnetisation |
| N | Number in a given population (such as number of spins) |
| P | Polarisation |
| $\psi$ | wavefunction |
| R | Resistance |
| $\infty$ | Infinity |
| $\pi$ | pi = 3.14 |
| $\delta$ | Chemical shift |
| $\sigma$ | Cross section |
| t | time |
| $\upsilon$ | Larmor frequency |

## Acknowledgement

Words are insufficient to express my gratitude to those great people who have been beside me throughout my journey toward the submission of this thesis. This thesis would not have been possible without their support. I would like to especially thank my parents for their unlimited support throughout my life.

I would like to thank my sponsor, The University of Tabuk and the Ministry of Higher Education in Saudi Arabia for granting me this opportunity and for covering all the study and living expenses for my family and I in Australia and the United Kingdom from 2009 until 2017.

I would like to express my sincere gratitude to my supervisor: Professor Gary Green for the endless support and guidance during my PhD and related research and for his priceless advice even with regards to my career after getting the PhD.

It was a great honour for me to work with a remarkable name in the field like him. His perpetual energy and enthusiasm in research motivated me in my studies. In addition, although he is a very important and busy person he was always accessible and willing to help whenever I needed him.

I also would like to deeply thank my co-supervisor Professor Simon Duckett for his incredible patience and his expertise in science helped me tremendously. I would like to thank my TAP members Professor Alex Wade and Doctor Alexandra Olaru for their insightful comments, suggestions and encouragements. My sincere thanks are also also expressed to the staff, post docs and students both in the York Neuroimaging Centre and in the York Centre of Hyperpolarisation in magnetic Resonance who gave me access to the research facilities. Without their support it would not be possible to have conducted this research.

My close Saudi friends also deserve special thanks for making my life easier away from my home country especially Sultan Alamri, Magbool Alelyani, Anwar Aljadaani , Swilem Alatawi, Jassas Alotaibi, Abdulrahman Alquait Khalid Alasmari and Abdullah Algarni. We did a lot together I will miss you

all.

I would like to thank my family who believed in me and in my work and for supporting me throughout my studies.

Finally, the biggest expression of deep gratitude is to my wife Khadijah Alghmadi for all the love and for standing beside me throughout my study. She has been my inspiration and motivation during the hardships of a PhD to improve my knowledge and move my study forward. I would like to thank my daughters Ruba and Joud for the good times we spend together.

## Declaration

I declare that this thesis is a presentation of original work and I am the sole author under the supervision of Professor Gary Green and Professor Simon Duckett. Where figures or tables or any passages in this thesis have been copied from other sources these are clearly identified by citation and reference. I also confirm that this work has not previously been presented for an award at this, or any other University. All sources are acknowledged as references.

# Chapter 1

# Introduction

MRI is a powerful non-ionising and non-invasive imaging technique. The use of MRI techniques in medicine provides clinicians with a valuable diagnostic tool for investigations of both anatomical and functional features associated with human disease. MRI is also a powerful research tool which provides a wide range of unique capabilities such as high resolution, localised spectroscopy in conjunction with isotropy specificity [Kraus Jr et al., 2014]. This thesis concerned with using the power of MRI by making it more sensitive in the earth's magnetic field using SABRE.

The NMR phenomenon which forms the basis of MRI was first reported in 1945 by Bloch and Purcell independently [Bloch, 1946, Purcell et al., 1946]. They were awarded the Nobel Prize in 1953 for their discoveries. Following the introduction of MRI imaging [Lauterbur et al., 1973], there has been a rapid expansion of MRI techniques in diagnostic medicine. When used clinically these techniques are known as MRI and MRS. However, there are many other applications outside the medical field including for example, anthropology [Kleinman, 1997], paleontology [Chhem and Brothwell, 2007], evolution [Falk and Gibson, 2001, Hopkins and Rilling, 2000], material analysis [Hennessy, 2005] and food quality analysis [Hills, 1995].

NMR and hence MRI, depend upon the ability to detect and measure signals that arise due to two fundamental properties of matter. These are that atoms, amongst other fundamental properties, demonstrate nuclear magnetism and nuclear spin. For spin half isotopes, $^{1}$H is the preferable nucleus

over many other active nuclei such as $^{13}C$, $^{15}N$ and $^{31}P$ for three important reasons. First, the abundance of $^{1}H$ is 100% [Eisenschmid et al., 1987]. Second, it has a high gyromagnetic ratio which makes it the easiest nuclear spin to be observed and third the concentration of molecules containing $^{1}H$ is very high in biological tissue. The reason these three factors are important is because NMR signal intensity is directly proportional to them [Bowers and Weitekamp, 1986]. Other nuclei of lower abundance, lower gyromagnetic ratio and possibly lower concentration produce smaller signals and are therefore hard to observe even with signal averaging to maximise the resultant signal to noise ratio [Eisenschmid et al., 1987].

Traditionally, MRI is based on the detection and analysis of a signal that is generated from nuclear spin angular momentum in a magnetic field at thermal equilibrium. Therefore, there is a further factor that also determines the size of the observed NMR signal. This is the distribution of the spin between these so called spin states. Spin half nuclei are distributed between spin up and spin down orientations and that can be visualised as a bulk property of the sample. The effects of thermal energy is given by $k_B T$, where T is the absolute temperature and $k_B$ represents the Boltzmann constant while the population distribution of the spin states is controlled by Boltzmann statistics [Green et al., 2012]. If for example, a spin half nuclei possesses magnetic states in thermal equilibrium in molecule with a magnetic field, there will be large thermal effects when compared to the energy difference between the two states, that is generated from the Zeeman splitting.

Because the NMR signal is related to the size of the bulk magnetisation associated with the population difference between these two states, a fundamental problem is the inherent low sensitivity associated with their detection. This is because at body temperature and in a clinical magnet, almost as many nuclei are in the spin up state as in the spin down state. This difference is precisely determined by Boltzmann statistics.

As we cannot change the temperature of the human body, the population difference of molecules is directly related to the applied magnetic field; hence the signal is stronger at higher magnetic fields. But moving from a 3 Tesla magnet to one at 7 Tesla only changes the observed signal strength by $(7/3)^2$

times [Green et al., 2012]. In standard clinical magnets the Boltzmann distribution is such that a very small proportion of the atoms contribute to the MRI signal. For example, in a magnetic field of 9.4 T at 300 K, they exist with a population difference of only 1 part in 31,000 for protons [Green et al., 2012].

To overcome this low sensitivity problem, the population difference needs to be increased. This may be done by a method known as hyperpolarisation [Leawoods et al., 2001] Figure 1.1. A hyperpolarisation methods can boost the NMR signal of liquid samples by several orders of magnitude above that seen at thermal equilibrium polarization. Hyperpolarisation therefore enables the investigations of less concentrated molecules and the acquisition of images from nuclei other than protons. In addition to applications such as vascular imaging and perfusion studies, hyperpolarised MRI has recently been employed in molecular imaging studies to investigate the distribution [Golman et al., 2003] and metabolism [Golman et al., 2006a, Golman et al., 2006b] of hyperpolarised substrates. For example, several *in-vivo* studies have investigated the conversion of hyperpolarised $^{13}$C-labeled and Pyruvate into its metabolic products [Golman et al., 2006a, Viale and Aime, 2010], this is important because increased lactate production is a major indicator of cancer [Koukourakis et al., 2005]. The first trial of this technique was already reported in the clinic [Nelson et al., 2012].

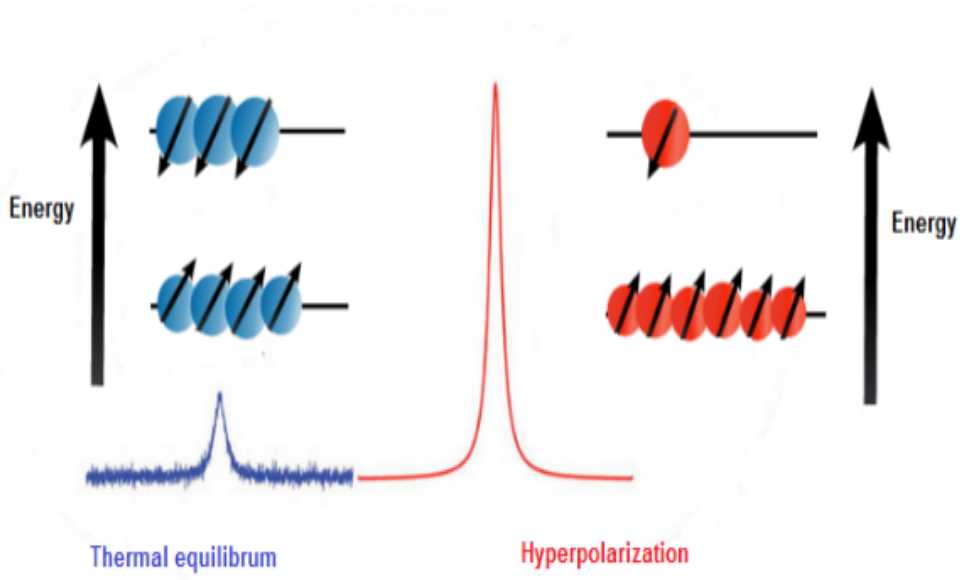


Figure 1.1: Signal amplitudes underlay thermal equilibrium and hyperpolarisation conditions.

Different hyperpolarisation methods have been used to boost the signal by increasing the population difference of the nuclear spin states from thermal equilibrium. These methods include brute-force [Månsson, 2002], Optical Nuclear Polarization [Prisner and Koeckenberger, 2008], DNP[Abragam and Goldman, 1978], NOE [Abragam and Goldman, 1978, Colpa et al., 1980, Hausser and Stehlik, 1968], Parahydrogen Induced Polarization (PHIP)[Pravica and Weitekamp, 1988] and Signal Amplification By Reversible Exchange (SABRE) [Ardenkjær-Larsen et al., 2003].

The SABRE means that a high field magnet is not necessary to create the spin distribution and may not be necessary for imaging. However, it might become more powerful for this method to supplement rather than replace conventional high-resolution MRI. This thesis describes the use of SABRE hyperpolarisation to prepare for the imaging of biological material in low field magnets.

The detection of nuclear precession in highly homogeneous earth's field was first demonstrated by Packard and Varian [Packard and Varian, 1954]. Many pioneering studies were conducted in the 1950s and 1960s [Brown and Thompson, 1961, Thompson et al., 1964a, Thompson and Brown, 1962, Thompson et al., 1964b,

Béné, 1967, Merck et al., 1967]. In the last few years, there has been a renewed interest in earth's field NMR due to many factors but most importantly the aim is to develop high resolution , reduced size, portable and low coast devices suitable for teaching and research purposes.

After setting out the main objectives and experimental sections of the thesis, I describe the physics of NMR and MRI; the basis of hyperpolarisation and the background to imaging in low fields in more details in the following chapters.

## 1.1 Aims and objectives

This study will focus on maximizing the use of SABRE approach in the earth's magnetic field for research purposes by developing this method from different aspects. The aims of this thesis are: 1) To investigate the major factors that enhance the SABRE sensitivity in the earth's magnetic field. 2) Develop the existing low filed NMR instrument to enhance the sensitivity of signal transmit and detection. 3) Designing and building a new and flexible pulse sequence system dedicated to detect different magnetisations rather than single spin in the current system. 4) Characterisation of the optimal conditions for polarisation transfer using SABRE in the earth's field.

PHIP is a common hyperpolarisation method in research showing a good signal enhancement several times greater than those of thermal equilibrium. However, this technique is restricted to limited number of biologically relevant molecules that characterized by the ability to accept $^{1}H$ and incorporate it into molecule and must be both unsaturated. Therefore, SABRE is a good solution to overcome this problem in which signal enhancement achieved without chemical incorporation of molecules. The idea of investigating the SABRE signal using low field NMR system is promising technique. Because the low field NMR provides a cheap , portable and more sensitive NMR imaging option.

In this thesis, chapter one has introduced a general idea about the need to use SABRE in the earth's magnetic field to overcome the inherent sensitivity problems in NMR. Chapter two, will present a fundamental principles of how does

MRI works from protons to image acquisition. Chapter three, will describe the commercially available Earth's Field Nuclear Magnetic Resonance (EFNMR) device (Magritek, Terranova, NZ) we use in our studies. This chapter explains step by step how this system works from finding the best homogeneous earth's field in the experiment room to running complex experiments.

Chapter four, will focus on investigating the effect of range of important factors on the signal enhancement including: flip angle, pulse duration, transmit gain, the field dependency, the polarisation duration, parahydrogen pressure. Optimal value of each factor will be defined to be used in further experiments to improve the quality of observed signals. In addition, chapter four will employ the optimal parameters determined in earlier to investigate different characteristics of SABRE process in the earth's field such as the decay time the enhanced signal takes to be destroyed completely, testing the effect of parahydrogen pressure inside the NMR test tube by opening the tube after a specific time, achieving multiple shakes of the sample a after fixed increments and a comparison between signal decay form pure liquid sample and sample that contains tissues of a rate heart.

Chapter five, will describe the instrumental developments by building a Data Acquisition system (DAQ) which includes a high performance ADC and DAC systems. This system can be controlled by python commands to run a complex and long experiments, visualise and analyse data automatically.

Chapter six, will describe an advance work by transporting the sample between the polarisation coil and excitation and detection coil in earth's magnetic field. The second part of chapter six will describe initial trials of measuring the long lived singlet state in the earth's magnetic field.

Finally, chapter seven will present the conclusions and the future work.

# Chapter 2

# Nuclear Magnetic Resonance

## 2.1 Nuclear spin

Atom consists of a positive nucleus located in its centre and negatively orbiting electrons. Nuclei are very small compared to the total size of the atom but contains most of its mass. This mass is the result of small particles called nucleons which consists of protons (positive) and neutrons (neutral). The number of electrons are usually the same as the number of protons, this makes the atom electrically neutral. The atomic number defines the chemical properties of the atom and is the sum of protons in the nucleus. The mass number is the total number of protons and neutrons which spin about their axes at the same rate but in opposite directions inside the nucleus. In some atoms, protons are more or slightly less in number than the neutrons which results in an odd mass number and therefore, the nuclei possesses a spin, denoted by quantum number I. This nuclear spin is completely quantum mechanical in origin and can be described in classical physics as rotating around its axis (angular momentum) see Figure 2.1.

However, nuclei with even mass number, are those where the number of protons and neutrons are equal , and half of their spins in particular direction and the other half in an opposite direction hence, they have a spin quantum number I=0 [Westbrook and Roth, 2013]. Nevertheless, if nuclei have an odd mass number, where the number of protons and neutrons is not equal, and they spin at a different rate in opposite directions, a net spin I in the nucleus can

be generated which then has angular momentum [Westbrook and Roth, 2013]. In addition, if the the number of neutrons and protons are both odd numbers, the spin is given by an integer number larger than zero. For example, $^{10}$B has I=3 and it has 5 neutrons and 5 protons.

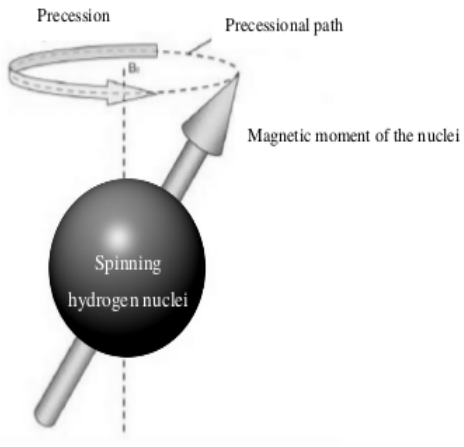


Figure 2.1: Schematic representation of the nuclear and electronic magnetic momentum of an Atom. Image taken from [Levitt, 2008].

The principles of MRI basically depend on the spinning motion of nuclei described by Faradays induction law which states that if two of three components (charge, motion and magnetization) are present the third is induced automatically. Therefore, when the positively charged nucleus spins it induces a magnetic moment $\mu$ that has a property of interacting with the external magnetic field. Those common nuclei described as NMR active nuclei, as shown in table 2.2 and find use in NMR and MRI studies.

| NUCLEUS | SPIN ($I$) | NATURAL ABUNDANCE (%) | BIOLOGICAL ABUNDANCE (% OF MASS) | $\gamma$ ($10^6$ RAD/T-SEC) | $\gamma/2\pi$ (MHz/T) | SENSITIVITY (REL. $^1$H) |
|---|---|---|---|---|---|---|
| $^1$H | ½ | 99.985 | 10. | 267.513 | 42.576 | 1 |
| $^2$H | 1 | 0.015 | 0.0015 | 41.065 | 6.536 | $9.65 \times 10^{-3}$ |
| $^3$He | ½ | 0.000138 | – | –203.78 | –32.434 | 0.44 |
| $^7$Li | 3/2 | 92.5 | $3 \times 10^{-6}$ | 103.96 | 16.546 | 0.29 |
| $^{13}$C | ½ | 1.10 | 0.198 | 67.263 | 10.705 | $1.59 \times 10^{-2}$ |
| $^{14}$N | 1 | 99.634 | 3.0 | 19.331 | 3.077 | $1.01 \times 10^{-3}$ |
| $^{15}$N | ½ | 0.366 | 0.011 | –27.116 | –4.316 | $1.04 \times 10^{-3}$ |
| $^{17}$O | 5/2 | 0.048 | 0.025 | –36.264 | –5.772 | $2.91 \times 10^{-2}$ |
| $^{19}$F | ½ | 100.0 | 0.004 | 251.66 | 40.053 | 0.834 |
| $^{23}$Na | 3/2 | 100.0 | 0.15 | 70.761 | 11.262 | $9.25 \times 10^{-2}$ |
| $^{31}$P | ½ | 100.0 | 1.0 | 108.29 | 17.235 | $6.63 \times 10^{-2}$ |
| $^{39}$K | 3/2 | 93.26 | 0.23 | 12.483 | 1.987 | $5.08 \times 10^{-4}$ |
| $^{43}$Ca | 7/2 | 0.135 | 0.002 | –18.001 | 2.865 | $6.40 \times 10^{-3}$ |
| $^{129}$Xe | ½ | 26.4 | – | –74.00 | –11.78 | $2.12 \times 10^{-2}$ |

Figure 2.2: Schematic representation of the nuclear and electronic magnetic momentum of an Atom. Table from [Kraus Jr et al., 2014].

The Hydrogen nucleus is the most common MR active nucleus that is used in clinical applications. This is because that it has a single positive proton that gives a large magnetic moment and more importantly, it is the most abundant atom in the biological tissue. These two characteristics give the advantage of utilising the maximum amount magnetisation in the body.

### 2.1.1 Alignment

The magnetic moment of these nuclei are distributed randomly in the absence of any magnetic field. When a strong magnetic field ($B_0$) applied, though the randomly distributed magnetic moments interact with this field. Some of these magnetic moments align parallel and others align antiparallel depending on their thermal energy Figure 2.3. Nuclei with low thermal energy do not possess sufficient energy to oppose the magnetic field so align parallel, however, nuclei with high thermal energy align antiparallel.

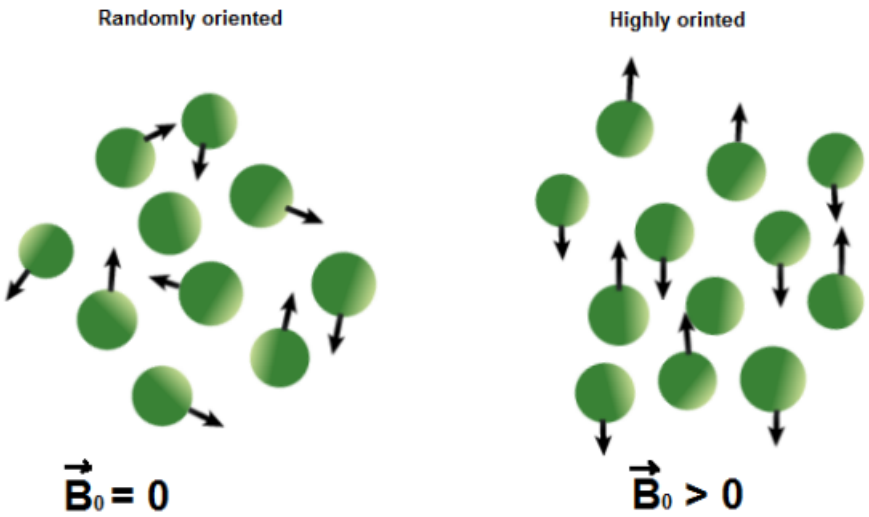


Figure 2.3: Motions of the spinning particles before and after applying the magnetic field.

The direction of alignment is determined by two factors, (i) the strength of the external magnetic field and, (ii) the level of thermal energy available to the nuclei. In thermal equilibrium, the number of nuclei with high energy are always fewer than those of low energy, therefore, those are larger numbers of nuclei aligned parallel to the applied magnetic field. This cancels the antiparallel aligned nuclei of opposite spin. It should be noticed that other NMR active nuclei rather than hydrogen nuclei align with the magnetic field producing small magnetic moments but are not used for clinical imaging as will be described in more details later in this chapter.

The number of energy levels for a given nucleus depends on the nuclear spin quantum number and equals to 2I + 1. For proton, where I= 1/2, two energy levels are available m=1/2 , and m= -1/2 with energy given by:

$$E_m = \gamma \hbar m B_0 \tag{2.1}$$

Where $\gamma$ represents the gyromagnetic ratio of the nuclei, $\hbar$ is Planck's constant divided by $2\pi$, $m$ is the magnetic quantum number and $B_0$ is the static magnetic field in Tesla. The population of each level is given by Boltzmann

statistics as in:

$$P = \frac{N_+ - N_-}{N_+ + N_-} = tanh\left(\frac{\gamma.\bar{h}.B_0}{2k.T}\right) \tag{2.2}$$

Where $N_m$is the number of nuclei in the $m$th state and N indicates the total number of spins, k is the Boltzmann constant and T denotes the absolute temperature. However, this magnetization cannot be measured until an excitation (RF) pulse is applied to tilt the magnetization toward the transverse axis perpendicular to $B_0$ allowing the manipulation of the polarisation. The manipulation of the spin orientation forms the basis of most MRI sequences in MRI and NMR.

It is clear from equation 2.2 that the amount of polarisation is inversely proportional to the temperature. Decreasing the temperature is limited by material applications and it is not possible when imaging biological living systems. In these conditions, it is only the magnetic field that determines the amount of magnetic moments aligned parallel or antiparallel. This leads to the fact that the initial magnetisation in low field are small. This can be compensated by using a stronger pre-polarising field and SQUID sensors instead of traditional Faraday pick up which is the core of our study.

### 2.1.2 Precession

Any rotating object has angular momentum which is a vector property. This vector defines the axis of the rotational motion and may point to any direction in space. Similarly, the spinning particles also have vectors that are distributed randomly in space in the absence of an external magnetic field [Westbrook and Roth, 2013]. these moving charges have the tendency to align with strong magnetic fields. Whenever an external magnetic field is applied to a spinning nucleus, it produces a spinning of the nucleus around $B_0$ in a circular path known as *precession*, and has a speed called the *precessional frequency* (in Hz). The spin polarisation rotates in the same precession with constant angle between the spin axis and the applied field [Westbrook and Roth, 2013].

The precessional frequency is governed by the Larmor equation which is given by:

$$\omega_0 = \gamma \times B_0 \tag{2.3}$$

This equation applies to every population of non-zero spin nuclei in any sample where $\omega_0$ denotes the precessional frequency, $\gamma$ is the gyromagnetic ratio and $B_0$ is the external magnetic field. The gyromagnetic ratio is the relationship between angular momentum and magnetic moment of specific nuclei and expressed in MHz/Tesla. The gyromagnetic ratio determines the polarisability for a nucleus. For example, the gyromagnetic ratio of Hydrogen is 42.57 MHz/T [Westbrook and Roth, 2013]. The amount of gyromagnetic ratio of given isotopes usually compared to that of protons to determine their sensitivity. Therefore, because there is a direct relationship between the gyromagnetic ratio and the precessional frequency, other nuclei will have different precessional frequencies as they have different gyromagnetic ratios. This makes it possible to specifically image hydrogen for example and ignore carbon in the body [Westbrook and Roth, 2013]. Most conventional MRI systems use tuned coils to excite and detect particular nuclear species at known magnetic field. Clinically, scanners typically tuned to detect the NMR signal from protons due to their high abundance in human body [Westbrook and Roth, 2013].

Interestingly, the gyromagnetic ratio is neglected when NMR signal measured in non- inductive coils such as SQUID because the response is frequency independent as will be described in more details in later chapters.

### 2.1.3 Resonance

When the precessing nuclei are exposed to an external RF pulse with the same frequency (Larmor frequency) which is perpendicular to $B_0$, these nuclei gain energy and resonate. Resonance occurs because the nuclei absorb energy from the RF leading to increase in the number of high energy population that align antiparalell. However, resonance does not occur if the RF pulse has a

different frequency. For example, for Hydrogen resonance to occur, the RF pulse must have energy of Larmor frequency of hydrogen. In this case, the applied RF pulse will not influence other MR active nuclei such as carbon or nitrogen because they have different precessional frequency. The process of applying RF pulse that cause nuclei to resonate called (excitation).

The energy difference between the two energy levels correspond to the energy needed to form resonance via excitation. That is to say, as the magnitude of the magnetic field increases, the energy difference between the two energy levels increases. This means, high energy (greater frequency) are required to to produce resonance.

### 2.1.4 Free Induction Decay (FID)

Resonance leads to a component known as the bulk magnetisation that moves away from the $B_0$ field toward the xy transverse axis. The angle at which the NMR tilted toward the transverse axis called the flip angle. the flip angle is dependent on the amplitude of the applied RF pulse and the duration at which it was applied. As the coherent transverse magnetization rotates at the Larmor frequency a voltage is induced in a coil which mounted in the xy axis. This causes a sinusoidal electrical signal based on Faraday's law called the Free Induction Decay (FID).

The magnitude of signal depends on the amount of magnetisation in the transverse axis. The optimal signal is measured when the magnetisation flips by 90 degree from the longitudinal axis. When the RF field is turned off it returns back to z axis under the influence of $B_0$ which is known as Relaxation. signal decreases with time under the effect of three factors. These factors are : (i) the magnetic moment is return back to equilibrium toward z axis (relaxation). (ii) the dephasing of the spin coherence as it rotates about the xy plan due to the small variations in the local magnetic field seen by each spin. 3) dephasing of the spin coherence due to the field inhomogeniety which are not recoverable.

### 2.1.5 $T_1$ recovery and $T_2$ decay

The process at which the magnetisation realigns gradually with the longitudinal $B_0$ field (recovery) makes decrease in transverse magnetisation (decay). During $T_1$ recovery the nuclei give up their energy to the surrounding (lattice) and the process is known as spin lattice relaxation. This recovery is exponential in nature, and has recovery time constant, termed $T_1$ . This is the time needed to re-establish 63% of the longitudinal magnetisation through recovery.

In contrast, the $T_2$ decay is caused by nuclei exchanging their energy with neighbouring nuclei. This exchange caused by the interaction of magnetic field each nucleus posses with its neighbours. It is called spin-spin relaxation and leads to loss of coherent transverse magnetisation. This also occurs at an exponential rate, and the time constant at which it decays called the $T_2$ relaxation time. This time is the period required to allow 63% of the transverse magnetisation to decay.

Different molecules possess different $T_1$ and $T_2$ values i.e. they are short in fat and long in water. In MRI, dedicated pulse sequences are used to exploit these differences to provide contrast. This can be done by employing a combination of RF pulses, signals and intervening delays. The main components of such a pulse sequences are :

1) The repetition time (TR), which is the time between the first 90° excitation pulse and the next 90° excitation pulse of the following sequence for each slice and is usually measured in milliseconds (ms). It is therefore defines the relaxation allowed between each two subsequent 90° excitation pulses, and hence, the $T_1$ relaxation occurred during reading the signal.

2) The echo time (TE), which is the time between the RF pulse and the maximum amplitude of the signal that is induced in the detection coil. It therefore encodes the amount of decay in the transverse axis and is set according to $T_2$.

### 2.1.6 Chemical shift

Hydrogen nuclei are present in different chemical molecules in the body (e.g water and fat). The precessional frequency of water and fat are slightly different due to the different in their chemical structures. The signal frequency in MRI is directly proportional to the local magnetic field, which has a contribution from $B_0$ as mentioned previously in section 2.1.2. It means that the NMR signal frequency increases with high magnetic fields and so does and difference due to the local effects. That is to say, in 1.5 T the prcessional frequency of water is about 220 Hz greater than that of fat. This difference decreases to about 147 Hz in the presence of magnetic field of 1 T.

However, this difference is only great in the presence of high magnetic fields, and decreases as the field decreases until it becomes almost ignored in very low field such as earth's magnetic field. This will be described in more details in this thesis.

### 2.1.7 Scalar coupling

Usually scalar coupling and J-coupling are used synonymously and reflect the indirect dipole-dipole coupling that is mediated by the chemical bond that connects two spins. However, J-coupling refers to the anisotropic and scalar coupling indicates the isotropic part of the bond. Scalar coupling therefore, describes the relationship between spins that mediated by electrons that effect bonds between nuclei. J-coupling is directly proportional to the gyromagnetic ratio of nuclei connected by bonds and the s-orbital overlap.

Practically, anisotropic coupling is hardly observable, because it only exists in aligned media and indistinguishable from the much stronger component of dipolar coupling. When abundant nuclei such as $^{1}H$ and rare nuclei $^{13}C$ are bound, there will be symmetrical peaks (called satellite signals) surrounding the dominant $^{1}H$ peak due to the coupling Figure 2.4.

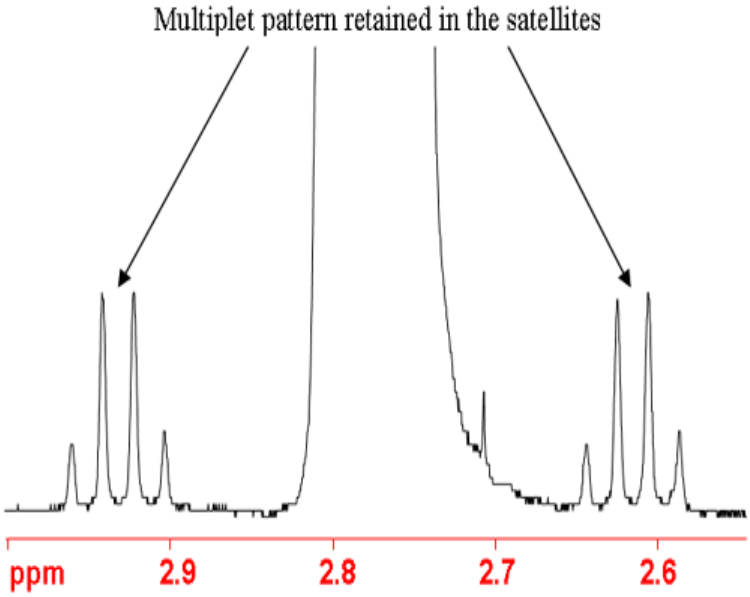


Figure 2.4: A representation of the satellites peak.

Magnetic interactions can transfer through J coupling in liquid state NMR. Several techniques such as Correlated Spectroscopy (COSY) and Total Correlated Spectroscopy (TOCSY) rely on this concept. However, a major limitation in observing J-coupling arises when one of the nuclei has a very fast relaxation such as $^{14}$N. For example, the coupling between $^{1}$H and $^{14}$N is not usually observable due to $^{14}$N's fast relaxation.

Magnetization transfer experiments in liquid state NMR are strongly dependent on scalar coupling, therefore, the sequences of these experiments require the introduction of a delay to exploit the dynamics of J-coupling evolution. The coupling is also related to the number of Hydrogens existed on neighbouring carbon atoms.

J-coupling can suppressed by a process known as decoupling, which can be used with heteronuclei or even in homonuclei to make the spectra simpler by using RF power for decoupling. For example, $^{13}$C spectra are usually studied with $^{1}$H decoupling. J-coupling requires low RF power for decoupling when compared to those needed for dipolar decoupling.

## 2.2 Gradients

MRI uses gradient fields which are superimposed on the $B_0$ field to cause a linear version of Larmor frequency with position in the sample as shown in Figure 2.5. Therefore the precessional frequency of nuclei located on a defined axis of the gradient changes relatively. This process is exploited in spatial encoding, Figure 2.5 shows that the magnetic field strength has been increased on one side (right) and has been decreased on the other side (left) of the coil. Nuclei on the left hand side will experience lower magnetic field so precess at a lower frequency. However, nuclei on the right hand side will experience a higher magnetic field and will have higher precessional frequency. The magnetic field in the centre of the gradients does not change hence, the precessional frequency at that point remain unaltered. Therefore, it becomes possible to locate the position of any nuclei according to their precessional frequency [Westbrook and Roth, 2013].

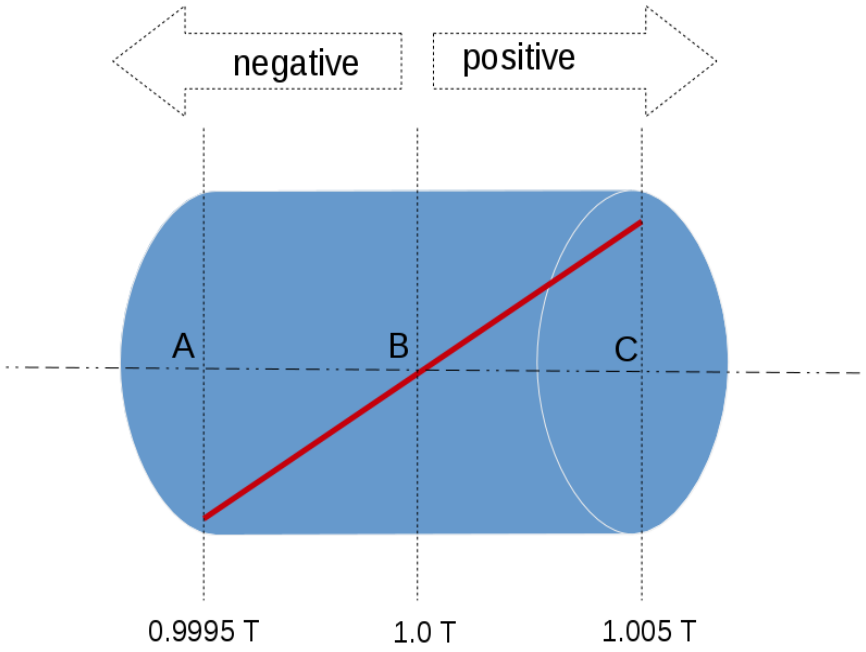


Figure 2.5: How gradient changes the magnetic field.

The slope of the gradient determines the magnetic field amplitude along the gradient axis. Steep gradients change the magnetic field significantly while

shallow gradients have slight influence on the magnetic field, Figure 2.6. Generally, gradients can be used to dephase or rephase the magnetic moments [Westbrook and Roth, 2013]. Additionally, they can be used to perform the spatial encoding process which usually consists of three processes as the following :

i) Slice selection: locating the position of a particular slice on a selected scan axis.

ii) Frequency encoding: locating the signal spatially along one axis of the volume.

ii) Phase encoding: locating the signal spatially orthogonal to the frequency axis of the volume [Westbrook and Roth, 2013].

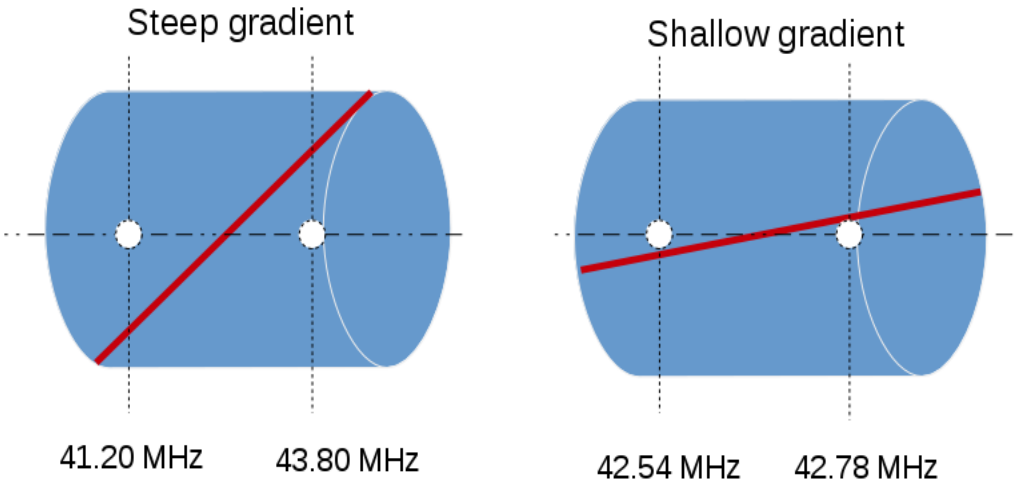


Figure 2.6: The difference between steep and shallow gradients.

### 2.2.1 Slice selection

When a slice selection gradients applied see Figure 2.7, the magnetic field and therefore the precessional frequency of nuclei along that axis alters. It means that before applying the gradient all slices have the same frequency but after the gradient has been applied each slice will have different frequency. The RF pulse now applied at the Larmor frequency equal the precessional frequency of the selected nuclei. Resonance therefore, occurs only to the selected nuclei while other nuclei that are located in other slices remain unaffected because

their frequencies do not match the frequency of the RF pulse.

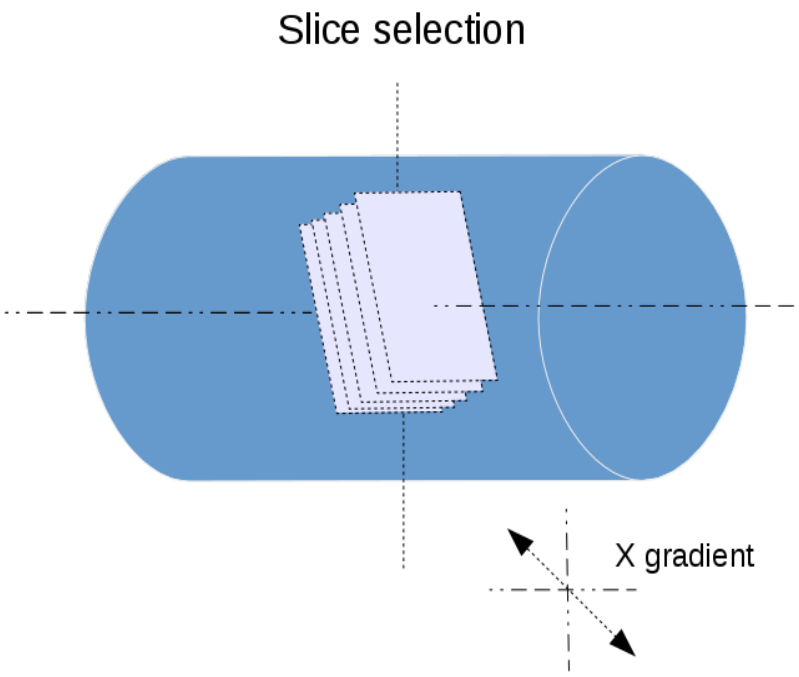


Figure 2.7: Slice selection on X axis.

### 2.2.2 Frequency encoding

When a particular slice has been selected, the next step is to locate the signal comes from this slice on both axes of the image. Locating the signal on particular axis is called frequency encoding. This is performed by applying a frequency encoding gradient, which will change the magnetic field linearly and therefore the precessional frequency of the nuclei located on its axis Figure2.8. The gradient lead to a frequency shift along the selected axis. This therefore makes it possible to locate the signal along the gradient axis based on it frequency.

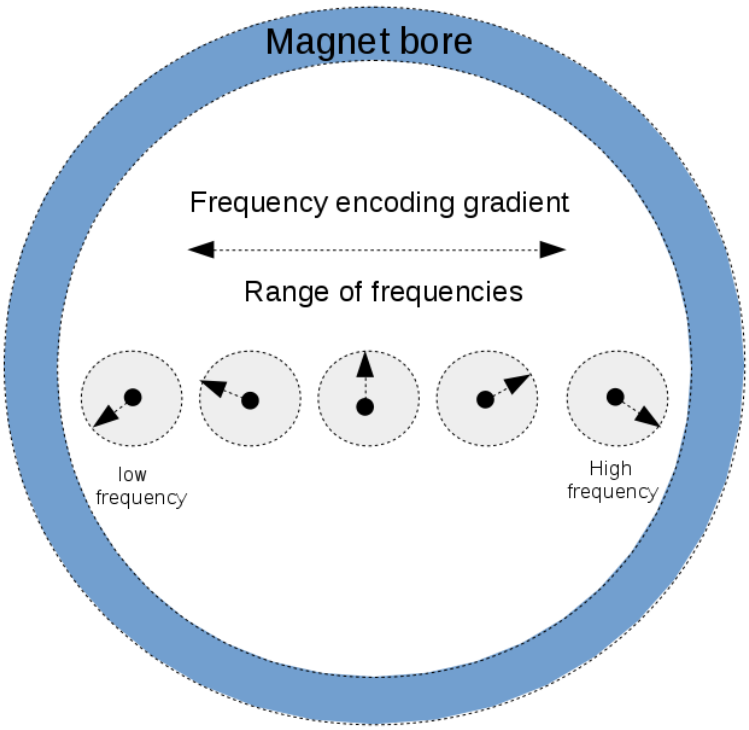


Figure 2.8: The frequency encoding.

The frequency encoding gradient turns on when the signal is received and it is also known as the readout gradient. The echo is usually centred in the middle of the frequency encoding gradient so it covers the rephasing and dephasing parts of the echo. The degree of gradient strength determines the size of the volume of interest covered along the frequency encoding axis during the imaging which known as the Field Of View (FOV).

### 2.2.3 Phase encoding

Once the slice has been selected, the signal coming from it has been located on one axis, the next step is to locate the second axis of this signal. This can be done by a process called phase encoding. It begins by switching on a phase encoding gradient which alters the magnetic field along its axis (orthogonal to frequency axis) and therefore, alters the precessional frequency of nuclei on this axis Figure 2.9. As the precessional frequency has changed, the phase of magnetic moments also changes on their precessional path. Nuclei that had

their speed increased due to the application of gradient move further around their precessional path than if there is no gradient. On the other hand, nuclei that had their speed decreased due to the application gradient move back around their precessional path than if there is no gradient.

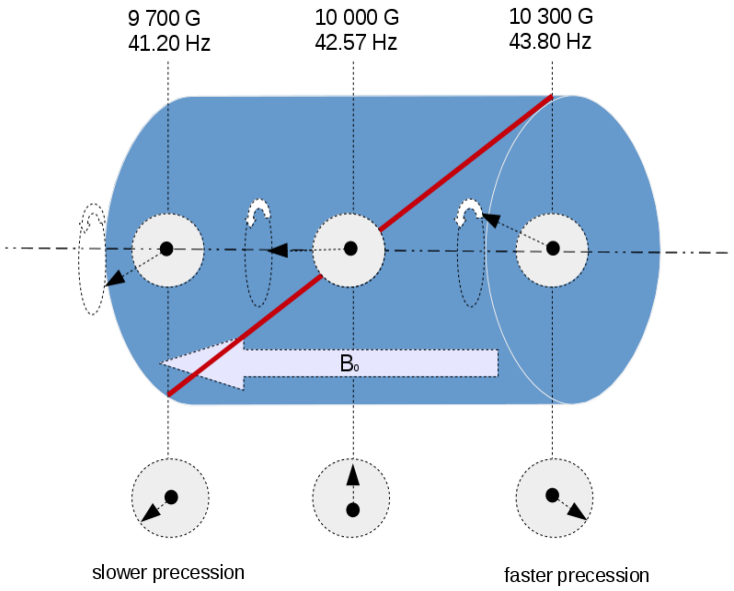


Figure 2.9: The phase encoding.

The phase encoding gradient usually turn on just before the 180 refocusing pulse in spin echo sequence. And the strength of its gradient determines the degree of which the phase between two points changes. To create a large phase shift between two points, a steep gradient is required but if a small shift is needed a shallow gradient can be applied.

## 2.3 Pulse sequence

In NMR and MRI, it is essential to understand the action of variety of pulse sequences. A pulse sequence is a range of RF pulses and gradients arranged in certain way to control the type of detected signal. Several pulse sequences are used in clinical research is designed according to the purpose of the required study. In this chapter, two pulse sequences will be discussed and their advantages and disadvantages described. These are the Spin Echo (SE)

sequence and Gradient Echo (GE) sequence.

### 2.3.1 Spin Echo (SE) sequence

The spin echo pulse sequence is the most common used pulse sequence and generally consists of a slice selective 90° RF pulse followed by one or more 180° refocusing pulses Figure2.10. In imaging, the 180° RF pulse refocuses the dephasing lost due to the local field inhomogeneity in addition to the lose of coherence caused by the application of a magnetic field gradient [Westbrook and Roth, 2013]. Slice selective (GS), phase encoding (GP) and frequency encoding (GF) are three gradients that are typically used in SE pulse sequence to spatially locate signals according to their frequencies only, not their time. The rephasing part of the slice selection gradient, the phase encoding gradient and the dephasing part of the readout gradient are applied simultaneously, after the 90° RF pulse. The phase encoding gradient is switched on just before the 180° pulse. The slope of the phase gradient determines the phase shift along the encoding axis [Westbrook and Roth, 2013]. The slice selection gradient that is applied with the 180° RF pulse does not need a rephasing. However, two similar gradient lobes applied to both sides of this gradient to exclude the transverse magnetisation built in by the 180° rephasing pulse form on the edge of the slice [Westbrook and Roth, 2013].

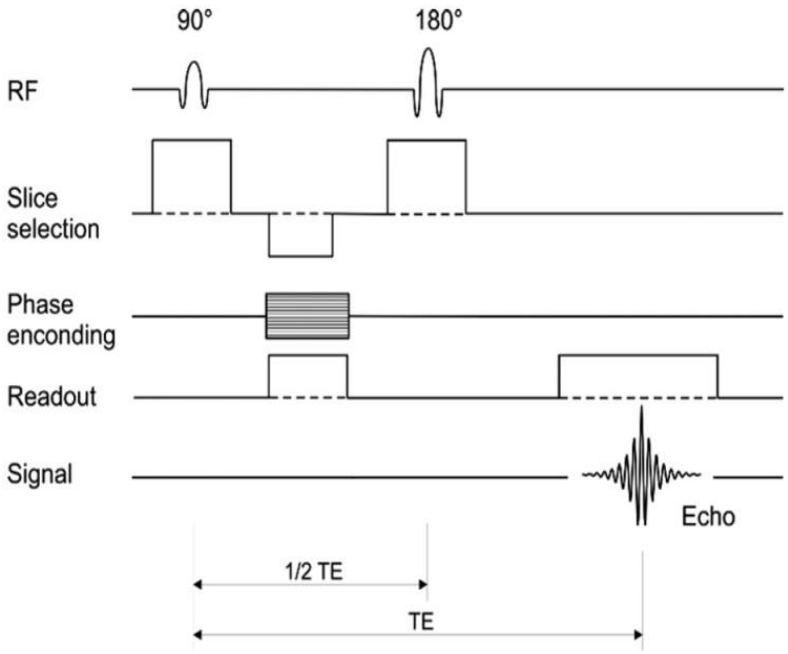


Figure 2.10: Spin echo pulse sequence.

A spin echo sequence begins with the 90° excitation pulse that flips the NMR to the traverse axis. The NMV then precess in the transverse axis and induces a voltage in the receiver coil. When the RF pulse removed, the induced voltage decreases and a FID is produced. $T_2^*$ occurs instantly and the signal decay. The 180° RF pulse possesses sufficient energy to flip the NMV through 180°. The magnetic moments dephase in the transverse axis under the effect of $T_2^*$. These magnetic moments then become out of phase and flipped to the transverse axis by the 180° RF pulse. The magnetic moments at this stage still on the transverse axis but the magnetic moments that were in the trailing edge before applying the 180° become on the leading edge. On the other hand, the magnetic moments that were in the leading edge before the 180° become the trailing edge [Westbrook and Roth, 2013].

The precession direction remains the same, until the trailing edge match the leading edge after a period of time and the two magnetic moments superimposed and become in phase again. At this moment, a large signal is induced in the receiver coil. This signal is called the spin echo [Westbrook and Roth, 2013].

The pulse timing can be adjusted to give different types of MR images. For example, when only one 180° rephasing pulse is used with a short echo time

TE and short repetition time TR the resulting image would be T1-weighted. However, in order to produce a proton density or a $T_2$-weighted, TE should be long to allow enough time for signal due to $T_2$ from different molecules to decay. And therefore, the the differences between their $T_2$ becomes distinguishable [Westbrook and Roth, 2013].

#### Uses

The spin echo pulse sequence is the most popular pulse sequence in many studies because that a T1 weighted image is a powerful technique to demonstrate the anatomy of any structure due to its ability to distinguish different tissues according to their $T_1$ values which have different decay rate in different molecules. However, in some cases when used with contrast media enhancement it can show pathology with high quality. $T_2$ weighted images are also capable of demonstrating pathology. This because the diseased tissues are usually oedematous and/or vascular which means they have a high water content and therefore, high signal in $T_2$ weighted images and consequently can easily be defined [Westbrook and Roth, 2013].

#### Advantages and disadvantages

As SE uses 180° RF rephasing pulses it overcomes problems due to the field inhomogeneity and therefore, generates a high image quality. In addition, it is very versatile sequence which can produce both true $T_2$ weighted image sensitive for pathology and PD. The main disadvantage of SE is the long scan time due to the additional time needed for extra 180° rephasing pulses [Westbrook and Roth, 2013].

### 2.3.2 Gradient Echo (GE) sequence

The long times for SE can be avoided by using ultra fast SE sequences or by gradient echo pulse sequence which consists of a 90° excitation pulse and variable gradients instead of rephasing pulses (figure 2.11). This leads to short TR times and therefore short total scan times without saturation. The

gradients are used to rephase the FID [Westbrook and Roth, 2013].

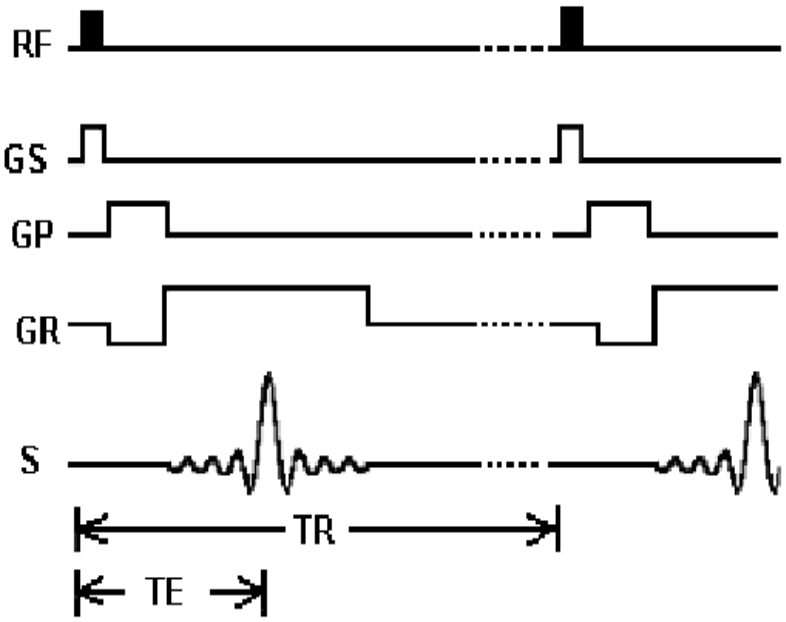


Figure 2.11: Gradient echo pulse sequence.

In GE, the frequency encoding gradient is used for this purpose because that it is quicker than the 180° rephasing pulse which lead to minimum TE. The phase encoding gradient in GE applied between the excitation and signal collection.The frequency encoding gradient is firstly applied negatively to speed up the FID decay followed by another but positive gradient to rephase the readout echo. However, because there are no 180° pulses, the gradients echo sequence does not compensate for the field inhomogeneity so a great deal of $T_2^*$ information will be displayed in this sequence [Westbrook and Roth, 2013].

**Uses**

GE pulse sequence can generates $T_2^*$, $T_1$ and PD weighting. The fast frequency encoding used in this sequence results in a significant reduction in the total scan time due to the short TR needed. Consequently, when fast imaging is required such as breath hold imaging in the abdomen, single slice GE can be used. In addition, it is a very useful technique because it is very sensitive to moving nuclei such as flowing particles as gradient rephasing is not slice selective. Therefore, it is useful for angiographic imaging

[Westbrook and Roth, 2013].

#### Advantages and disadvantages

Gradient echo pulse sequences have the advantage of a reduced TR and therefore a short scan time. This is because the gradients are much faster than the RF pulses. However, this leads to the fact that the dephasing due to field inhomogeneity remain unsolved [Westbrook and Roth, 2013].

## 2.4 Encoding and image formation

### 2.4.1 Introduction

In MRI, the application of gradients typically selects a particular slice and generates a frequency shift along one plan of the slice, and phase shift on the other axis. Therefore, it is possible to define the location of the signal within the image according to its frequency and phase by detecting the number of times the magnetic moment induces a response in a receiver coil (frequency) and the location around the precessional path (phase). The detected data now can be translated to an image. When the information of the frequency and position of the signal are acquired it can be stored in the array processor of the computer in k-space.

### 2.4.2 k-space description

The raw data has to be processed and reconstructed before visualising it as an image. The k-space of a single slice is illustrated in Figure (2.12. K-space is a rectangular shape space which has two perpendicular axes (phase and frequency) used to store the digitised signals during data acquisition. Each axis has a positive and negative side. The horizontal axis is called the frequency axis and the vertical axis is know as the phase axis. The matrix size of the k-space and therefore for the final image, can be controlled by setting the frequency and the phase encoding matrix [Westbrook and Roth, 2013].

It should be noted that k-space is the spatial frequency domain which

means that the frequency and location of the signal within the sample is stored. The frequency can be measured as a phase over distance and its unit is radians. Therefore, the k-space unit is rad/cm. Although both real space and k-space have the same matrix size, the positions of their corresponding pixels do not directly related to each others. That is to say, information acquired from top right pixels of k-space does not corresponding to the raw information for the top right pixel in the image [Westbrook and Roth, 2013].

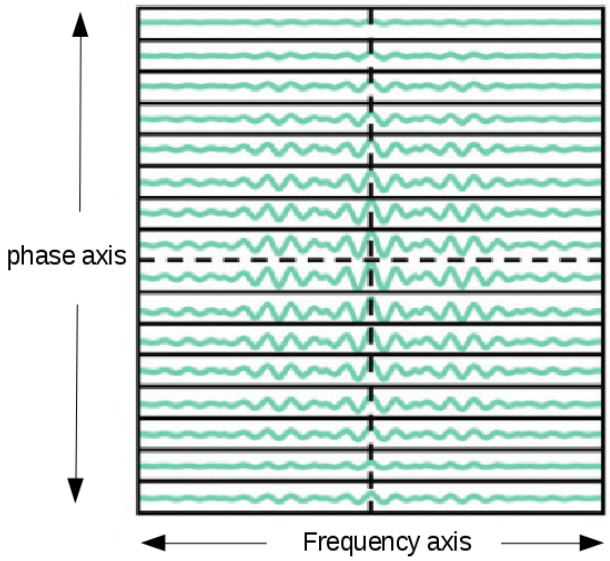


Figure 2.12: Example of k-space with phase and frequency data, image from [Westbrook and Roth, 2013].

### 2.4.3 k-space filling

Lines of k-space are always numbered in a certain way starting with lowest numbers in the central area and increases toward the edges. The upper half of the k-space represents the positive side and the lower half represents the negative lines , see Figure 2.13. Similarly, the horizontal axis contains a positive side (right) and a negative side (left). This is because the position of lines in k-space determined by two components, polarity and slope of the gradient [Westbrook and Roth, 2013].

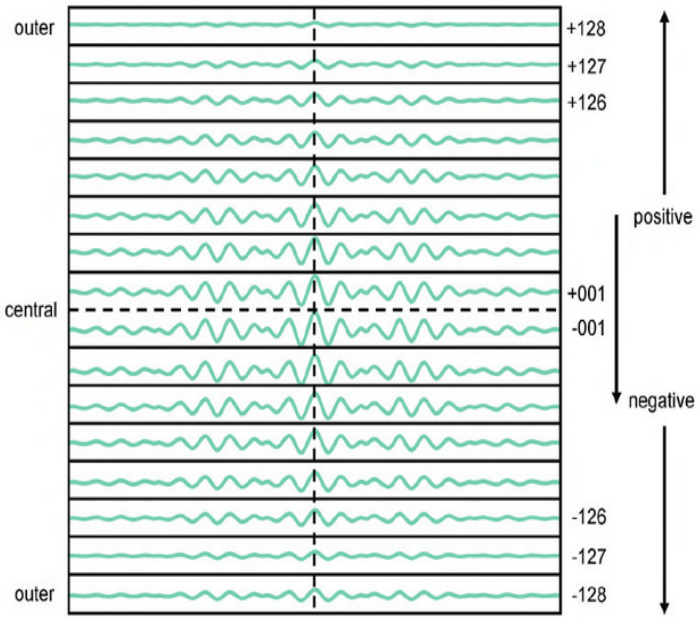


Figure 2.13: Characteristics of k space, image from [Westbrook and Roth, 2013].

Because the phase gradient is changing every TR, data from each TR represented in a different line of k-space Figure 2.14. If otherwise, the same gradient polarity and slope applied for each TR then the same data will overwrite on the same line. As the phase matrix is determined by the number of filled lines, if the phase encoding gradient has not changed this results in single pixel image in its phase direction. Therefore, it is important to change both the polarity and the slope of the phase gradient every TR to produce the image resolution in the phase axis. That is to say, positive polarity gradients fill the upper half of the k-space and the negative polarity gradients pick lines in the lower half of the the k-space [Westbrook and Roth, 2013].

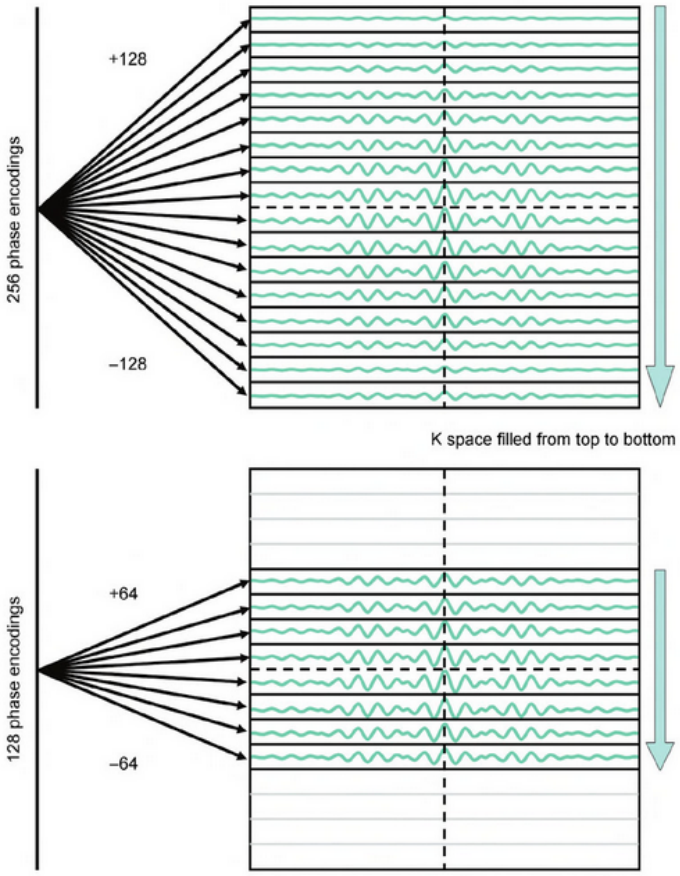


Figure 2.14: Phase matrix of k space, image from [Westbrook and Roth, 2013].

Moreover, the position of the line in k-space is dependent on the slope of the phase gradient. Central lines filled when shallow gradient used and the outer edges of k-space (either positive or negative) are filled when steep gradients. As the slope of the gradient increases, lines fill k-space from central to outer limits. The pattern of k-space filling is generally from bottom to top or from top to bottom.

In SE for example, the slice selection gradient applied during the excitation pulse selects which k-space to be filled, and the 180° rephasing pulses to selectively excite and rephase particular slice. Applying the phase encoding gradient determines the position of the line to be filled with data. While the readout gradient fills each line with different information based on the frequency of the detected signal. If we assume that k-space is 256 phase matrix k-space filled in linear way starting from +128 , +127 and decreases until it reaches central lines Figure 2.14.

The frequency encoding gradient now applied to determine the FOV. When frequency encoding gradient applied, different frequencies in echo can be digitized to collect data points that fill particular line of k-space selected previously by phase encoding gradient Figure 2.15. These data points arranged during the sampling rate period from left to right.

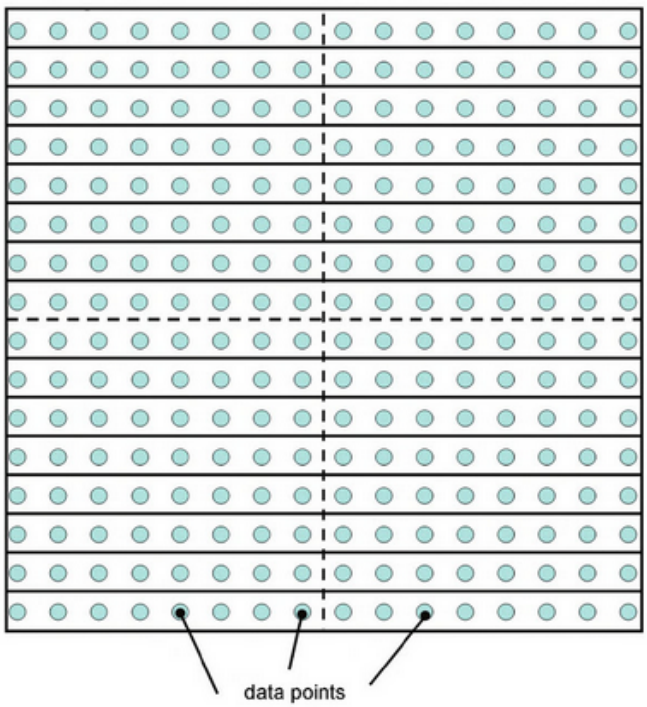


Figure 2.15: Data points in frequency encoding, image from [Westbrook and Roth, 2013].

The frequency matrix of the image is determined by the number of acquired data points. The frequency encoding gradient is switched off immediately when the sampling rate completed and this process repeated again in the next slice. The phase encoding gradient applied again with the same polarity but with different amplitude to fill another line in the k-space and repeated until all lines are filled. All this occurs in one TR period that is why it is important to increase TR to allow more time to excite, rephase, phase and frequency encoding slice. However, in short TR, less time allowed so fewer slices can produces.

Once line +128 of all slices has been filled. Another TR is repeated with different phase encoding gradient amplitude to fill line +127 of all slices and

so on. This type of k-space filling known as linear k-space filling where phase encoding gradient applied repeatedly but with less gradient strength amplitude to fill the next line.

### 2.4.4 Fast Fourier Transform (FFT)

The mathematical derivations of the Fourier transform are beyond the scope of this chapter. However, the basic concepts of FFT will be described here. The MR image quality is dependent on the matrix which consists of a number of pixels. This matrix size is defined by the number of filled lines in k-space (phase matrix) and the number of collected data points in each single line (frequency matrix). A process called FFT converts these data to an image allocated a gray scale depending on the magnitude of signal at each slice. As each data point contains phase and frequency information of the whole slice at a certain time during the readout.

This means that frequency amplitudes goes from frequency domain to spatial domain. FFT then, uses mathematical processing to convert it from time domain to frequency domain. This is crucial because gradients spatially locate signals according to their frequencies only, not their time. Because FFT deals with frequencies, the system should be capable of converting the information acquired from phase encoding gradient to frequency. This can be performed by applying phase gradient over the bore of the magnet which produces a phase shift over a distance. Therefore, each frequency represented as a sine wave according to the degree of phase shift produced by the gradient. That is to say, steep phase gradient generates larger phase shift and results in higher frequency and therefore, shallow phase gradient produces low distance shift and low frequency.

The FFT, collects this information and generated it in two dimensions. The data then transform to signal versus corresponding frequency and therefore produce gray scale corresponding to each pixel in the 2D matrix of the images.

## 2.5 Signal enhancement using Hyperpolarisation methods

As was mentioned earlier in Section 2.1, MRI based on the detection of the a signal originated from the nuclear spin angular momentum in particular magnetic field at thermal equilibrium. In the absence of external magnetic field, spins distributed randomly. However, when an external magnetic field is applied some of these spins (with low energy) align parallel and some (with high energy) align antiparallel with the applied field. The distribution between the spin up and spin down orientations determines the magnitude of the MR signal. The population distribution of spin states is controlled by Boltzmann distribution and can be given by equation 2.2.

The magnetic field and thermal energy can be exploited to boost the spin distribution and therefore, MR signal as in may hyperpolarisation methods such as (brute force) which will be discussed in more details in the following section.

### 2.5.1 Brute-force

This method termed the brute force approach [Roberts and Dabbs, 1961], and has been practicable since 1970 [Brewer, 1977]. It is simply based on (equation **??**) as it shows a direct relationship between the NMR signal and the static magnetic field and inverse relationship between NMR signal intensity and the temperature in the thermal equilibrium conditions. The Brute force technique is the most straightforward technique and it has several advantages over other hyperpolarisation techniques. It applies a very strong magnetic field at a very low temperature close to absolute zero for a long time enough to enhance the nuclear spin polarisation [Viale and Aime, 2010], that is expected by the following equation:

No free-radicals, microwave excitation, or co-solvents are required [Hirsch et al., 2015]. Two obvious advantages result, First, as the known contaminants (radicals) are not used in this method no need for quality assurance and downstream filtering. Second, no secondary chemistry or physics are required to achieve the po-

larisation process as it is more general, relaying only on Boltzmann law polarisation. These advantages are similar to those used in parahydrogen methods, which uses catalytic metals for chemical transformation[Bowers and Weitekamp, 1987] or transient association with the molecular targets [Adams et al., 2009a] of HP as has been used in our study.

Table 2.1 below compares the polarization of selected nuclei in different magnetic field and temperatures [Månsson, 2002].

Table 2.1: This table compares the polarization of selected nuclei in different magnetic field and temperatures. P1 is polarisation number one and P1 is polarisation number 2. Table from [Månsson, 2002].

| Nucleus | Polarisation P1 at 1.5 T,310 K | Polarisation P2 at 20 T, 4 K | Ratio P2/P1 |
|---|---|---|---|
| $^{1}$H | $4.9.10^{-6}$ | $5.1.10^{-3}$ | 1033 |
| $^{3}$He | $3.8.10^{-6}$ | $3.9.10^{-3}$ | 1033 |
| $^{1}$3C | $1.2.10^{-6}$ | $1.3.10^{-3}$ | 1033 |
| $^{1}$29He | $1.4.10^{-6}$ | $1.4.10^{-3}$ | 1033 |

A 1000 fold signal enhancement is reported when the temperature is decreased from 310 K to 4 K and the magnetic field is increased from 1.5 T to 20 T [Månsson, 2002].

The polarization level of the hyperpolarised nuclei return again to thermal equilibrium level when they are moved back into the earth's magnetic field. The rate of the decay is controlled by the longitudinal relaxation T1 rate which is determined by:

$$P(t) = exp(-t/T_1)(P(0) - P_{thermal}) + P_{thermal} \tag{2.4}$$

where P(0) refers to the initial polarization, $P_{thermal}$ is the equilibrium polarization and $T_1$ is the relaxation rate that is different from one nucleus to another and also depends on the field.

These levels of signal enhancement are still not very high and can be increased several hundreds times. For example, a range of 200,000 folds of signal enhancement can be approached when a 16 T and 7 milliKelvin used compared

to only 1000 folds, when a 3 T and 310 K is used [Owers-Bradley et al., 2013]. Although this is a significant enhancement, there are two issues that should be considered. First, is the ability to maintain this level of polarisation when returning to the room temperature, which is inevitably needed for the majority of clinical applications.

That is to say, brute force is a very demanding technique in term of technical challenges and high costs. Nevertheless, other methods can be used to increase the polarisation levels sufficiently utilizing $^{3}$He, $^{129}$Xe and $^{13}$C.

### 2.5.2 Optical Pumping

Noble gasses ($^{3}$He $^{129}$Xe) can be hyperpolarised by a method called optical pumping. Optical pumping is a hyperpolarisation technique that uses a light source to excite particular electron transitions to create out non-equilibrium spin polarisations.

In this method, Noble gases such as $^{3}$He and $^{129}$Xe can be hyperpolarised when they are mixed with an alkaline metal vapour, or metastable atoms e.g $^{3}$He [Franken and Colegrove, 1958], and the mixture irradiated using circularly polarised light from a laser at an appropriate frequency. The valence electrons of these atoms then become spin polarised. The alkali (or the metastable atoms) absorb the angular momentum of the laser light, and the spin exchange occurs during the interatomic collisions which transfers the polarisation to the noble gasses [Altes and Salerno, 2004, Oros and Shah, 2004]. This approach produces a very strong polarisation enhancement several times greater than that produced when using the strongest laboratory magnets. Moreover, this enhanced polarisation persists for a long time.

The physical and physiological properties should be considered when choosing a HP noble gas. Despite the fact that Xenon is naturally more abundant, Helium is more widely used in these studies because it has larger gyromagnetic ratio ( $\gamma$ $^{3}$He = 0.76 $\gamma^{1}$H and $\gamma^{129}$Xe = 0.28 $\gamma^{1}$H). However, the MR signal of

$^{3}$He is more sensitive to attenuation because it has a larger diffusion coefficient than $^{129}$Xe [Wild et al., 2002]. Moreover, $^{3}$He is virtually insoluble so it is limited to the lung air-space during breath hold. $^{129}$Xe is highly soluble and makes it the suitable for perfusion studies of gas exchange [Norquay et al., 2013].

In term of clinical applications, functional MRI of the lung using hyperpolarised $^{3}$He gas has proven to provide valuable in demonstrating pathophysiological changes [van Beek et al., 2004]. This can offer a solution to the limited application of lung imaging using MRI because the conventional proton MRI provides poor anatomical information [Wild et al., 2003].

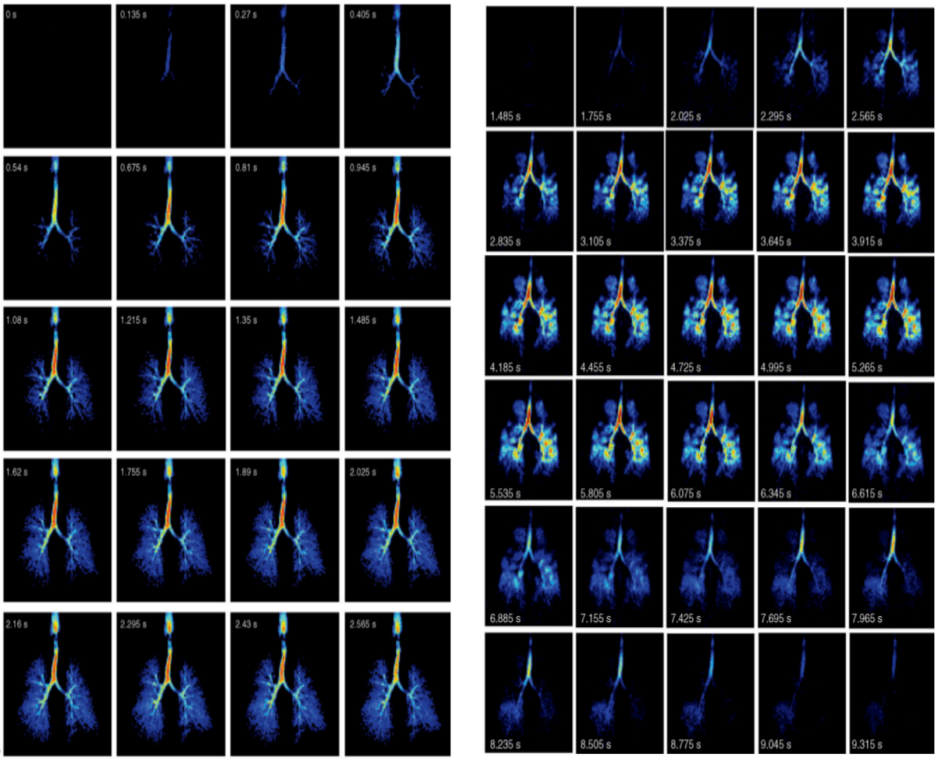


(a) (b)

Figure 2.16: Dynamic images acquired utilising a sliding window radial sequence (reference [Wild et al., 2003]). (a) Images from a healthy normal (128 views per frame) collected at equal intervals from the inhalation of 300 mL of 3-He polarized to 40%. The dynamic flow of the inhaled gas is clear down from the trachea to the lungs. (b) Dynamic time series collected from a patient with Chronic Obstructive Pulmonary Disease COPD demonstrating areas of ventilation obstruction specially in upper lobes and delayed emptying of gas in the left lower lobe, which may indicates an air trapping. image taken from reference [van Beek et al., 2004]

However, the major drawback is that the optical pumping uses noble gases that are limited to lung studies and some perfusion investigations.

### 2.5.3 Dynamic Nuclear polarization (DNP)

Dynamic Nuclear Polarisation (DNP) is a method that permits a significant enhancement of NMR signal intensities of solids and liquids, and therefore is considered as an important tool in structural and mechanistic investigations of biologically relevant molecules [Maly et al., 2008]. This process usually occurs in low temperature less than (1-2 K) and high magnetic field ( 3 T ) in the presence of radiations from high frequency microwaves. This phenomena was first predicted by Overhauser [Overhauser, 1953] when he proposed that it is possible to transfer the large Boltzmann polarisation derived from unpaired electrons to the neighbouring nuclei by the saturation of the corresponding Electron Paramagnetic Resonance (EPR) transition [Maly et al., 2008]. However, this phenomena was not measured experimentally until the work of Slichter in 1953 [Carver and Slichter, 1953].

The high spin polarisation, typically, generated from a bath of free radical electrons, transferred to a nuclear spin bath which enhances the difference between the nuclear energy levels (non-Boltzmann distribution). This is because at the same temperature and same magnetic field, the polarisation of electron spin is significantly greater than that of nuclear spin. At a temperature of 90 K for example, the polarisation of proton spin and electron spin are 0.016% and 10.541% receptively [Maly et al., 2008]. The ratio between the nuclear and electronic resonance frequency can be used to increase the nuclear polarization under optimal conditions. This ratio is about 2600 for $^{13}C$ nuclear spins [Månsson, 2002].

There are four categories of the transfer process in DNP. Currently, the Overhauser Effect [Overhauser, 1953], is the only known DNP mechanism for liquid state NMR. For solid samples, there are three main enhancement processes : Solid Effect (SE) [Jeffries, 1957], Thermal Mixing (TM) [Abragam et al., 1982, Abragam and Goldman, 1978] and the Cross Effect (CE) [Kessenikh et al., 1963, Hwang and Hill, 1967]. The details of these methods are beyond the scope of this thesis.

**Signal enhancement using DNP methods**

A NMR liquid state signal of 10000 times of enhancement was obtained by combining the dynamic nuclear polarization DNP [Abragam and Goldman, 1978] at low temperatures with fast sample dissolution DNP [Ardenkjær-Larsen et al., 2003]. The process begins with the material that contains the target nuclei being doped with a free radical followed by applying a high magnetic field (e.g. 3T) and low temperature (about 1 K) which results in $90 - 100\%$ polarization of the unpaired electrons and only 0.1% polarization of the $^{13}C$ nuclei [Månsson, 2002]. Then, microwave radiation is used to transfer the polarization from the unpaired electrons of the radical to the target nuclei to gain nuclear polarization of $20\% - 40\%$ in the solid state material. This then needs to be rapidly thawed and dissolved immediately in order to be used and (in some applications), injected with small signal loss [Golman et al., 2002].

However, even though solid state DNP has proven to be a useful analytical tool it still challenging to be used for *in-vitro* or *in vivo* studies [Pileio et al., 2013]. The hyperpolarised nuclear spin magnetization still decays with T1, the time constant which remains from milliseconds to few minutes [Pileio et al., 2013]. This method was developed to be useful for dissolved state NMR. This hyperpolarisation state can be employed for *in vivo* studies. Due to the signal enhancement using the DNP hyperpolarisation technique, the role of MRI can be extended to study non-proton nuclei and thus allows novel kinds of investigations e.g. visualization of metabolic processes which were previously unachievable [Rossini et al., 2013].

DNP is limited by the slow understanding of its complex theory compared to the fast clinical progress which was described in many studies [Banerjee et al., 2013, Hovav et al., 2012]. In addition, it requires a long relaxation times and labelling of the hyperpolarised molecule. This is because the development of the *in-vivo* studies requires a long relaxation times sufficient enough to perform injection and transport to the area of interest. Also it needs free radicals consists of substrate to form a signal at low temperature. This can be done by

labelling the molecule (i.e $\hat{1}$3C labelled) which in fact makes the DNP method more demanding.

## 2.6 Parahydrogen

Hydrogen molecule consists of two hydrogen atoms linked by covalent bonds. Each hydrogen atom comprises one positively charged proton that have a nuclear spin. This produces an angular momentum that associated with proton's spin of 1/2. Applying a magnetic field makes these spins align either parallel $\alpha$ or antiparallel $\beta$ to the direction of the field.

Molecular hydrogen exists in two isomers, termed para- and orthohydrogen which differ in their nuclear spin configurations. The possibility of these two isomers is derived from the Pauli principle which requires that the overall wavefunction that describe fermions to be antisymmetric with the respect to nuclei exchange [Green et al., 2012]. The overall wavefunction of dihydrogen can be expressed as:

$$\Psi = \psi_E \psi_V \psi_R \psi_T \psi_N \psi_S \tag{2.5}$$

where $\Psi, K = E, V, R, T, N, S$, are the electronic, vibrational, rotational , translational , nuclear and spin wavefunctions respectively. As the electronic, translational and vibrational are all symmetric, the rotational and nuclear products must be antisymmetric [Green et al., 2012].

In case of molecular hydrogen there are four spin configurations $\alpha\alpha$ , $\beta\beta$ , $\alpha\beta$ and $\beta\alpha$. Where $\alpha$ is the parallel alignment of spin with the applied magnetic field and $\beta$ is the antiparallel alignment. $\alpha\alpha$ and $\beta\beta$ are symmetric with respect to particle interchange, while $\alpha\beta$ and $\beta\alpha$ are neither symmetric nor antisymmetric [Green et al., 2012]. Nevertheless, the symmetric and antisymmetric states can be produced by a simple linear combinations of these functions 2.17. Thus, the normalised nuclear spin states of hydrogen molecule will be:

(Symmetric triplet)

$$\begin{aligned} |T_{+1}\rangle &= |\alpha\alpha\rangle \\ |T_{-1}\rangle &= |\beta\beta\rangle, \\ |T_0\rangle &= \frac{1}{\sqrt{2}}|\alpha\beta + \beta\alpha\rangle \end{aligned} \tag{2.6}$$

(Antisymmetric singlet)

$$|S_0\rangle = \frac{1}{\sqrt{2}}|\alpha\beta - \beta\alpha\rangle \tag{2.7}$$

Orthohydrogen (S=1), represents the triplet of the symmetric nuclear spin states ($\alpha\alpha$, $\beta\beta$ and $\alpha\beta$ + $\beta\alpha$) which are all coupled to antisymmetric (odd J) rotational states. However, parahydrogen (S=0) reflects the antisymmetric singlet nuclear spin state ($\alpha\beta$ - $\beta\alpha$) coupled with symmetric (even J) rotational states [Green et al., 2012]. The variation in the rotational configurations accessible to the two isomers leads to different in energy. Parahydrogen is more stable than orthohydrogen, as the lower energy rotational state is accessible. This difference causes a distribution among the isomers, with the equilibrium concentration of parahydrogen favoured by the lower temperatures [Green et al., 2012].

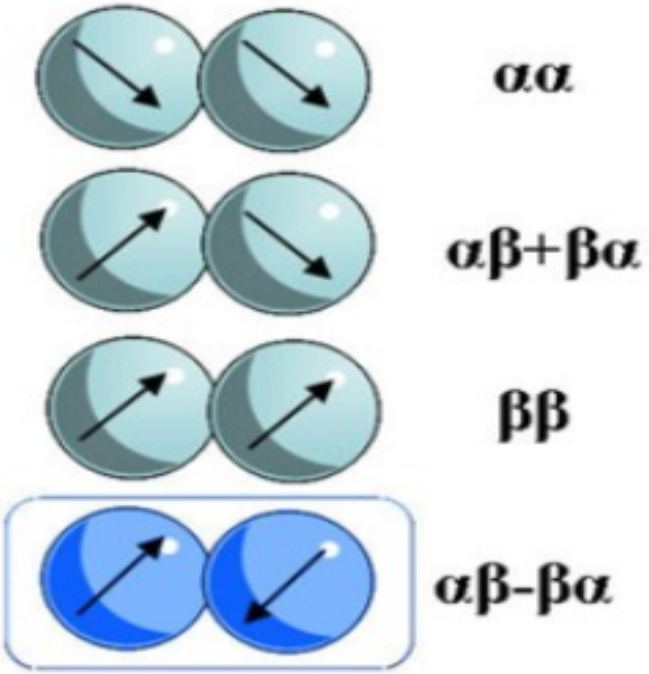


Figure 2.17: This graph demonstrates the four spin combinations of dihydrogen split into two isomers of orthohydrogen and parahydrogen. The highlighted box refers to the lowest energy parahydrogen state. Image from (https://www.york.ac.uk/chym/parahydrogen/).

In thermal equilibrium at room temperature, the ratio between orthohydrogen and parahydrogen is 3:1. This means that molecular hydrogen consists of 75% of orthohydrogen and only 25% of parahydrogen. It is possible to get pure parahydrogen by cooling the hydrogen molecule [Green et al., 2012]. The amount of parahydrogen increases as the temperature of Hydrogen decreases until it reaches about 99% at 20 K. Equation (2.8) describes the relationship between the parahydrogen over orthohydrogen percentage as a function of temperature across the range 20 - 273 K [Farkas, 1935, Harkness and Deming, 1932]. Table 2.2 below shows how the amount of parahydrogen increases as the temperature decreases [Green et al., 2012] which contains sufficient terms to calculate the equilibrium para/ortho ratio over the temperature range $20-273$ K [Farkas, 1935, Harkness and Deming, 1932]. Calculations using $\theta_R = 87.6$ K [Atkins and De Paula, 2006], show that the expression continues to converge up to about 500 K as illustrated in table 2.2.

$$\frac{N_{para}}{N_{ortho}} = \frac{1 + 5exp(-\frac{6\theta_R}{T}) + 9exp(-\frac{2\theta_R}{T}) + 13exp(-\frac{42\theta_R}{T}) + ...}{3(3exp(-\frac{20\theta_R}{T}) + 7exp(-\frac{20\theta_R}{T}) + 11exp(-\frac{30\theta_R}{T}) + ...)} \tag{2.8}$$

Table 2.2: This table shows how the the amount of parahydrogen increases as the temperature decreases. Taken from [Adams et al., 2009b].

| Temperature (K) | Parahydrogen in equilibrium mixture (%) |
|---|---|
| 20 | 99.8590 |
| 65 | 62.2388 |
| 77 | 52.0859 |
| 190 | 26.4256 |
| 200 | 26.1013 |
| 230 | 25.5061 |
| 250 | 25.3004 |
| 273 | 25.1644 |
| 298 | 25.0851 |
| 350 | 25.0215 |

### 2.6.1 Parahydrogen Induced Polarization (PHIP)

PHIP was first observed by Bryndza and Bergmann in 1980. This discovery was followed by theoretical predictions by Bowers and Weitekamp in 1986 [Bowers and Weitekamp, 1986]. One year later, two independent groups proved this experimentally [Eisenschmid et al., 1987, Bowers and Weitekamp, 1987]. The concept of PHIP spectroscopy is based on the hydrogenation reaction between parahydrogen and an unsaturated molecule. A characteristic antiphase signal was observed during the hydrogenation reaction between acrylonitrile and parahydrogen inside spectrometer and named by Bowers and Weitekamp as Parahydrogen And Synthesis Allow Dramatically Enhanced Nuclear Alignment (PASADENA)[Bowers and Weitekamp, 1986].

In 1988 [Pravica and Weitekamp, 1988], a different signal pattern was observed when the hydrogenation was performed outside the spectrometer in the earth's magnetic field, followed by transferring the sample to a spectrometer for investigation in a strong magnetic field. This effect is called Adiabatic Longitudinal Transfer After Dissociation Endangers Net Alignment (ALTADENA). The acronym PHIP (Parahydrogen Induced Polarisation) is a term

used to cover all parahydrogen experiments (ALTADENA and PASADENA) that have only small differences that arise from a Boltzmann factor in order of $10^{-5}$. The formation and transfer of PHIP are governed by the scalar spin spin interaction. Moreover, there is a possibility of forming four transitions which give rise to two doublets which are located in the corresponding resonance frequency according to its chemical shift.

The significant signal enhancement observed in PHIP allowed $^{13}$C angiography in less than 1 s [Golman et al., 2001]. Therefore, hyperpolarisation derived from PHIP impacts MR clinical imaging based on observing a long-lived $^{13}$C magnetic state instead of detecting the common signal from $^{1}$H [Frangioni, 2008]. For example, the feasibility of imaging of hyperpolarised $^{13}$C was examined and compared to typical proton imaging using both spin echo and gradient echo sequence [Golman et al., 2001] Figure 2.18. In this study [Golman et al., 2001], two types of imaging were achieved before injection. First, high resolution SE sequence was performed which required a long scan time. Second, a GE sequence achieved in a short time which degraded the resolution and the SNR. After that, a single shot RARE sequence was utilised to obtain $^{13}$C images one second following the injection of 3 ml of contrast medium where injected in the tail vein of the rat [Golman et al., 2001].

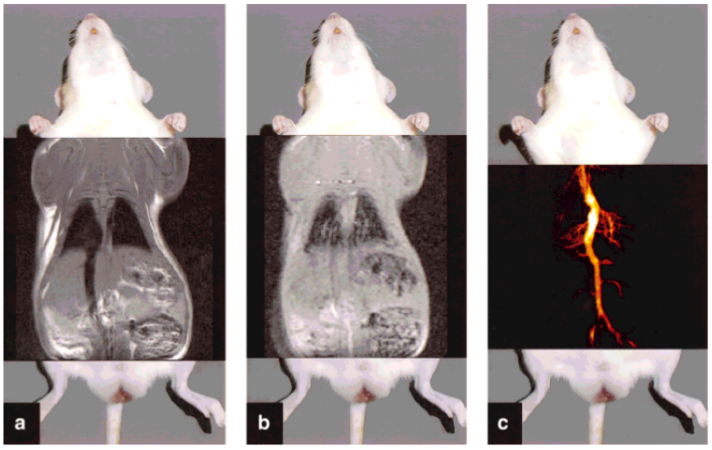


Figure 2.18: Rat images using 2.4 T field. a) Proton SE image with scan time of 5.40 min. b) Proton GE image with scan time of 5.40 sec. ) A $^{13}$C single-shot RARE image with 0.9 sec. The orange color represent the signal enhancement derived from $^{13}$C. Image taken from [Golman et al., 2001].

The low natural abundance of $^{13}$C decreases the amount of enhancement. However, clear demonstration of major veins was obtained with $^{13}$C polarisation of

about 0.3 % and concentration of 150 mM. In addition, since the nuclear polarisation derived from PHIP is independent of field strength, it is possible to perform high resolution NMR in the earth's magnetic field [Golman et al., 2001] which is the basic concept of our study.

**How polarisation transfers from parahydrogen**

The simple population model (AX type) spin system Figure 2.19 provides an easy understanding of this process. It is as required, antisymmetric in exchange of the nuclei [Natterer and Bargon, 1997]. As the total nuclear spin of this wavefunction equals zero, A Zeeman effect can not be seen from parahydrogen itself and therefore has no NMR signal. While the NMR signal of Hydrogen arise only from orthohydrogen and seen at 4.5 ppm on the proton spectrum. This can be seen as three equidistant levels $t_{-1}, t_0, t_{+1}$ related to the wavefunctions $\alpha\alpha, \alpha\beta + \beta\alpha$ and $\beta\beta$.

If the Hydrogenation with parahydrogen performed inside the spectrometer (PASADENA), There will be a significant deviation of the population of these energy levels in the resultant Hydrogen product different from those in thermal equilibrium. When the two parahydrogen nuclei transferred into AX spin system in the product molecule, the population occurs only in the levels $\alpha\beta$ and $\beta\alpha$ (Fig 2.19b). The formation of four transitions are possible, just similar to the standard NMR spectrum. Nevertheless, because the energy levels are selectively populated, this leads to observing two antiphase doublets. Due to the significant population differences, a few orders of magnitude enhancement is achieved in comparison with standard NMR spectrum [Natterer and Bargon, 1997].

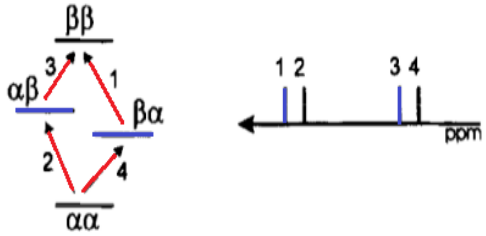


(a) standard NMR system

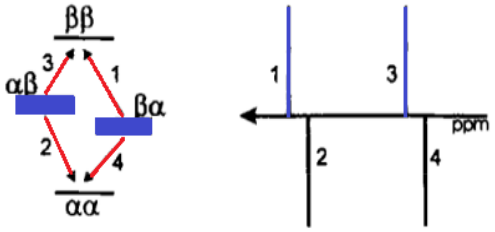


(b) PASADENA process

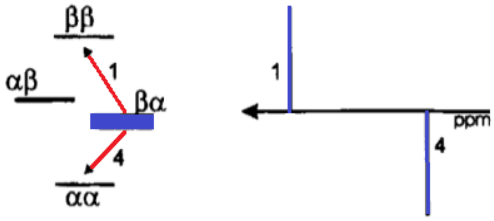


(c) ALTADENA process

Figure 2.19: The population models in case of two spin system of AX type (A) standard NMR spectrum (b) PASADENA (c) ALTADENA. Image taken from [Natterer and Bargon, 1997].

On the other hand, if hydrogenation of Hydrogen occurs outside the NMR magnet in earth's magnetic field (ALTADENA), and sample transferred adiabatically to the strong detection field. In this case, the spin system of the product forms outside the NMR magnet in a low field and forming strongly coupled spin system leading to efficient, coherent distribution of spin polarization [Natterer and Bargon, 1997]. The eigenfunctions being the symmetry adapted spin functions $S, T_{+1}, T_0$, and $T_{_1}$, if the transfer occurs adiabatically and there is no alterations of population. Therefore, the system will be adapted to the new conditions at all times and remains at eigenfucnction state of relevant Hamiltonian. Thus, in the AX spin system at high field, only one level becomes populated of the two levels $\alpha\beta$ or $\beta\alpha$. If the differences resulted from Boltzmann factor are ignored, only two transitions can be formed resulting

in spectrum as shown in Figure 2.19c this is due to the effect of transitory nature. While the thermodynamics influence the spin system to struggle to compensate for population difference that represent utmost non equilibrium state [Natterer and Bargon, 1997].

### 2.6.2 Signal Amplification By Reversible Exchange (SABRE)

Recently, two ways of introducing polarization to molecules without chemical incorporation of parahydrogen into the substrate have been reported [Adams et al., 2009b]. The first approach is known as Insensitive Nuclei Enhanced by polarization Transfer (INEPT). INEPT is a hyperpolarisation method that enhances signal from nuclei with low gyromagnetic ratio such as $^{15}$N, where the polarisation transfers from strong proton magnetic spins to the scalar coupled weak nucleus [Morris and Freeman, 1979]. INEPT is achieved by using a pulse sequence called INEPT. Unlike Nuclear Overhauser effect (NOE), INEPT is dependent on J-coupling instead of dipolar cross relaxation to achieve the polarisation transfer. The second approach is Signal Amplification By Reversible Exchange (SABRE), where a spontaneous polarization transfer from parahydrogen to substrate occurs at low magnetic field. In this method, the polarisation transfers with no need to generate the RF pulses but it occurs only due to spontaneous polarisation transfer.

A dedicated study of SABRE was published in 2009 [Adams et al., 2009b, Bowers and Weitekamp, 1986, Atkinson et al., 2008]. This method is very similar to PHIP in using parahydrogen as a source of magnetisation transfer. However, the most important difference is that it does not incorporate in the substrate. The polarisation transfer is mediated by a transition metal complex. When a contact between parahydrogen and metal complex forms the covalent form is broken to create dihydride and reversely the dihydride separated to form the molecular Hydrogen again. As shown in figure 2.20). In the same time, substrate ligands binds to the metal centre and detached later just as with hydride ligands. In the presence of scalar coupling the polarization transfers from parahydrogen to molecule of interest. Followed by a dissociation of target molecule from the complex resulting in free hyperpolarised substrate. In this case, signal from $^{1}$H and heteronuclei of polarized

substrate can be observed.

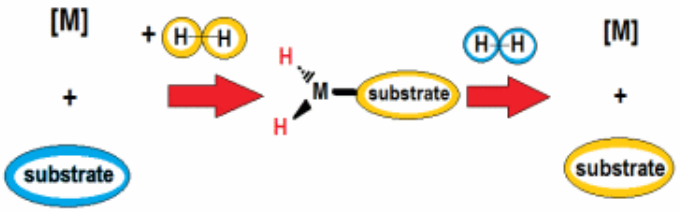


Figure 2.20: Schematic representation of SABRE method in which polarisation transfers from parahydrogen to substrate without chemical incorporation of the molecules. Where the yellow color indicates the hyperpolarisation state. Image adapted from [Adams et al., 2009b].

The main advantages of SABRE when compared to PHIP are, First, there is no chemical incorporation of parahydrogen into the the substrate. Second, it is a repeatable process, this is because parahydrogen is the only consumable reactant within the reaction.

### Theoretical approaches

For simplification, a model was considered in previous studies [Adams et al., 2009b] to provide an easy understanding of theoretical basis of SABRE. The model consists of two $^1$H in one substrate coupled to two hydride nuclei of former parahydrogen on the metal centre of the equatorial plan of the complex. Thus, there are four spin systems in the bound complex and only two spin system in the free substrate.

As the model of the original parahydrogen $^1$H nuclei is considered as A2 spin system [Natterer and Bargon, 1997]. Two spin systems possibilities are available in the case of free substrate. Each contains two different conditions as the following:

**First**, two possibilities in the case of free substrate:

1- $B_2$ coupling topology- (Isochronous substrate) when the two $^1$H nuclear spins of the substrate have the same chemical shift.

2- BC spin topology - (Anisochronous substrate) when the two $^1$H nuclei of the substrate have different chemical shift.

Figure 2.21, depicts a schematic representation of an octahedral (model) complex with two substrate ligands.

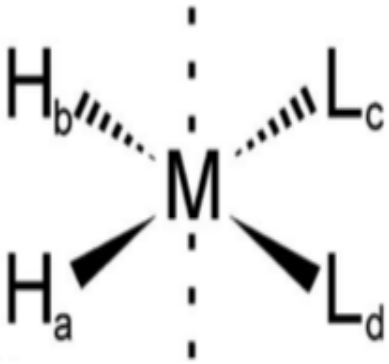


Figure 2.21: Schematic representation of the equatorial ligands in the octahedral complexes. $H_a$ and $H_b$ are the Hydrogen atoms derived from parahydrogen, $L_c$ is the substrate and $L_d$ is a second ligand. Image from reference [Adams et al., 2009b].

Where $H_b$ and $H_a$ represent parahydrogen originated nuclei, $L_d$ and $L_c$ represent the substrate molecules (ligands). In theory, we only consider the polarisation transfer to $L_c$ for simplification. Therefore, there are only four spin systems demonstrated here. According to their positions, $H_b$ and $H_a$ are either *cis* or *trans* and possess different way of coupling to $L_c$ protons producing magnetic inequivalence in the complex disregarding the correlated chemical sifts of the complex topologies.

**Second** (with respect to chemical shift), two possibilities in the case of complex that incorporates isochronous substrate:

1 - AABB where $L_c = L_d$ and the chemical shifts of each pair of $^1$H nuclei are equivalent .

2 - ABCD where $L_c \neq L_d$ and the chemical shifts of each pair of $^1$H nuclei are inequivalent.

Finally, two possibilities in the case of complex bound with Isochronous substrate :

1- AABC where $L_c = L_d$ and former parahydrogen pair of $^1$H have the same

chemical sift while the substrate has a pair of $^1$H with inequivalent chemical shift

2- ABCD- $L_c$ and $L_d$ and the chemical shifts of each pair of $^1$H nuclei are inequivalent.

When the active catalyst formed, the polarisation transfers from parahydrogen to the substrate. The results of this model are comparable to experimental results [Adams et al., 2009b].

There are two important components resulted from SABRE method before starting the investigations with $^1$H NMR measurements. These are i) The longitudinal magnetization ($I_z$) which results only from using 90° flip angle and ii) The longitudinal two spin magnetisation ($I_zS_z$) which result from flip angles less than 90° or sometimes as a result of 90° imperfections. The maximum magnetization of $I_z$ can be observed at 60 G while the maximum $I_zS_z$ can be observed at earth's magnetic field [Cowley et al., 2011]. For this reason, the two spin magnetisation ($I_zS_z$) can be used as a filter to measure the signal observed only from parahydrogen. This pulse sequence is called OPSY (Only Parahydrogen SpectrscopY) [Aguilar et al., 2007].

After the dissociation of the substrate from the complex any component involving nuclei generated from both parahydrogen and the substrate will be lost [Adams et al., 2009b]. The only remaining term for the polarised free substrate nucleus is $-(\mathrm{bz} + \mathrm{cz})\hat{R}_\mathrm{z}$. The dependence of $\hat{R}_\mathrm{z}$ intensity on the mixing field strength is illustrated in Figure 2.22.

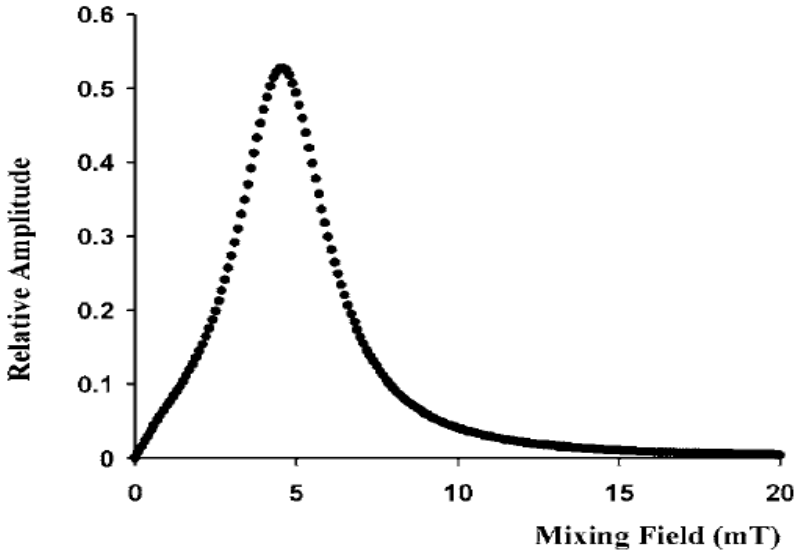


Figure 2.22: The dependency of the longitudinal magnetisation and the mixing field in a model substrate containing a single spin. Image from [Adams et al., 2009b].

## 2.7 Using parahydrogen *in-vivo*

Parahydrogen is ideal for spin order transport *in vivo* due to many reasons. First, because it does not depleted by RF pulse. In addition, it has a long life time of several weeks as long as it is protected as singlet state. Moreover, being the smallest molecule it is highly diffusive in biological tissues. increasingly, viable *in vivo* concentration from $\mu$M to mM in blood.

However, the main challenge of converting the undetectable spin order to visible polarisation *in vivo* is to develop a proper biocompatible catalyst. Alternatively, catalyst can be targeted to some diseases such as cancer cells. Because parahydrogen is small it can be used to hyperpolarise indigenous or exogenous molecules, including Adenosine Triphosphate (ATP) and its derivatives that are usually formed in high concentration around cancer cell. ([Pellegatti et al., 2008]).

## 2.8 Catalyst

The catalyst plays a crucial role is SABRE process as it facilitates the polarization transfer from parahydrogen to the substrate. However, it destroys the signal enhancement by depleting the resulting polarized states through further interaction [Mewis et al., 2014]. Hence, the architecture of the ligand surrounding the metal centre is very important so that it must be efficient to facilitate facile analytic ligation to the metal centre. It should contain sufficient vacant sites, during the catalytic cycle, to allow a firm binding between analyte and parahydrogen-derived hydride ligands. And a free exchange must occur between parahydrogen and the analyte molecules at the metal centre.

The influence of phosphine substituent on the exchange rate of hydride to H and equatorial bond pyridine (trans to hydride) to free pyridine was tested [Mewis, 2015]. At 335 K, the dissociation rate of the equatorial pyridine from $[Ir(PR_3)(py)_2(H)_2]$ quickest for when R=p$-C_6H_6-$OMe, which is the most electron rich Carbine investigated [Mewis, 2015] with rate constant of 0.90 $s^{-1}$ for the loss of Pyradine. Initial studies focused on the use of iridium complexes containing Phosphines ligands. Cationic complexes with formula $[Ir(COD)(PR_3)_2][BF_4]$ were designed were R=Ph , p-tolyl or p$-C_6H_6-$OMe [Atkinson et al., 2009]. The main complex resulted in $CD_3OD$ was $[Ir(PR)_3(py)_2(H)_2]^+$ after the addition of parahydrogen and pyridine with little a mounts of $[Ir(PR_3)(py)_3(H)_2]^+$.

However, the dissociation rate of equatorial pyridine from $[Ir(PR_3)(py)_3(H)_2]$ was faster; at 335 k the rate constant for when R= Ph or p-tolyl were 1:16 and 2.00 $s^{-1}$ respectively. While the rate constant for when R=p$-C_6H_4-$OMe could not be defined due to thermal composition [Mewis, 2015].

Additionally, the influence of catalyst loading on the enhancement of three $^1H$ sites of Pyradine was also studied [Mewis, 2015]. It was reported that when $[Ir(COD)(PC_3)(py)][BF_4]$ was used as catalyst, the enhancement maximised at 1:5 loading level. Particularly, Pyradine ortho protons were enhanced by 94 times (p =0.02 %) when polarisation transfer occurs at 0.5 x $10^{-4}$ T magnetic field, when this loading was utilised relative to those at thermal equilibrium [Mewis, 2015]. Having reported that the electron richness of the phosphine ligand is strongly related to the enhancement of substrate using SABRE, the use

of Carbines is a logical progression [Cowley et al., 2011, Fekete et al., 2013] .

The first use of Carbine complex with SABRE was reported in 2011 [Cowley et al., 2011]. It concentrated on the use of IMes (1,3-bis(2,4,6-trimethylphenyl)imidiazole-2-ylidene) to create the complex [Ir(IMes)(COD)CL]Cl (COD= cyclooctadiene). This gives $[Ir(IMes)(H)_2(py)_3]Cl$ following the activation of hydrogen in the presence of Pyradine [Mewis, 2015]. Structurally, it is similar to the monophosphine complexes. Comparing $[Ir(IMes)(H)_2(py)_3]$ and $[Ir(PCy_3)(H)_2(py)_3]Cl$ as a SABRE catalyst resulted to the observation that the former enhanced the *meta* peak of pyradine in $CD_3OD$ by about 266 times (p=0.04%) , while the enhancement of the latter was only 18 times (p= 0.03%)[Mewis, 2015]. Hence, using the rich electron donating NHC a ligand in the polarisation transfer catalyst resulted in a considerable improvement in the observed enhancement. For theses reasons we used [Ir(IMes)(COD)Cl] [Vazquez-Serrano et al., 2006] as a catalyst in all experiments to facilitate the maximum possible polarisation transfer between parahydrogen and substrate.

## 2.9 Substrate (Pyrazine)

Pyrazine is colorless, water soluble and aromatic heterocyclic organic compound characterized by ring structure of four carbon atoms and two nitrogen atoms and has the chemical formula $C_4H_4N_2$ Figure 2.23. It is known as a symmetrical molecule with point group $D_2h$. Pyrazine, in nature, is less abundant than pyridine, pyrimidine and pyridazine. However, it is of biological and industrial significance. Pyrazine was selected in our study for two important reasons. First, because it is very similar to pyridine that shows a significant signal enhancement in SABRE hyperpolarisation [Atkinson et al., 2009] but it has another nitrogen atom in the ring. Second, it has four protons which have the same chemical environment that generate only one signal in NMR measurements.

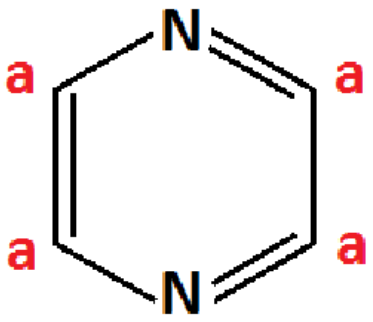


Figure 2.23: The chemical structure of pyrazine which contains four hydrogen nuclei that are chemically equivalent.

There are several derivatives [Ferreira and Kaiser, 2012] such as phenazine which used as antitumor, antibiotic and diuretic activities. In addition, tetramythylpyrazine (also called Ligustrazine) described to scavenge superoxide anion and reduce the production of the nitric acid in human polymorphonuclear leukocytes. Other derivatives are alloxazines and pteridines. Particular pigments, folic acids are Pteridine which plays a vital role in the chemical reactions of the human body. The growth-promoting agent, riboflavin (or Vitamin $B_2$) is an alloxazine compound.

Nicotinamide and aminothiazole were Figure 2.24 used as a substrates in some experiments such as calibrating the flip angle in earth's magnetic field with SABRE. This was done to compare the 90° and 180° flip angle of each molecule to that of pyrazine and water.

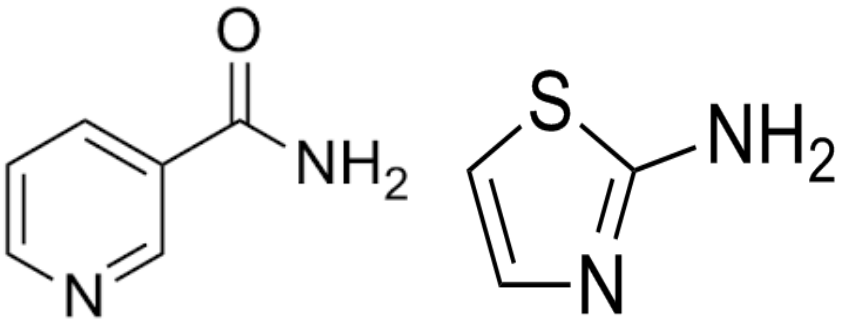


(a) nicotinamide (b) aminothiazole

Figure 2.24: The chemical structure of (a) Nicotinamide and (b) Aminothiazole.

Nicotinamide and aminothiazole were chosen because of their biological importance and due to the range of studies [Shchepin et al., 2016, Olaru et al., 2016] revealed recently using these two molecules to address the inherent NMR insensitivity using hyperpolarisation methods. Figure 2.24 illustrates the chemical structure of each molecule.

# Chapter 3

# Earth's field NMR

## 3.1 Introduction

NMR and MRI studies are often accomplished in high magnetic fields. This is because the high magnetic field is capable of producing a high polarization of the sample (hence, high SNR) and improved sensitivity of detection. In addition, because spectroscopy is based on chemical shift, thus requires a sufficiently strong magnetic field to make their chemical shifts observable.

However, there are many obvious limitations when a high field is used in NMR and MRI. First, images are usually distorted by the field inhomogeneity caused by the significant magnetic susceptibility gradients of the sample broadening the resonance lines, therefore, high field MRI is limited to small samples. Moreover, the strong field uses RF pulse with a small penetration depth [Bottomley and Andrew, 1978]. This decreases the efficiency of nuclear spin excitation and NMR detection when the sample is placed in the magnet [Bennett et al., 1996].

Achieving a highly uniform magnetic field is a demanding technique with several associated engineering issues: Firstly, to generate the strong magnetic field, immobile superconducting coils are required. The superconducting coils need cryogens to keep the magnets cold. Therefore, both superconducting coils and cryogens together are expensive tools limiting the availability of these machines.

As, the bore of the magnet is narrow in high field machines this limits the study of large samples.Although no superconducting magnets are required for the low field NMR, the poor chemical shift resolution would result in low information content obtained from the sample [Michal, 2010].

Recently, there has been a growing interest towards low field MRI/NMR that offers low cost, small size, portable and open scanners. The distortion artefacts caused by metals in high field MRI can be reduced in low field MRI/NMR making it possible to investigate samples inside metallic shells [Matlachov et al., 2004]. In Ultra Low magnetic field (UTF) in the range from $\mu$T to mT, it is not necessary to be in a homogeneous measurement field to achieve narrow line width. The NMR line width is linear with measurement field strength for a fixed corresponding homogeneity which makes it possible to achieve narrow NMR lines with high SNR in the earth's field [McDermott et al., 2002].

Although chemical shift is unmeasurable in ULF because it is dependent on the field strength, scalar coupling phenomena which are independent from field strength can be detected in ULF [McDermott et al., 2002]. Moreover, $T_1$ is often much longer in low field allowing to produce significant contrast not possible in high fields [Ramadan et al., 1998].

NMR and MRI are based on magnetic properties of nuclear spins that precess in the measurement field at a specific frequency. It is difficult to observe NMR/MRI signals in low field due to the reduced initial polarisation. In typical systems this magnetisation is detected as a voltage induced in an inductive coil. Therefore, the induced voltage increases as the Larmor frequency increases. Thus, in thermal equilibrium in low field as the signal is related to the rate of change of the observed magnetic signal, the polarisation is low and the magnetic signal is small.

To overcome the low initial magnetisation, NMR and MRI in low field consists of three steps; prepolarisation, evolution and detection. Prepolarisation is necessary because the initial magnetisation in low field is low and barely observable and prepolarisation is necessary to produce a significant enhancement of the bulk magnetisation. Sample prepolarisation can be achieved

by equilibration in a temporary high magnetic field transfer immediately into the low field for measurements [Blanchard et al., 2013, Ledbetter et al., 2009]. There are two other ways we can improve the signal to work better in low field. One is to exploit hyperpolarisation technique and the second is to use more sensitive sensors that coils. In this study we use a hyperpolarisation method where the polarization transfer from para-$H_2$ to molecular substrate (SABRE) in the earth's magnetic field is exploited to create a large magnetic moment [Bowers and Weitekamp, 1986].

MRI and NMR in earth magnetic field requires sensitive detectors and the most common three measurement devices used in low field NMR/MRI are inductive coils, Superconducting Quantum Interference Device (SQUIDs) and atomic magnetometers. SQUIDs and atomic magnetometers are more sensitive in low fields [Harel et al., 2008]. Although atomic magnetometers are less complex and requires no cryogens which make them of lower cost and more portability, advances in SQUIDs are growing further than those in atomic magnetometer and therefore, SQUIDs application have been used more frequently into atomic magnetometers [Harel et al., 2008].

SQUID is a magnetic flux to voltage converter of unique sensitivity with response that is independent of frequency. A growing number of studies have been using SQUID in UTF [Matlachov et al., 2004, McDermott et al., 2002, Clarke et al., 2007]. A SQUID also has the advantage of simultaneously measuring multiple different nuclei even if they have NMR frequencies that substantially different $\geq$2 [McDermott et al., 2002]. More details about the construction and performance of the SQUID coils will be discussed later in this thesis.

## 3.2 Recent developments in low field and earth's field NMR

Low field NMR measurements have the advantage that the magnetic field inhomogeneities resulting from susceptibility mismatch are much smaller [Mohorič et al., 2004]. Moreover, the relaxation of magnetisation in the longitudinal and the trans-

verse axes are often slower providing details of molecular dynamics which are hard to distinguish in a strong field NMR [Mohorič et al., 2004].

In 2004, the first publication of phantom imaging at Ultra Low Field (2-25 $\mu$T) with a sample outside a cryostat at room temperature was published. This showed that there are no fundamental limitations to hinder the anatomical or functional imaging of humans in such fields [Matlachov et al., 2004]. A $^{1}$H spectra from water and frog tissues were observed using a prepolarisation field ($B_p$) of 20 mT and a measurement field ($B_m$) of 10 $\mu$T, averaged over 100 epochs is indicated in Figure 3.1 [Matlachov et al., 2004]. These samples were placed in an open coil 1 cm distant from the sensor. Epoch-averaged data demonstrated signals within 10 Hz bandwidth (SNR $>$ 1) see Figure 3.1.

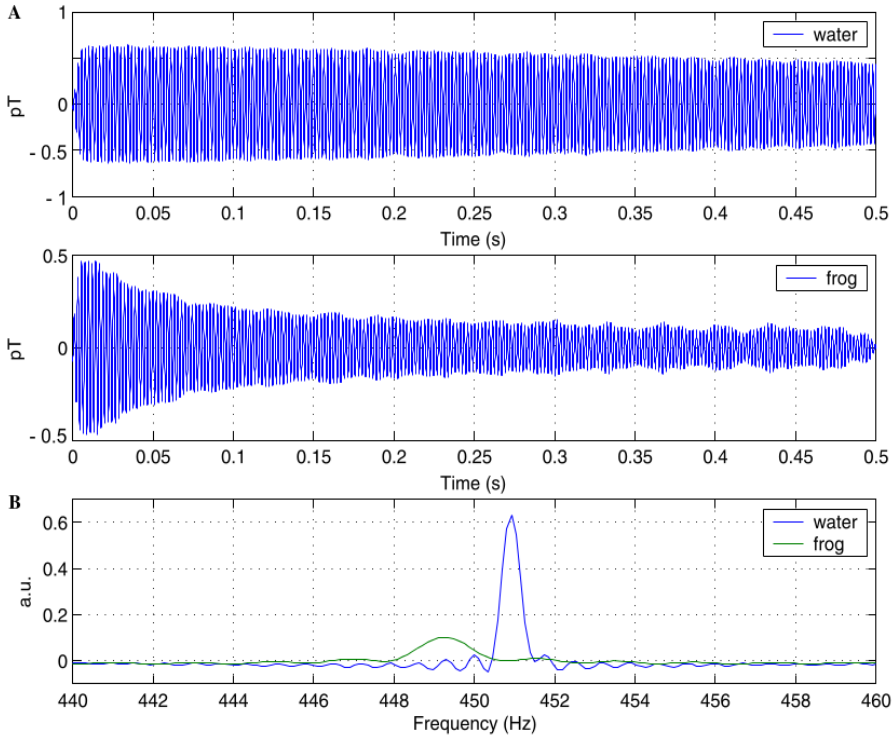


Figure 3.1: (A) Free Induction Decay and (B) $^{1}$H spectra from water and frog tissues $B_p$ = 20 mT and $B_m$ = 10 $\mu$T, Averaged over 100 epochs is indicated. Image taken from [Matlachov et al., 2004].

Furthermore, NMR measurements of samples placed into metal containers were achieved which can not be achieved in high fields [Matlachov et al., 2004]. The high frequencies of high field imaging are associated with a small skin depth in metal resulting in weak penetration of RF pulses and NMR signals

observed from the sample even in a thin conductive layer surrounding the sample [Matlachov et al., 2004]. For example, for copper at 1 T, the penetration skin depth is 10 $\mu$m and it is 10 mm at 10 $\mu$T. This problem was solved by using NMR measurements in ULF. Figure 3.2 shows the FIDs and spectra of water inside a 2 mm thick copper canister at $\approx$ 2 $\mu$T which is a useful tool for inspecting food or any biological materials inside cans.

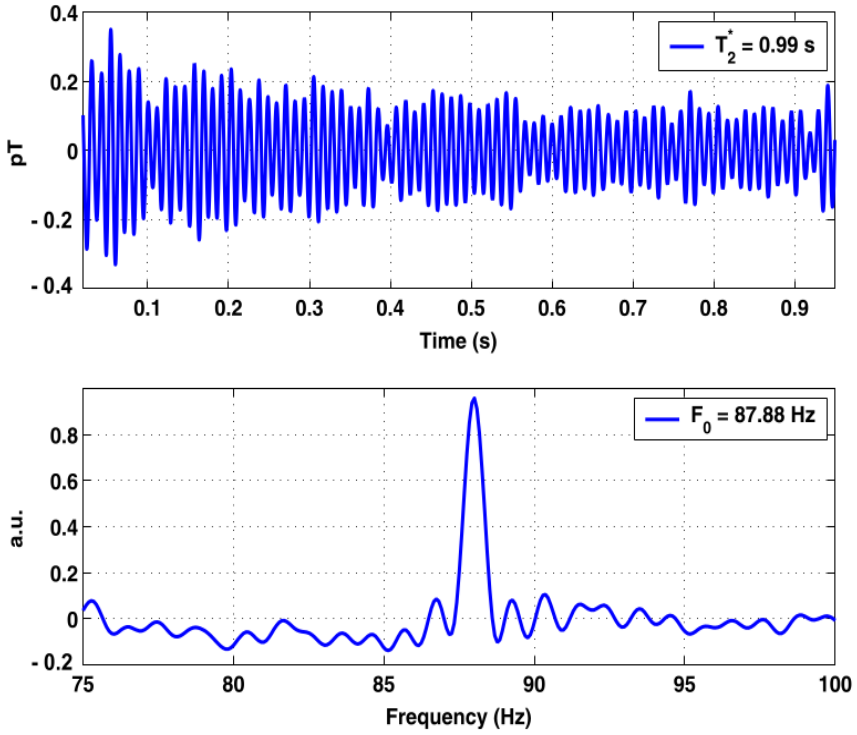


Figure 3.2: FID and spectra of $^1$H from water inside copper canister of 2 mm thickness using $B_p = 10$ mT and $B_m = 2$ $\mu$T, Averaged over 100 epochs. Image taken from [Matlachov et al., 2004].

In 2006, the first 2D correlation spectra (COSY) in Ultra Low Frequencies was reported [Robinson et al., 2006]. The magnetisation transfer occurred in heteronuclei through J-coupling and was investigated in both para-Difluorobenzene and Trifluoroethanol Figure 3.3. In the range of (kHz) frequency experiments produce spectra of quality comparable to those obtained from superconducting NMR experiments of at about 100 MHz. Because EFNMR experiments have an improved spectral resolution, with a significant magnetic field homogeneity, the use of this form of multi-dimensional NMR spectroscopy is a promising technique in regards to heteronuclear spin coupling in organic and biomolecules.

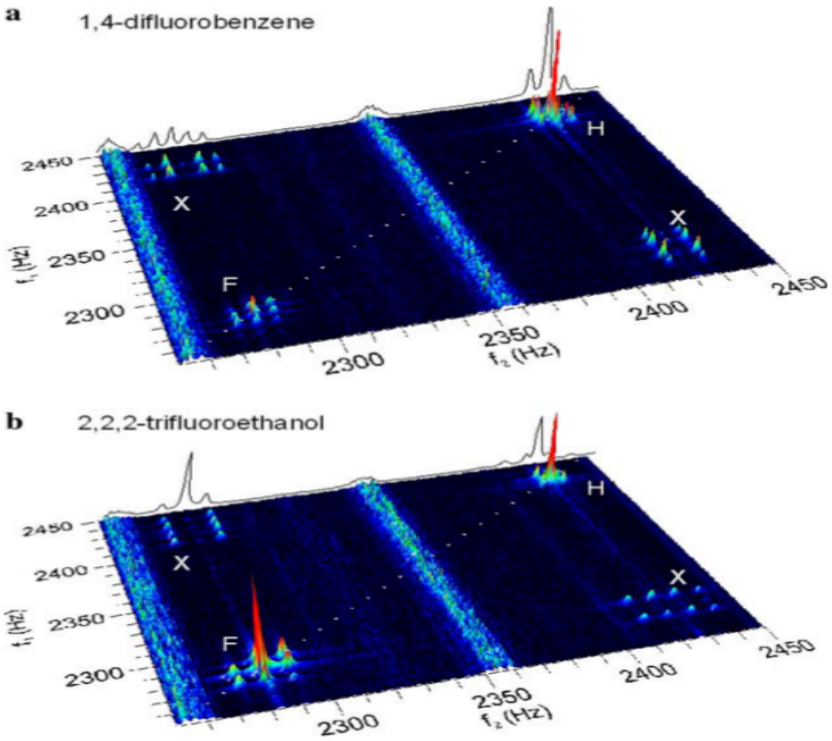


Figure 3.3: Experimental two dimensional COSY NMR spectra of a) Difluorobenzene and b) Trifluoroethanol. Both were observed at the range of audiofrequencies 2.28 kHz ($^{19}$F) labelled F, and 2.43 kHz ($^{1}$H) labelled H, while the cross peaks are indicated by x. The low frequency interference shown as streaks along $f_1$ Image taken from [Robinson et al., 2006].

An *in vivo* NMR study of human brain at 130 $\mu$T was reported [Inglis et al., 2013] using a prepolarisation field of 80 mT and the NMR signal detected using SQUID. The relaxation time $T_1$ of the scalp fat , CSF, brain tissue and blood were observed at $B_0$ and $B_p$ (table 3.1).

Table 3.1: This table shows the ${T_1}^{B0}$ and ${T_1}^{Bp}$ of different tissues. Data from [Inglis et al., 2013]

| constituent | ${T_1}^{B0}$ (ms) | ${T_1}^{Bp}$ (ms) |
|---|---|---|
| scalp fat | 96 ± 2 | 223 ± 45 |
| CSF | 1770 ± 130 | 4360 ± 600 |
| brain tissue | 141 ± 38 | 453 ± 117 |
| blood | 190 ± 39 | ≈ 450 |

For comparison, the ${T_1}^{B0}$ of tap water is about 2200 ms in these conditions [Inglis et al., 2013]. A coronal 2D images of the brain tissue were observed based on these values showing different signal intensities of different tissues with high flexibility to null or emphasise the signals Figure 3.4. For example,

it is possible to remove the CSF from the image by subtracting the image observed from the fourth echo of a CPMG sequence from that observed from the first echo. This is because CSF has a very long $T_1$ leaving the image containing only fat ,brain and blood. It is also possible to separate the CSF signal from signals obtained from other tissues, simply by allowing time for the echoes from the blood and brain to decay [Inglis et al., 2013].

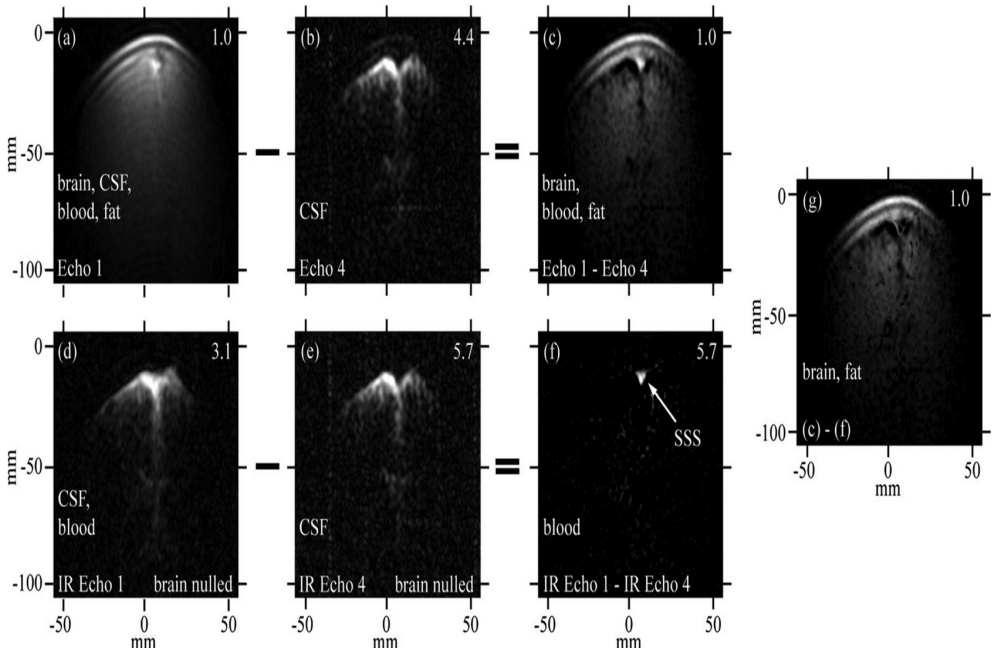


Figure 3.4: 2D images of the brain tissue using CPMG sequence interleaved with an IR-CMPG sequence (D and E) with inversion recovery delays to generate a signal null for brain tissue. C and F are the result of A-B and D-E receptively while G= C-F. Image from [Inglis et al., 2013].

One of the issues at low field is the need to ensure that the polarisation field is homogeneous. There are two issues, first eddy currents can result in unwanted fields and second, the coil design can result in a broad polarisation field distribution.The magnetic field caused by eddy currents can significantly reduced using self shielded polarisation coils [Nieminen et al., 2011]. This produces a much stronger and more controlled polarisation field than those produced by unshielded polarisation coils Figure 3.5. This also allows the production of a polarising field without inducing eddy currents in the room shielding layers. While only small amount of polarisation field at the centre of the coil is effected. This design allows the use of SQUID magnetometers for detection of signal [Nieminen et al., 2011]. Generally, axial gradiometers of sec-

ond order have been used for ultra low field MRI [McDermott et al., 2004, Zotev et al., 2007]. Commonly, the second-order gradiometers produces only small signals resulted from eddy currents. .

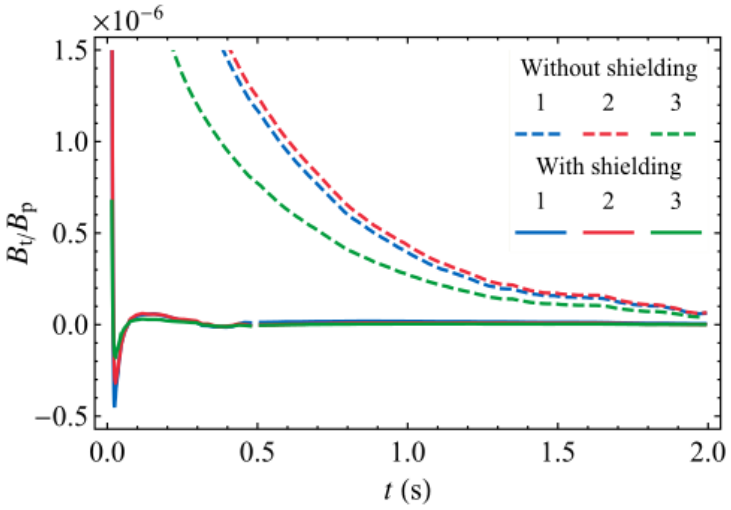


Figure 3.5: Transient magnetic field $B_t$ after switching off the polarisation coil. $t$ represent the time after switching off the coil and $B_p$ is the polarising field measured at the center of the coil. Image taken from [Nieminen et al., 2011].

In ULF MRI superconductive sensors are exploited to observe MRI signals usually in filed on the order of 10-100 $\mu$T [Nieminen et al., 2011]. Despite the highly sensitive detectors, it is important to prepolarise the sample in a stronger magnetic field in the range of 10-100 mT [Nieminen et al., 2011], which should be switched off rapidly in few milliseconds before signal detection. In addition, external magnetic interference decreased usually by situating the the ULF MRI system inside a magnetically shielded room (MSR). With typical designs of dipolar polarising coil, the stray field induces a strong eddy currents in the conductive layers of the MRS [Nieminen et al., 2011]. These eddy currents result in significant secondary magnetic fields that may distort the spin dynamics of the sample, exceed the dynamic range of the detectors. and prevents the simultaneous MEG and MRI acquisitions. A simple self-shielded polarising coil, used to largely reduce these magnetic fields caused by eddy currents. These devices can use stronger and spatially broader polarising fields than that achievable with unshielded polarising coils [Nieminen et al., 2011]. Results of unshielded coils show stronger magnetic fields with an exponential decay at longer time constant. For example, after 200 ms of polarisation

with a magnetic field of shielded polarising coil is 50 times lower than that of unshielded coils [Nieminen et al., 2011].

The substrate of SABRE hyperpolarisation has been examined in a wide range of fields (in earth's field and at 10 T using high field superconducting magnets) [Hovener et al., 2014]. It has been shown that *in situ* signal detection and quantification is possible using recently developed low field MR devices Figure 3.6. This has been done by comparing the hyperpolarisation signal with that of a thermally polarised reference. This enabled monitoring and quantification of the SABRE hyperpolarisation at the point of polarisation transfer [Hovener et al., 2014].

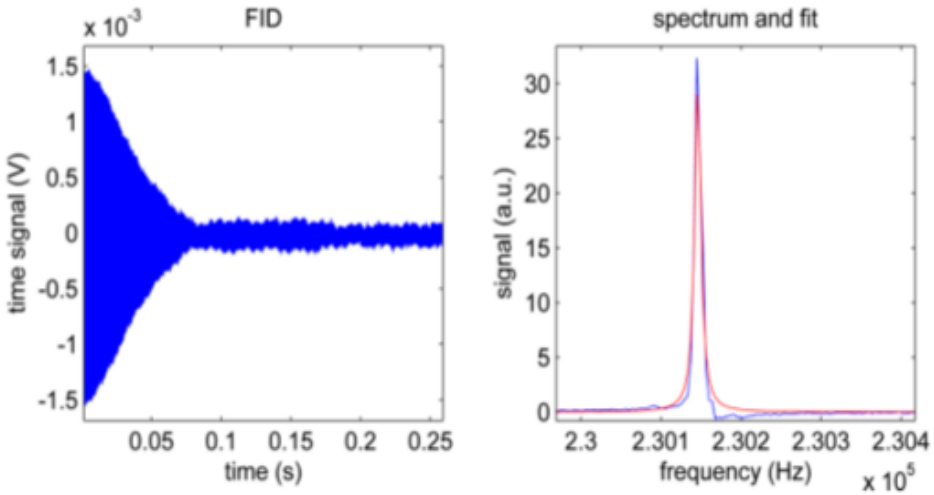


Figure 3.6: $^1$H-NMR shows a signal to noise ratio of 1.6 $\times$ $10^3$ in low field from 148 $\mu$ mol of Pyradine in 2 mM of catalyst using a 5.4 mT polarisation field. This shows that low concentration of analytes can be measured in a single acquisition. Image taken from [Hovener et al., 2014].

Pyridine showed 320 $\times 10^3$ of signal enhancement which equates to above 0.6 % polarisation of $^1$H. To produce the same polarisation magnitude in thermal equilibrium at room temperature it would require the use of around 3000 T [Hovener et al., 2014]. A further 2.5 order of signal enhancement was also observed by increasing parahydrogen from 5 to 10 bar. The transfer field ($B_s$) has a similar effect on signal enhancement of Pyridine both *in-situ* and high field measurements [Hovener et al., 2014].

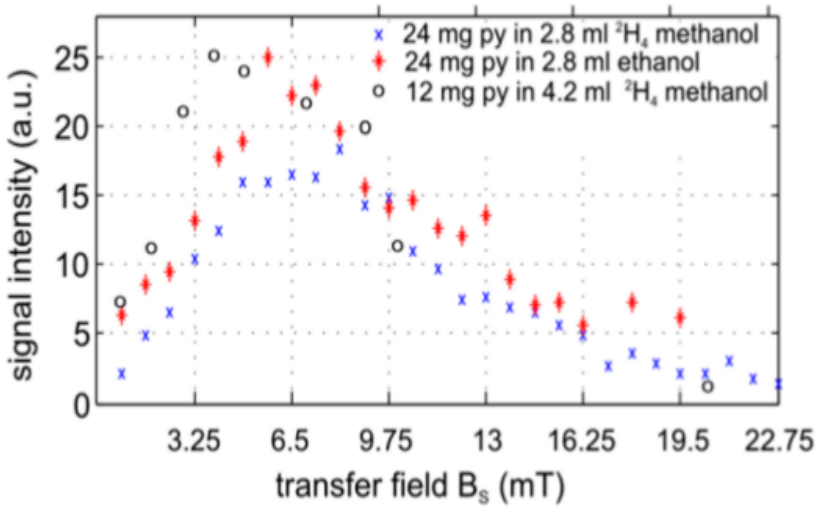


Figure 3.7: Signal amplitudes from hyperpolarised pyridine in methanol-$d_4$ and ethanol, the transfer field $B_s$ varied from 0.5 to 22 mT. Where ($\times$ and $*$) are the signals detected at low magnetic field and ($\bigcirc$) are signals detected at 7 T. Image taken from [Hovener et al., 2014].

When investigating pyridine in high field multiple frequency responses are seen, these are not seen in low fields because signals overlap over the small frequency range of chemical shift dispersion [Hovener et al., 2014]. Signal resonance observed using $^{13}$C-Nicotinamide in SABRE as a $^{13}$C MR signal but with low polarisation level [Hovener et al., 2014]. However, the longer $T_1$ of $^{13}$C (compared to $^1$H) and the invisible background allows ultrafast *in vivo* imaging using this method.

In addition, Talyer et al., 2016 demonstrated the analytical capabilities of NMR measurements Figure 3.8 by showing detection of molecules achieved via J-coupling in the zero to ULF region, less than 1 $\mu$T. This was done using fields ranged from 100 micro T to 1 mT [Tayler et al., 2016].

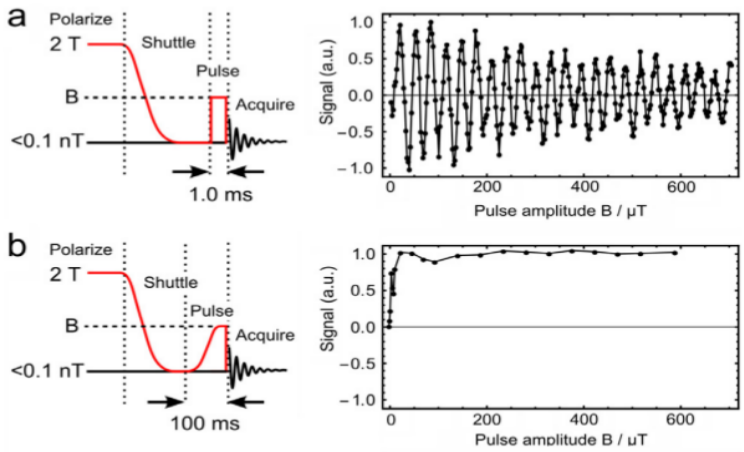


Figure 3.8: NMR Amplitudes for [ $^{13}$C]-formic acid at zero-field. Firstly, the sample was prepolarised at 2 T and transported adiabatically into the zero field. Then, the magnetic field was applied along the z axis. (a) represents a square pulse of duration 1.0 ms; (b) illustrates a hyperbolic secant pulse of duration 100 ms, for adiabatic remagnetisation. Image from [Tayler et al., 2016]

In our experiments, instead of polarising in 2 T, we can use SABRE hyperpolarisation and polarisation field of about 5 mT to create the signal and then detect it in the earth's magnetic field. The results in Section 4.3.2 will be compared to Figure 2.22 [Adams et al., 2009b] that predicts the relative amplitudes of signal vs polarisation field for different molecules for a single spin.

However, the theory in Figure 3.9 represents different molecules that have several $^1$H atoms. For example, $\hat{R}_z$ is just one atom and $\hat{T}_z$ is another atom which peaks at 5 mT Figure 3.9b. Nevertheless, in chapter 4 we use Pyrazine resonance because it has only a single $^1$H. Although there are four different $^1$H atoms in our substrate (e.g Pyrazine) they all contribute to one the same signal. Similarly, when we use Aminothiazole only see a single resonance and treated it as a single $^1$H atom unless we look at singlet states. But instead of using the triplet to singlet magnetisation, what we could have done is gone down to zero field and then see the signals which arise from more than one atom through the J-coupling. This needs different methods instead of polarising at 5 mT we would construct a device that would shield the magnetic fields going down to the range of nanoTesla.

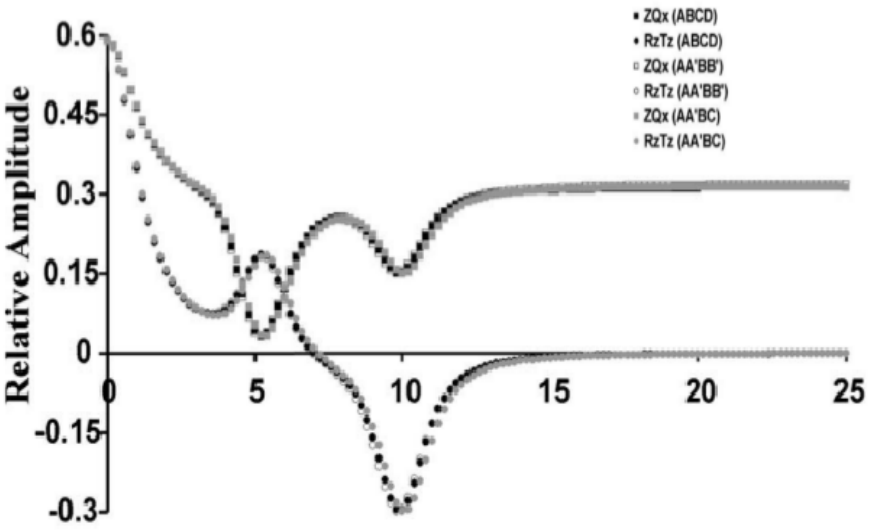


(a) The relative amplitudes for the zero quantum coherences $ZQ_x$ and longitudinal two-spin order $\hat{R}_z\hat{T}_z$.

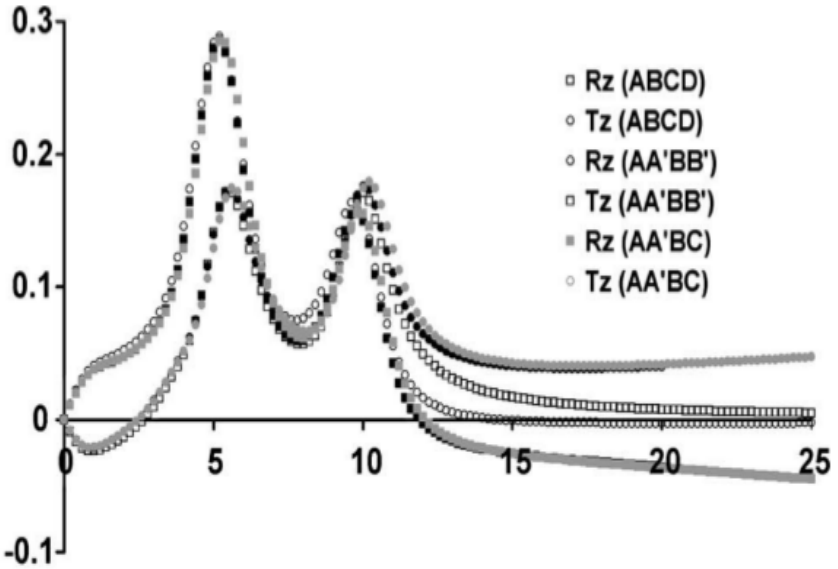


(b) The relative amplitudes for the longitudinal magnetization $\hat{R}_z$ and $\hat{T}_z$.

Figure 3.9: Mixing field dependence of the spin states made for model complexes with different spin topologies. The relative signal intensities for the zero quantum coherences $ZQ_x$ and longitudinal two-spin order $\hat{R}_z\hat{T}_z$ are illustrated as a function of mixing field over the range 0 - 25 mT (a). The relative signal intensities for $\hat{R}_z$ and $\hat{T}_z$ are also demonstrated as a function of mixing field (b). Images from [Adams et al., 2009b].

All the results in our studies will be observed based on an inductive coil used for signal detection which relies on Faraday's electromagnetic law of in-

duction. However, signal enhancement in the earth's magnetic field can be improved by using more sensitive detectors. Recently, a variety of signal detectors have been used in low magnetic field based on the study requirements. For example, the Faraday coil is preferable in Geophysical research [Legchenko et al., 2002] and in high field NMR/MRI. Using SQUID detectors is an important alternative in J-coupling investigations in low magnetic field [Bernarding et al., 2006] and for MEG and MRI detectors [Zotev et al., 2008]. In a comparison study [Dong et al., 2010], the efficiency of different detectors was compared Figure3.10. These detectors are Wire-wound resonant copper coil + Room-Temperature (RT) amplifier Wire-wound resonance Copper Coil (WCC), Printed (planar) resonant copper coil + RT amplifier (PCC) Bare high-Tc (Tuned Circuit) rf SQUID , WCC (w/o amplifier) + high-Tc rf SQUID (TSC1) (SQUID Tuned SQUID Circuit), High-Tc tape coil + high-Tc rf SQUID (TSC2) at different frequencies.

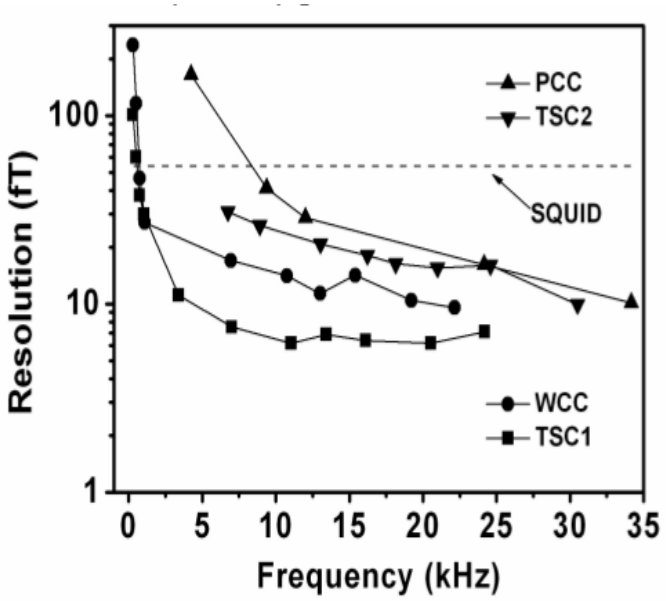


Figure 3.10: The resolution of magnetic field of different detectors Wire-wound resonant copper coil + RT amplifier (WCC), Printed (planar) resonant copper coil + RT ampl (PCC) Bare high-Tc rf SQUID (SQUID), WCC (w/o amplifier) + high-Tc rf SQUID (TSC1), High-Tc tape coil + high-Tc rf SQUID (TSC2)at different frequencies.Image taken from [Dong et al., 2010] .

It was shown that when detectors were compared in range of 300 Hz- 35 kHz a SQUID achieved the highest sensitivity. This is due to its frequency independent behaviour. The best choice for the frequency range between 2

kHz and 25 kHz is a combination of a SQUID and a wired wound copper coil detectors and TSC1. This is due to its corresponding high sensitivity and large area of detection. Another publication [Myers et al., 2007] showed that, for frequencies below 12 kHz, the most sensitive detector (in principle) is the prepolarised SQUID, an untuned detector with a gradiometer. In practice, it still the preferred modality up to about 50 kHz. Figure 3.11 shows a comparison between the noise and the signal to noise ratio of different detection modalities [Myers et al., 2007].

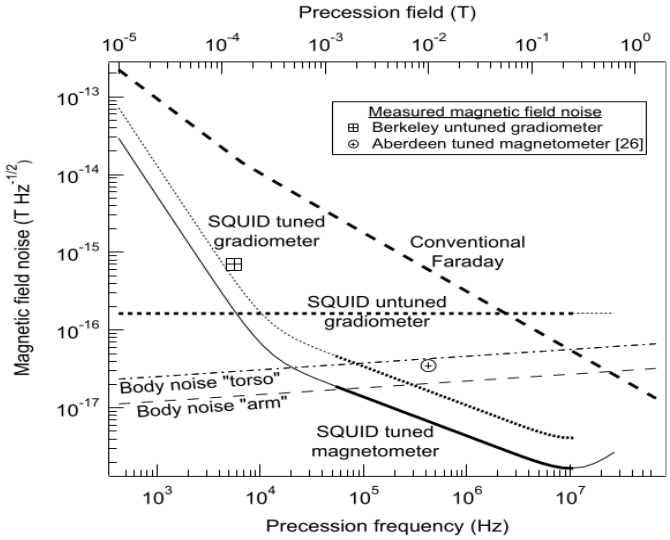


(a) Calculations represent the noise of magnetic field of tuned and untuned SQUID detectors and conventional Faraday detector with comparison to modeled sample noise. Two experimentally observed amplitudes are also illustrated. Image from [Myers et al., 2007].

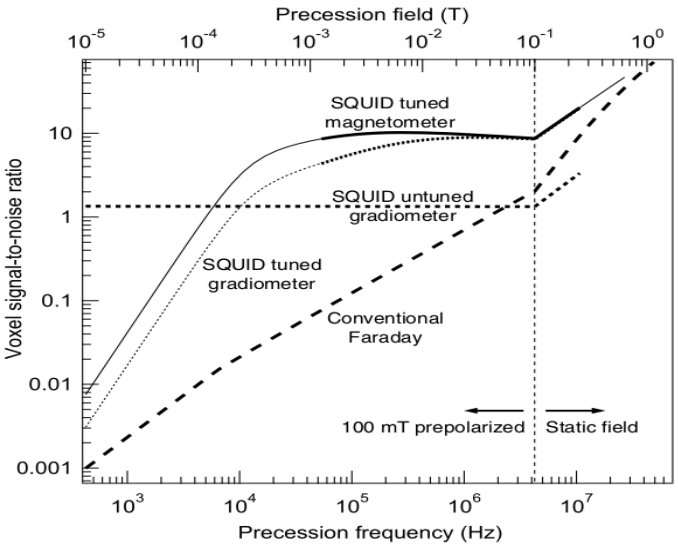


(b) Voxel SNR comparison of the four different detection modalities with prepolarization at precession fields below 100 mT. Above 100 mT the sample was polarized in the static precession field. However, the prepolarized SNR is plotted only for B 0 $<$ 100 mT . Image from [Myers et al., 2007].

Figure 3.11: Images show a comparison between different detection modalities (a) Noise (b) signal to noise ratio.

Many published works [McDermott et al., 2004, Matlachov et al., 2004] have suggested using a multichannel SQUID arrays as used in MEG for MRI detection to offer an efficient MEG/MRI neuroimaging system. This combines the sensitivity of hundreds of SQUIDs which would boost the SNR

much more than what is achieved by one detector. In a SQUID tuned gradiometer, the noise of the magnetic field decreases as the frequency increases until it approaches the level of sample noise at a crossover frequency between 90- 300 kHz based on the sample size. However, the noise of the magnetic field in a conventional Faraday detector reaches the level of sample noise at range of 4 -10 MHz and also depends on the sample size [Myers et al., 2007].

Generally speaking, SQUID untuned are the most powerful detector in low field and conventional Faraday detector is the best in high fields. However, in moderate fields SQUID tuned detectors are most suitable. Finally, the choice of detector depends on the range of frequency [Myers et al., 2007].

Therefore in a future study I would suggest the use of SQUIDs as detectors rather than the inductive coil is used. The disadvantage is the need for a cryostat.

## 3.3 The low field apparatus

### 3.3.1 Theoretical approach

The Terranova-MRI Earth's Field Nuclear Magnetic Resonance (EFNMR) (Magritek Ltd., Wellington, NZ) was used in this study to investigate NMR properties using SABRE hyperpolarisation. In high field NMR, a highly uniform field is required to polarise the nuclear spins and detect the observed magnetisation. It is challenging and expensive to produce a homogeneous magnetic field ($<$ 1ppm) and is limited to small sample sizes. However, it has the advantage that the high polarisation and detection field lead to high signal to noise ratio.

Unlike conventional high NMR instruments, the EFNMR allows measurements in the highly homogeneous earth's magnetic field. Therefore, it provides the advantage of studying large samples which in part compensating for the low detection field. In addition, it provides a cheap and portable option for NMR and MRI. However, because the measurements occur in low magnetic field the

initial bulk magnetisation is very small. To increase the initial magnetisation a pre-polarisation pulse about 350 times ($\approx$ 18 mT) larger than the earth's field is used to polarise water sample in thermal equilibrium. It should be noted that the earth's magnetic field is stable at all locations, it just has different values which are close to vertical and about 50 $\mu T$.

### 3.3.2 Design and operation

The Terranova-MRI EFNMR apparatus consists of three major coil groups. Two coaxial solenoid coils and one set consists of a group of four coils which produce gradients in the different orthogonal orientations x,y and z Figure 3.12a and 3.12b. On the x axis, there are two coils, one to perform excitation and shimming, and another one to do the measurements.

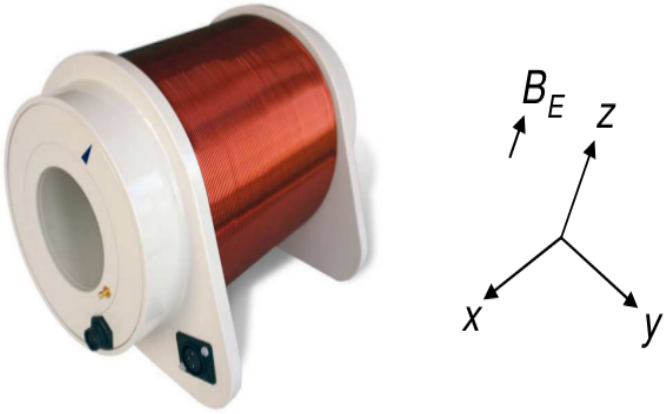


(a) The Earth's Field NMR and the axes orientations

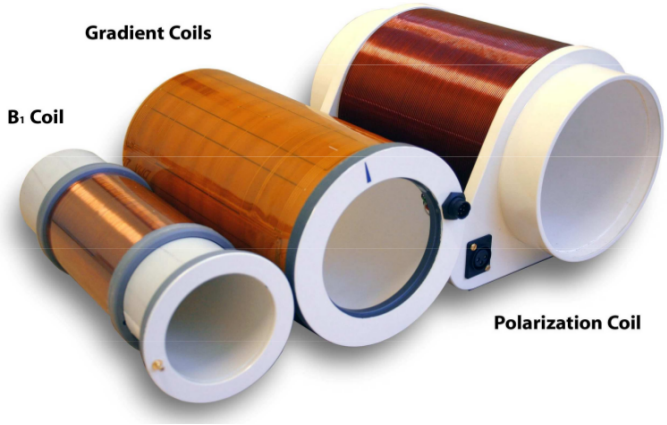


(b) The three coils of EFNMR/MRI

Figure 3.12: The Terranova-MRI Earth's Field Nuclear Magnetic Resonance (EFNMR) apparatus. Image from [Halse, 2006]

The outer most coil is the polarising ($B_p$) coil. A large current flow through this coil is used to produce a large field compared to the earth's field in order to generate initial magnetisation of the sample when placed inside the device.

In the middle are the gradient coils. These coils provide a linear gradient field gradients across the sample.

The innermost is the excitation and detection coil ($B_1$). This coil perform the excitation and detection of the resultant magnetisation. below the table (3.2) is the specifications of the three coils.

Table 3.2: Parameters of the typical coil from [Halse, 2006].

| Coil parameter | Polarising coil | Gr coils (x,y and z) | $B_1$ coil |
|---|---|---|---|
| Avg. coil diameter (mm) | 170 | 105 | 84 |
| Calc. mag. Field (mT/A) | 3.13 | N/A | 30 |
| Field gradient (mT/m/A) | N/A | 0.31, 0.28, 0.28 | N/A |
| Avg. Resistance ($\Omega$) incl. cable | 2.8 | 2.0/1.5/1.5 | 325 |
| Tuning cap for 2300 Hz (nF) | N/A | N/A | 9.7 |

**Polarisation**

It is crucial to polarise the sample before applying the excitation pulse because the initial bulk magnetisation of the sample is very small in the earth's magnetic field. This can be done when a strong current flows through the coil producing a large magnetic field compared to the measurement field. The maximum current of this coil is 6 A producing a polarising field of 18.8 mT. The current can be applied for different durations according to the experiment requirement (typically several $T_1$ periods $\approx$4 - 5 seconds). Then, the current switched off leaving the magnetisation of the earth's field direction (longitudinal plane).

It should be noticed that the current is limited by the existing power supply and the heating of the coil which may effect the apparatus and sample. If a high currents applied for long periods, at high duty cycle , it will produce considerable heating of the coil. In this case, the probe must be switched off for a period of time to allow the apparatus to cool down. If a maximum current of 6 A is applied for 4 seconds and 50% duty cycle ( 4 s on followed by 4 s off) this will dissipate 48 W with about 2 W dissipated to the sample.

### The Pulse Gradient Spin Echo (PSGE gradient) coil

This coil is specialised to produce a linear field gradient along the longitudinal axis (x-axis). As shown in table above it produces a field gradient of 2.38 $mTm^{-1}A^{-1}$ [Halse, 2006]. Because the maximum possible current is 2 A the maximum field gradient is 4.76 mT/m. The main purpose of this gradient field is to change the resonance according to the spin positions along the axis of the gradient. However, the maximum current is limited by the power supply and the dissipation of the heat in the coil due to the coil resistance as in the polarisation coil but the main difference is that the duty cycle for the PSGE coil has to be very low. For example, if two gradients of 50 ms ARE applied with TR of 4 s, so the duty cycle will be only 2.5% [Halse, 2006]. There will then be a power dissipation of only 0.3% when a maximum current of 2 A is used. The problem of heat dissipation increases as the duty cycle increases because the gradient coil is totally enclosed within the apparatus and this limits the length of gradient dimension and the shortness of the TR.

### Shimming and Imaging gradient

There are a set of three gradient coils which are used to produce orthogonal gradients and are also used to remove the background magnetic fields. This process is known as shimming. In the same time, this coil is capable of performing the magnetic resonance imaging (MRI). These coils can produce a maximum current of 200 mA corresponding to gradient of 55/63 $\mu T/m$ (z,y/x) [Halse, 2006]. The overheating is not a big issue in this coil due to the short duty cycles, low currents and resistances.

### Excitation and Detection

The $B_1$ coil is designed to perform the excitation of the sample and detect the resultant NMR signal. In a single pulse and collect experiment, a current is applied through the coil significant electromagnetic energy is produced at the Larmor frequency of the nuclei that is placed in the center of the probe in earth's magnetic field (generally 2-3 kHz). This tips the magnetisation from the longitudinal axis (z-axis) to the orthogonal axis(x,y). The $B_1$ coil then detects the x component of the magnetisation as the nuclei spin precess and relax to the z axis. The coil with an external capacitor, acts a resonance which is tuned to the Larmor frequency to remove the background signal and increase the sensitivity. Moreover, the $B_0$ coil can also acts as a as screen to remove unwanted external signals. This is done by shorting the polarizing coil during the detection phase. All fields within the $B_0$ coil are cancelled as long as they are uniform over the sample and axial in orientation, this is due to the large inductance and low resistance of the coil. This action also reduces the signal level by $\approx 20\%$ [Halse, 2006] since the signal field placed within $B_0$ coil which is considerably smaller than $B_0$ in diameter. The reduction factor of the noise is around 20 fold leading to about 15 times improvement of SNR over a non-shorted polarizing coil. Typically, if a 6 A, 4 s pulse is used with a 570 ml water sample, a peak amplitude of about 100 $\mu$V can be detected and then, amplified and digitised for display.

### Spectrometer

The spectrometer consists of digital signal processor (DSP) that controls the EFNMR experiments which itself receives commands from a separate computer that runs the data processing package *Prospa*. To run an experiment, all necessary data and commands are sent through the PC's USB port from Prospa to the DSP unit.

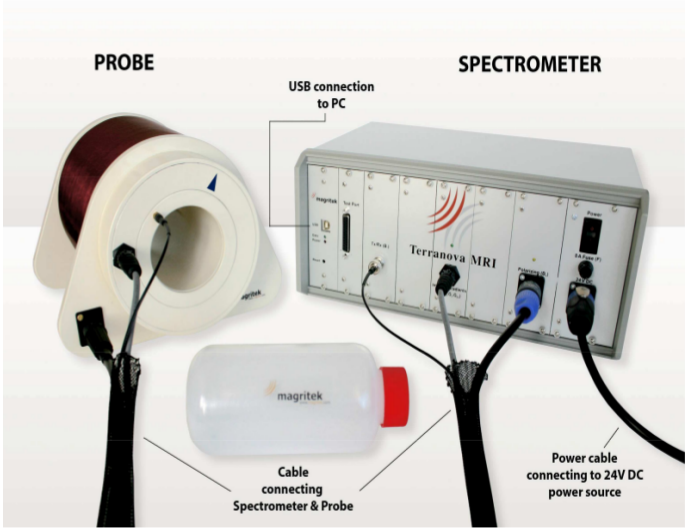


Figure 3.13: The spectrometer and probe of the EFNMR system. Image from [Halse, 2006].

This program sends all information about the the $B_p$, the gradients and the $B_1$ coils. It also collects the measurement signal from the $B_1$ coil via the DSP. The PC used to analyse and display the results. Then, the experiment is ended or can be repeated again if required. Shown in Figure 3.13 is a central box that contains the set of electronics including the DSP. The PC and spectrometer are connected via a USB interface. There are also cables connecting the power supply to the $B_1$ coil and other cables connecting the spectrometer to different the coils [Halse, 2006].

In my thesis some of the Terranova-MRI experiments are executed using Prospa software (Magritek Ltd., Wellington, NZ). Prospa was also used to manipulate and analyse data. However, a set of Python commands arranged in several scripts were also used to control the probe automatically. This allowed a were flexible option to run long and complex experiments. This will be described in more detail later in this thesis.

## 3.4 Set up of the EFNMR instrument

Before we start the measurements the instrumental set up was such that the power supply, PC, spectrometer and the probe were kept some distance away from each other to avoid any electrical or magnetic interference. The

three components of the EFNMR probe were connected to the spectrometer as shown in Figure 3.14.

(a) connecting the polarising coil

(b) connecting the gradient coil

(c) connecting the $B_1$ coil

Figure 3.14: The methods of connecting the cables of the probe

The amplitude of the NMR signal and noise are significantly affected by the orientation of the probe. A conventional compass was used to measure the magnitude and the direction of the earth's magnetic field in the experiment room. The probe was rotated so that the longitudinal (x) axes was orthogonal to the earth's field direction.

(a) Using the compass to find the prober orientation of the probe

(b) The orientaion of the EFNMR probe

Figure 3.15: (a) Using the compass to tilt the probe with the earth's magnetic field. (b) The best direction of the probe.

When all connections and the orientation of the system was set up properly, the next step was to evaluate the system by running some basic experiments from the Prospa software loaded on the PC.

## 3.5 Homogeneity of earth magnetic field

The lack of homogeneity of the natural earth's magnetic field may affects the experimental results and may result in non accurate measurements. Therefore, to ensure a homogeneous field it is important to locate the probe in the most appropriate place about 2 meter distance away from any ferrous materials that may effect field homogeneity. The NMR experiments were conducted in a non shielded room. The fields within the experiment room were measured precisely. The earth's magnetic field was measured in each square of half a meter in x, y and z axes all around the room using (GM08, Hirst magnetic instruments, UK) to find out the most stable field and homogeneous location while three separate measurements on different axes were required for each point. Data was collected a bout 1 meter high above the floor level and contour maps were plotted using Python. Figures 3.16a and 3.16b show a contour and vector maps throughout the experiment room respectively. The contour map indicates the magnitude and direction of the field.

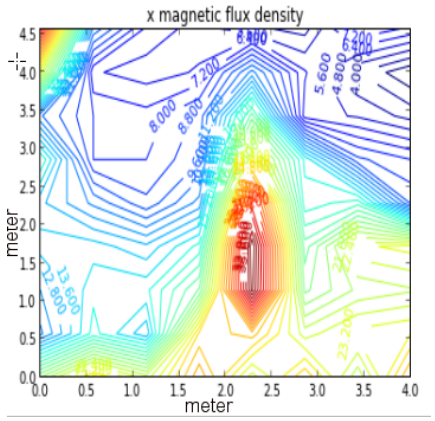


(a) Contour map of the magnetic field density

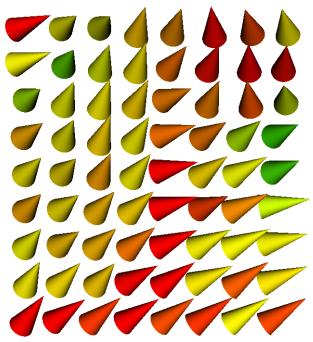

(b) External magnetic field alignment

Figure 3.16: Illustrated is maps of magnetic flux density and directions

When the field measurements were taken, the probe was placed in the location of the experiment room where the earth magnetic field was homogeneous and close to the longitudinal axis as shown in Figures 3.16a and 3.16b. The device was located in a displacement between 2.0 m, 3.5 m on the y axis and between 0.5 m, 1.5 m on the x axis) on the left corner of each image Figures 3.16a and 3.16b.

## 3.6 Optimising the Free Induction Decay (FID)

### 3.6.1 Tuning the $B_1$ coil

Once a position of good homogeneity was located a 500 ml sample of tap water was used and the FID optimised by tuning the coil, adjusting the $B_1$ frequency, finding the suitable $B_1$ pulse by calibrating the pulse duration and removing the background noise.

In order to optimise the SNR in the EFNMR probe it is essential to tune the probe correctly to the Larmor frequency of the sample. This was done using Prospa to run an *analyse probe* experiment to establish the appropriate tuning. This process maximizes the signal to ensure that signals are not decreased by not placing the coil resonance frequency at that of the sample Larmor frequency. To do this, a simple pulse and collect experiment was conducted on 500 ml of water sample using a prepolarisation field of 18.8 mT for 4 s and a short delay between the excitation pulse and the acquisition (acquisition delay 2 ms). The delay was set to avoid measuring the ring down signal of the coil.

Usually, the initial signal superimposes by sinc-like function Figure 3.17. The side sinc-like function is due to the coil affected by $B_1$ pulse, and the narrow pulse on the right side of the spectrum is the NMR pulse 3.17. In some cases, where the sample peak is very strong the ring down sinc function becomes undistinguishable. In this case it is important to reduce the signal intensity of the sample by reducing the polarisation duration.

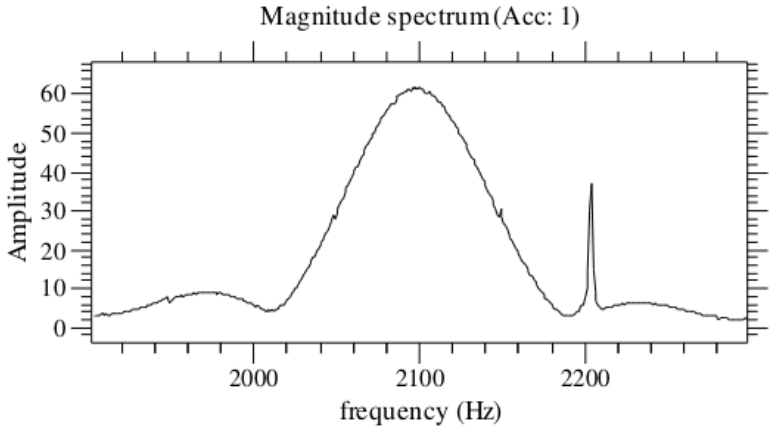


Figure 3.17: Signal from water sample as a result of incorrect tuning using 2 ms acquisition delay and 90 excitation pulse

The Capacitance of the system is controllable by Prospa software to match the appropriate resonance frequency until the maximum of the sinc function and the centre of the sample peak coincide Figure 3.18.

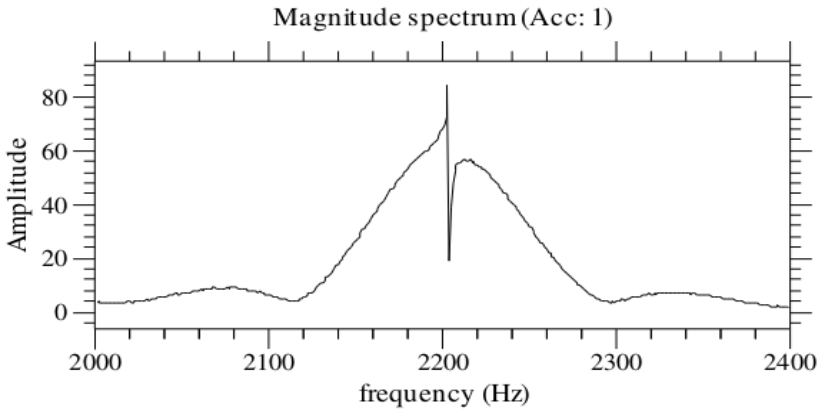


Figure 3.18: Plot indicates how the maximum of the sinc function and the centre of the sample peak coincide. Image from [Halse, 2006].

Repeating the pulse and collect experiment with an acquisition delay of 25 ms will result in an enhanced signal intensity Figure 3.19.

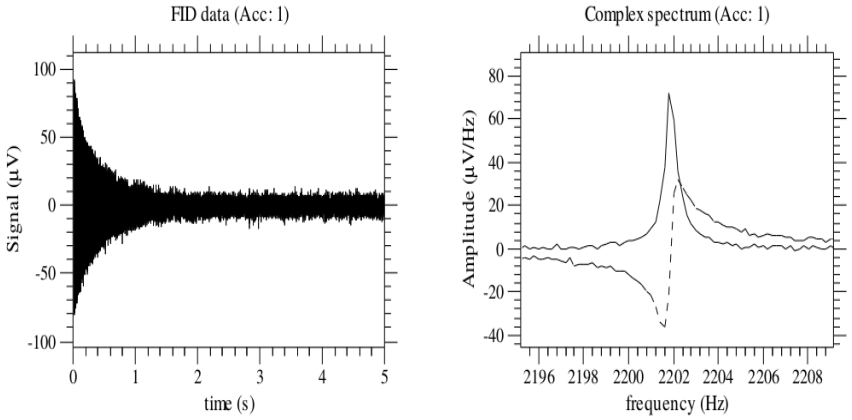


Figure 3.19: FID acquired for 5 seconds to show how the signal amplitude enhanced. Image from [Halse, 2006].

The frequency of the resonance peak in the spectrum can be measured as the second step to optimise the FID. the frequency amplitude is used as the $B_1$ frequency in the further experiments.

### 3.6.2 Shimming

Once a signal has been obtained, it can be optimised by shimming. Shimming is performed in an automatic manner to remove the background noise and set the magnetic level gradients in the earth's field. The pre-polarise pulse and collect sequence are repeated several times with range of shim current values (in the order of a few mA) to the three orthogonal coils until the signal reaches a maximum peak height. The effect of each shim current can be assessed by the size and the shape of the FID. The time domain decay lengthens as the overall homogeneity field increases. Therefore, the linewidth of the peak decreases in the frequency domain and then, the peak height increases Figure 3.20.

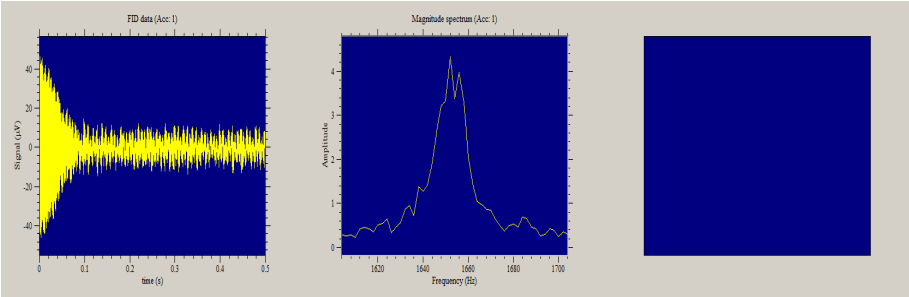


(a) Signal shape 5 seconds after starting the shimming process

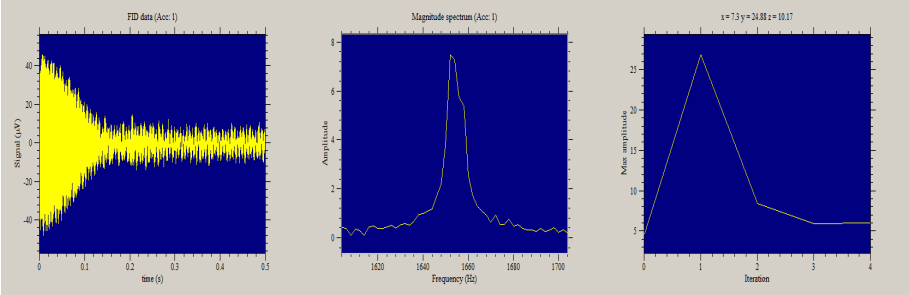


(b) Signal shape 60 seconds after starting the shimming process

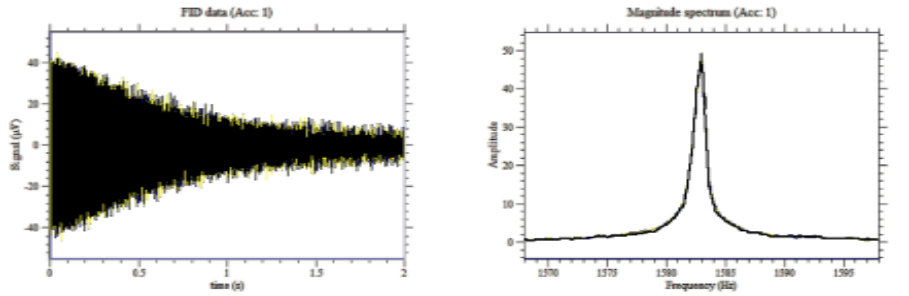


(c) The spectrum and FID of 500 mL of water observed immediatly after single shake and drop

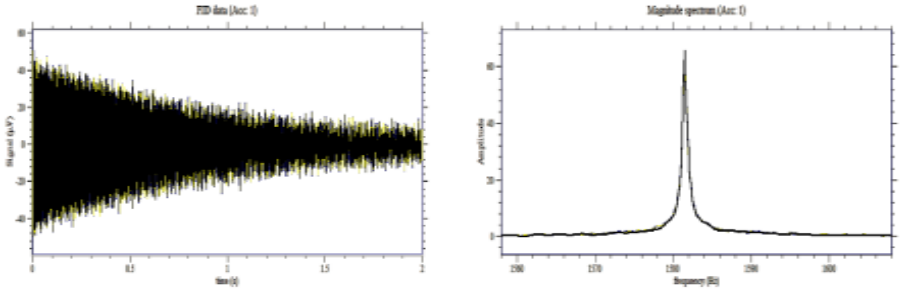

(d) The spectrum and FID of the hyperpolarised sample immediatly after single shake and drop

Figure 3.20: The resultant FID, signal and signal integration of Autoshimming in different days

The auto shimming process was performed on a daily basis to ensure an efficient and homogeneous field for each experiment. Figure 3.20 above shows the progress of the FID and signal peak during the auto shimming.

# Chapter 4

# Factors affecting SABRE signal enhancement in EFNMR

## 4.1 Introduction

Enhancing the sensitivity of NMR produced from SABRE hyperpolarisation is of great interest for spectroscopic and MRI investigations. A large number of variables affect the efficiency of SABRE [Lloyd et al., 2014]. In order to achieve the highest enhancement it is important to optimise the parahydrogen spin transfer conditions. Although most studies treat SABRE only in high magnetic field in this thesis the nature of signal enhancement derived from SABRE in the earths magnetic field is investigated. Many factors can be considered in order to improve the SABRE method in low magnetic field. In this chapter, these important factors, that influence SABRE signal enhancement, are manipulated and the the observed outcomes are discussed. To ensure the highest NMR signal we investigate each factor separately whilst other factors are fixed and use the optimal values as default in later experiments.

The following sections will deal with :

First, calibrating the flip angle dependency for different substrates including pyrazine, nicotinamide and aminothiazole. The observed curves of the

field dependency were fitted for each substrate and compared to that of water. Flip angle dependency was investigated using a fixed duration transmit pulse and the transmit gain was parametrically explored. This was done by using a 1.5 ms transmit pulse. As the experiments are done in the earth's field, the frequency of the transmit pulse was always between 2 and 3 KiloHertz. If the transmit pulse duration is short compared to the period of the pulse frequency, the pulse might have less than a period in duration and the bandwidth dramatically increases.

Second, the best polarisation field and polarisation duration, that achieves the optimal polarisation transfer, and therefore the maximum signal enhancement in pyrazine were observed. After that, a variety of measurements were done to investigate SABRE signal properties in the earth's magnetic field such as measuring the optimal signal enhancement per mole of pyrazine compared to that of water.

Furthermore, the decay of the hyperpolarised signal was measured as a function of time demonstrating the possibility of using the hyperpolarised signal several times for a long time. The effect of parahydrogen pressure on the observed signal was also investigated, this was done by comparing the signal from using parahydrogen at 3 bar pressure to that of observed using parahydrogen at atmosphere pressure by releasing the air at the top of the test tube in contact with the liquid sample. The effect of shaking the sample several times separated by fixed increments and how the signal amplitude decreases in each consequent shake was studied. This was used to explore the life time of the parahydrogen in the head space and its decay caused by dissolving the gas and its interaction in the SABRE process.

The effect of immersing a heart tissue in the liquid sample on the signal decay was also investigated. The hypothesis was that if the substrate interacted with the tissue then one might predict a more rapid relaxation of the hyperpolarised signal.

Finally, 2D imaging was achieved employing the optimal parameters of the previous measurements.

## 4.2 Parahydrogen production

When Hydrogen is used in normal conditions and at normal pressure, no enhancement can be observed by using this in the SABRE process. At first glance this is surprising as at room temperature, Hydrogen gas contains 25% parahydrogen and one might expect an enhancement that is one quarter that achieved when pure parahydrogen is used. Therefore it is necessary to investigate the condition under which parahydrogen must be used in the SABRE process.

To achieve this it is necessary to start with high partial pressures of parahydrogen where the SABRE effect is known to be observable. To do this it is necessary to cool the Hydrogen gas Figure 4.2, in the presence of a surface catalyst, until the parahydrogen becomes dominant. The proportion of parahydrogen is highly dependent on the temperature. As the temperature decreases the parahydrogen concentration increases until it reaches 100% at 20 K.

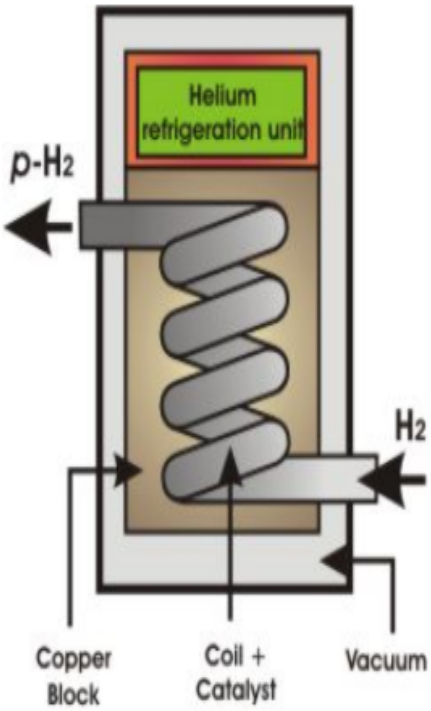


Figure 4.1: Schematic representation of the parahydrogen generator used at the Hyperpolarisation Centre in the University of York.

A catalyst (e.g activated charcoal) can be used to speed the process of changing

orthohydrogen to parahydrogen. When the influence of catalyst is removed, and the gas returns to the room temperature, the concentration of parahydrogen remains for hours and changes back to the normal distribution at a very slow rate as the without the catalyst the transformation is said to be a forbidden transition from the singlet to the triplet.

Figure 4.2: A picture of the in house developed parahydrogen generator used in this study.

## 4.3 Exploring the pyrazine signal enhancement from single shake and drop experiments

Typically, fresh parahydrogen is supplied from the parahydrogen generator to the headspace of the tube in each experiment. Then, the sample is shaken

manually for 10 seconds in the earth's field and dropped in the center of the NMR probe to start the measurements. The pulse sequence typically consists of a polarising field which is applied for about 4-6 seconds and turned off. This is followed by the excitation pulse (usually 90 degrees) and then after a suitable delay, the $^{1}$H FID is detected from the hyperpolarised substrate in the earth's field Figure 4.3.

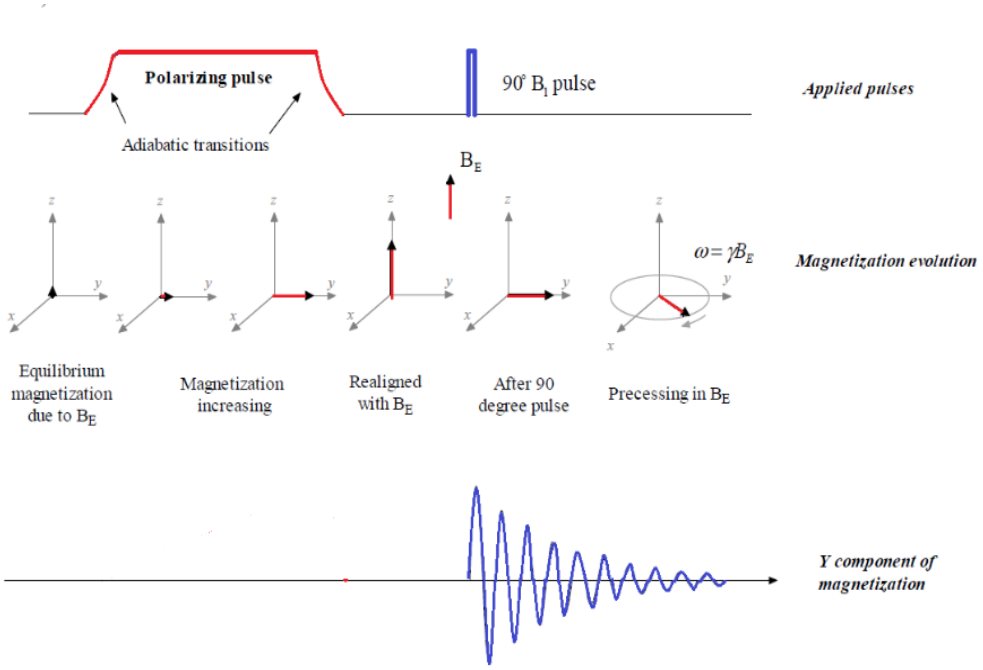


Figure 4.3: The simple pulse and collect sequence. Image from [Halse, 2006]

Using a 10 mm tube fitted with Young's tap, a liquid sample consisting of 25 mg (1.25 mM) of pyrazine in 3 mL $d_4-$methanol and 10 mg [Ir(IMes)(COD)cl] catalyst is studied in the earths magnetic field. In thermal equilibrium the proton signal is very low and not distinguished from the noise signal such that it is undetectable. However, when fresh parahydrogen is dissolved in the sample, the SABRE process occurs and a significant signal is observed indicating a strong SNR enhancement. This simple procedure was exploited to define the optimal conditions in order to produce the maximum signal enhancement.

The following sections describe a range of measurements that investigate the effect of many factors on the hyperpolarised signal in the earth's magnetic field to optimise the signal including flip dependency, polarisation field, polarisation

duration, signal decay as a function of time and the effect of changing the number and timing of sample shakes to dissolve parahydrogen in the solution.

It should be noted that before very experiment, a large water sample (500 ml) was used to find that day's value for the earth's magnetic field and the corresponding Larmor frequency to be used for transmit and receive coil tuningenergy. This was performed using a simple polarising field of 18 milliTesla following by a transmit pulse. The subsequent FID was recorded and the frequency of the proton signal was determined from the FID.

### 4.3.1 Flip dependency

In order to optimise the NMR signal, the 90° and 180° RF pulses must be defined accurately. This can be achieved either by varying the duration or amplitude of the RF pulse. The gain was varied here as the frequency of the proton signal in the earth's field is so low that it is not desirable to have transmit pulses that have less than one period.

The sample was prepared as described in Section 4.3 by varying the transmit gain and keeping the flip duration fixed. When the transmit amplitude of the transmit pulse is zero no magnetisation flips to the transverse axis. However, as the amplitude increases the amount of the transverse magnetisation and therefore the NMR signal increases until it reaches the peak at 90°. If we keep increasing the transmit amplitude the signal decreases until it reaches the minimum level at what we define to be 180°. We assume that a sinusoidal shape of the flip dependency curve will represent the observed data.

The solution was degassed using three freeze-pump-thaw cycles. Parahydrogen was produced as previously described in Section 4.2 by cooling the $H_2$ gas to 28 K temperature and was introduced into the tube at a pressure of 3 bar. The tube was then transported close to the NMR probe, shaken for 10 seconds in the earth's magnetic field ($\simeq 50\ \mu T$ ) about 10 cm distance from the scanner to dissolve para-$H_2$ in the liquid solution. The sample was then placed into the center of the NMR probe for immediate investigations.

The flip dependency of 500 mL of water and SABRE hyperpolarised samples containing 10 mg catalyst, 25 mg (pyrazine, Nicotinamide or Aminothiazole)

in 3 ml $d_4$−methanol were compared. This was done by adjusting the $B_1$ transmit gain and keeping the pulse duration fixed at 1.5 ms in all samples. It should be noted that the concentrations of these substrates and all other conditions are the same to allow a direct comparison between them as it was previously proven that the concentration of substrates and catalysts influence the signal enhancement [Mewis et al., 2014]. The transmit gain was varied from 0 to 10 while the following parameters were used: Polarising current 6 A (equivalent to a field of 18.8 milliTesla), polarising duration 6000 ms, $B_1$ freq 2860 Hz and TR 12 s. The total scan time for each experiment was about 480 seconds. The best polarisation fields for each SABRE sample were used based on measurements collected in Section 4.3.2. Signal amplitudes of each sample were observed as a function of transmit gain, then the relationship was plotted and compared with that of water and all other SABRE samples. Data points corresponding to a range of pulse gains were analysed and a sinusoidal curves were fitted using Python. The flip angle can be deduced from the graphs Figure 4.4 below.

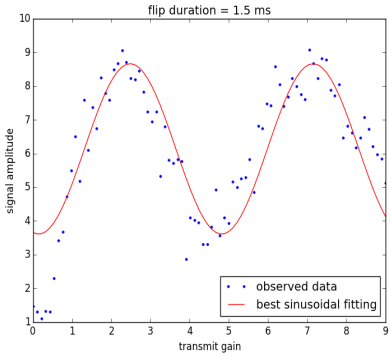


(a) water

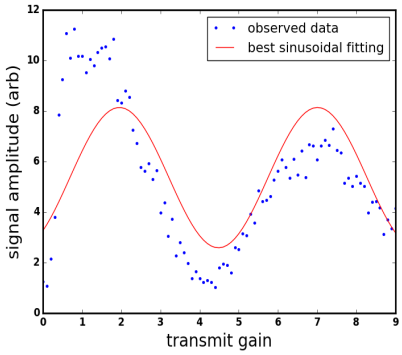


(b) Pyrazine

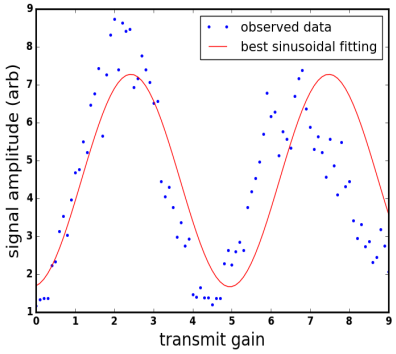


(c) Nicotinamide

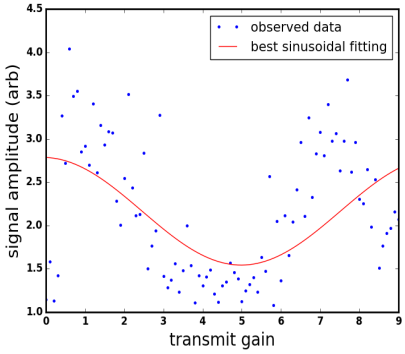


(d) Aminothiazole

Figure 4.4: Results showing the signal amplitude vs transmit gain from 0° to 360° for different molecules. Fitting a sinusoidal curve to the observed data showed a close agreement between the observed data and the fit line for water measured at thermal equilibrium. However, There is a clear deviation between observed data and sinusoidal line for the other three hyperpolarised samples. The deviation is at its maximum in the Aminothiazole sample while it is smaller for both pyrazine and nicotinamide.

The best sinusoidal fitting of the water sample at thermal equilibrium and those for pyrazine, Nicotinamide and Aminothiazole were compared in Figure 4.5.

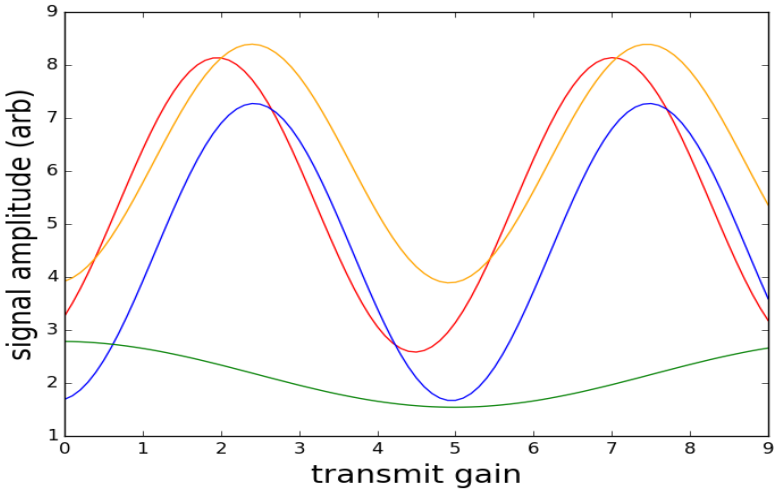


Figure 4.5: A best sinusoidal line fitted to the observed data in the flip angle dependency experiments.

From figure 4.5 it is clear that pyrazine and Aminothiazole 90° are about half the value of that of water being 1.17 and 0.97 in pyrazine and aminothiazole respectively. While the 90° of Nicotinamide requires more gain and even bigger than that of water at 2.17. However, although the 90° in pyrazine and Aminothiazole are smaller than those of water and Nicotinamide, the 180° angles at 6.90 and 7.40 respectively, can be compared to 6.42 and 6.62 in water and Nicotinamide respectively.

The best sinusoidal line was fitted to the flip dependence curve of pyrazine Figure 4.4b. It is clear from the graph that the observed data are slightly shifted from the sinusoidal fit line especial in the region of the maximum signal amplitude that represents the 90 flip angle. That is to say, the observed 90 degree was in 1.17 of the transmit gain axis while the 90 degree of the fitted line was at about 2.1 on the same axis. However, the 180 and 270 degree of the observed and sinusoidal curve are more matched to each other with differences less than 0.4 on the transmit gain axis (the 180 degrees were 4.2 and 4.5 and the 270 degrees at 7.1 and 6.9 for the observed and the sinusoidal curve).

### 4.3.2 Polarisation field dependency

#### Polarisation field strength

According to the theory of the mechanism of SABRE, the maximum enhancement is reached when the chemical shift frequencies of the protons are of the same order as those of the scalar couplings [Adams et al., 2009b]. However the optimal polarisation field is not predictably straight forward as multiple scalar coupling occur in the molecules studied in this thesis. Nevertheless, it can be observed practically by varying the magnetic field and observing the relevant signal amplitudes.

To measure this, samples were prepared by dissolving 10 mg of [Ir(IMes)(COD)Cl] catalyst and 25 mg of substrate (pyrazine) in 3 ml solvent $d_4-$methanol using 10 mm tubes fitted with a Young's tap. The solution was degassed using three freeze-pump-thaw cycles. Parahydrogen was produced as previously described in Section 4.2 by cooling the $H_2$ gas to 28 K temperature and was introduced into the tube at a pressure of 3 bar. The tube was then transported close to the NMR probe, shaken for 10 seconds in the earth's magnetic field ($\simeq 50\ \mu T$ ) about 10 cm distance from the scanner to dissolve para-$H_2$ in the liquid solution. The sample was then placed into the center of the NMR probe for immediate investigations.

Figure 4.6 shows how the relative amounts of the free substrate magnetisation varies with the polarising field strength over a range of 0-18.8 milliTesla for four different substrates and compared to that of water. These substrates were chosen because of their biological functions; Nicotinamide [Rovedo et al., 2016], aminothiazole [Olaru et al., 2016] and pyrazine [Roy et al., 2016b].

A number of polarising fields were used for 6 seconds. A 90° pulse was used to flip the magnetisation into the transverse axis. The experiment was achieved by increasing the current to the polarising coil from 0 to 6 A in small steps. The polarising coil requires a 6 A current to produce the maximum polarisation field of 18.8 mT. Python was used to plot a curve of observed signal intensities as a function of polarising field strength.

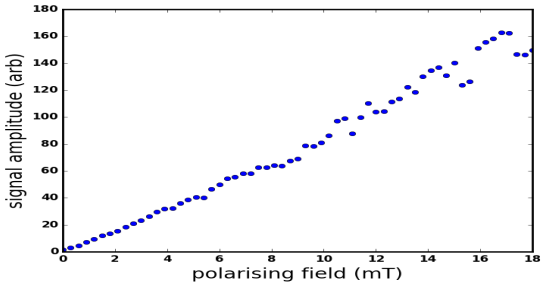


(a) water in thermal equilibrium

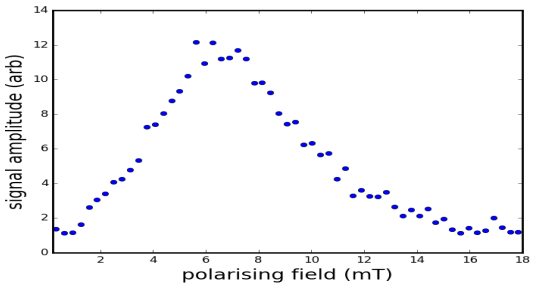


(b) hyperpolarised pyrazine

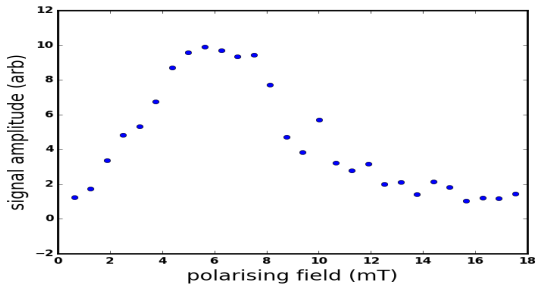


(c) hyperpolarised Nicotinamide

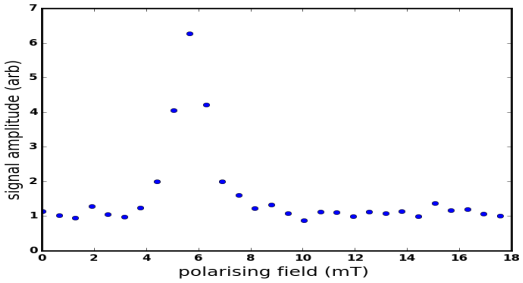


(d) hyperpolarised Aminothiazole

Figure 4.6: Four plots showing how the polarising field affects the $^{1}$H NMR signal amplitude observed from different molecules (water, nicotinamide , pyrazine and aminothiazole). The polarising field varied from 0 to 18.8 mT and data observed were compared.

The results show that the $^1$H NMR signal from the water sample at thermal equilibrium is directly proportional to and increases linearly as the polarisation field increases until it reached the maximum signal enhancement at 18.8 mT which is the maximum field possible for the coil Figure 4.6a. However, the other three plots Figures 4.6c, 4.6b and 4.6d) show very different relationships than that seen with water. In these cases, the $^1$H NMR signal amplitude is 0 at zero field and increases gradually as the polarising field increases until it approaches a maximum enhancement at a particular field and decreases gradually back to baseline at higher polarising fields. In hyperpolarised Nicotinamide for example, the $^1$H NMR signal enhancement starts to increase at 1.8 mT to reach the peak at 5.6 mT and reduces to match the level of the background signal at 15.0 mT. Pyrazine enhancement shows the same behaviour as with nicotinamide and the maximum signal is reached at 6.13 mT while the curve extends from 1 mT to 14.5 mT. Finally, the Aminothiazole dependency illustrates a narrower area of enhancement as a function of polarising field compared to nicotinamide and pyrazine. That is to say, the region of signal enhancement lies only between 2.8 mT and 8.6 with a maximum enhancement at 5.4 mT. Results in Figure 4.6c, 4.6b, 4.6d show that the maximum signal enhancement achieved with the amplitude of polarisation field was about 6.5 mT which is close to 7.0mT maximum obtained by Cowley et al. for pyridine [Cowley et al., 2011]. In the next experiment, the duration of the polarising field was varied at the optimal magnetic field of 6.5 mT as will be described in the next section.

Figure fig:field-dependencies demonstrates the critical fields for signal enhancement in different samples. These best fields have been used as the default in the following experiments in order to optimise the signal enhancement using SABRE.

Thus it can be clearly seen that with water, the signal simply and linearly depends on the polarising field. This is predictable in that that the population distribution of spin states in any molecule at thermal equilibrium is given by the Boltzmann distribution and the direct dependence on the polarising field. Over such as small range it would be expected to be linear. But the clear deviation from linearity for the other molecules shows that the process at

work is not that predicted from the Boltzmann distribution. It is also the case that the signals are from very small concentrations of substrate and thus the enhancement of the signal is much greater than that of water. This the SABRE process and is due to the transfer of magnetisation from parahydrogen to the substrate. The field dependency shows different peaks for each of the substrates studied here. This would be expected in that the scalar couplings differ across these three molecules. Scalar couplings are molecule dependent, so it could be hypothesised that if this experiment were to be repeated many times, for many molecules, the polarising field bringing about the highest enhancement would be representative of the bonds within the molecule.

**Polarisation duration dependency**

The next set of observations was completed utilising a liquid sample (10 mg of [Ir(IMes)(COD)Cl] catalyst and 25 mg of pyrazine as a substrate in 3 ml of $d_4$-methanol) with dissolved parahydrogen. Again the sample shaken for 10 seconds to dissolve parahydrogen into the solution, it was then placed in the center of the probe. After a brief period that allowed the sample to settle and to avoid the effect of the shaking process measurements were began in which the polarisation duration was varied whereas the optimal polarisation field remained constant (at 6.5 mT) because this was the optimum $B_p$ from the measerments recorded in Section 4.3.2. The results of these measurements are shown in Figure 4.7. There was evidence of changes in polarisation which generally increased with polarisation duration. For the hyperpolarised signal, the maximum enhancement level was reached at about a polarisation duration of 60 s. It was followed by a plateau from 60 s to 180 s when the signal was fairly constant. The maximum used polarisation duration was limited to 180 s. Although dedicated Python commands were used to control the whole experiment, the polarisation coil shuts down automatically when the polarising duration exceeds 180s, this is a safety procedure to protect the coil from overheating which may damage the system and also heat the sample.

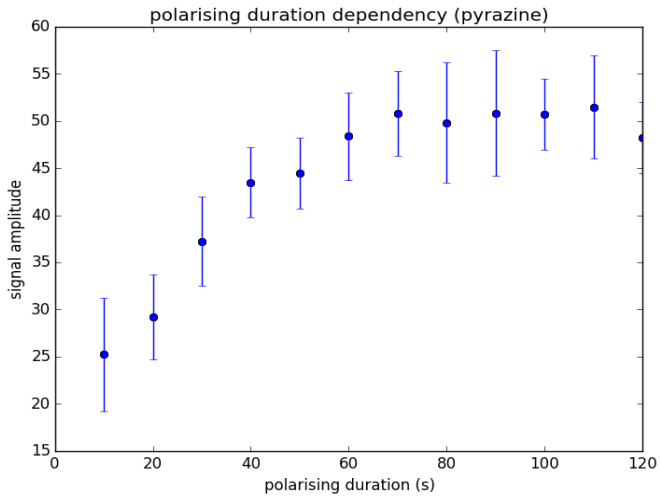


Figure 4.7: The effect of polarisation duration on signal intensity.

Interestingly, it is not feasible to evaluate the rate at which the polarisation builds up in the solution if the same experiment above was done immediately following the shake of the sample. This is because that the signal will not only be influenced by the polarisation field and duration but also due to the effect of the physical shaking of the sample. When the sample is shaken, large amount of parahydrogen dissolve from headspace of the test tube into the liquid sample. The amount of this bulk dissolved parahydrogen decreases quickly in a few seconds Section 4.3.3.

Therefore, to exclude this effect, it is important to investigate the effect of polarisation duration on the signal when the shaking effect is at its minimum and therefore the signal stabilises. This can be done either by conducting an experiment without shaking the sample or by allowing sufficient delay after the shaking process. This indicates that the polarisation transfer and therefore the hyperpolarised signal amplitude is also dependent on the amount of dissolved parahydrogen in the solution. This fact opens the window to the need to develop methods that continuously produce large amount of parahydrogen and which remain dissolved as long as possible. We conclude from these results that it is possible to increase the level of polarisation by using polarisation duration of 60s which persists for a period longer that produced by the typical 6 s. The dependence on polarising duration could be due to the rates at which parahydrogen, catalyst and substrate interact. To examine this in detail it

would be necessary to repeat these experiments at different temperatures and with differing catalyst and substrate concentrations. This was not carried out for this thesis.

### The effect of using small flip angles on the signal decay

Theory predicts that with SABRE or any other hyperpolarisation method, that if a 90 degree flip angle is used, then all the hyperpolarised signal would be transferred to the transverse axis and used up such that at the end of the FID, the remaining signal in the longitudinal axis would be simply that due to the normal thermal, Boltzmann, equilibrium.

In this section it is investigated what happens when we readout the hyperpolarised signal using different flip angles. We assume that using large flip angles such as a 90 degree pulse will consume all of the magnetisation so that no more magnetisation would be left in the longitudinal axis for any consequent 90 degree excitation pulses. Thus if the transmit pulse is repeated it is predicted that this would leads to a fast decay of the measured signal. However, when smaller flip angles are used to tip the magnetisation into the transverse axis, only a small amount of the total signal would be consumed and a very high fraction of the magnetisation on the longitudinal axis would remain in store to be used with subsequent excitation pulses. This stored magnetisation could allow for the use of repeated sequences such as those that are needed to create an image or for calculating kinetics of reactions or for diffusion measurements.

Here, the measured signal was studied as a function of repeated runs and flip angles are shown in Figure 4.9. Using the same sample used in Section 4.3.2 and a $B_p$ of 6.5 mT. It is clear that the initial signal is greater (about 3.6) when the 90 degree flip angle is used than those obtained from when a 45 and 27 degree flip angle is used. However, when a 90 degree flip angle was used it s was followed by a fast decay of the signal when the excitation was repeated but it did not disappear after the first pulse. This is presumably because that the 90 degree pulse is not exact and nor does it affect all regions of the sample equally. On the other hand, although the initial signal from using a 45 degree flip angle was smaller than that when the 90 degree flip angle was used (about

3.31) it shows a much slower decay which persists over longer periods at a higher level than those of the 90 degree excited signals. This demonstrates the lower consumption of the signal and the the concept of an exploitable reservoir of the signal. Signals obtained from the 27 degree flip angles last for an even longer time than those of the 45 degree flip angle measurements. Therefore, using smaller flip angles provides the possibility of using SABRE in the earth's magnetic field for in vivo studies where the required time for sample transportation is long.

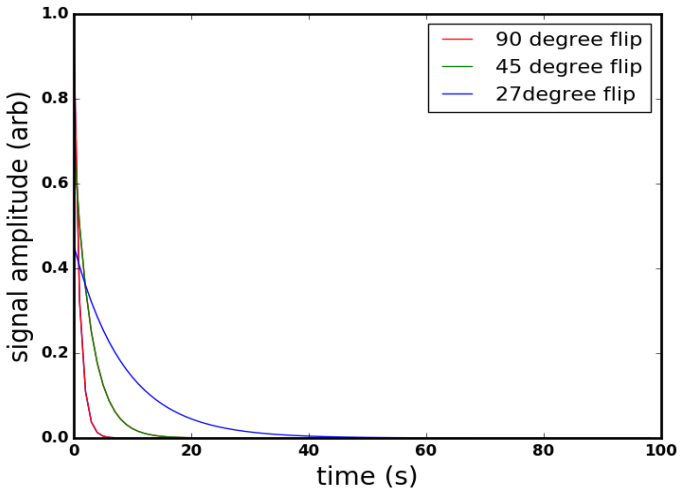


Figure 4.8: The calculated exponential decay of the signal in a function of time. It is clear that a larger amount of signal is consumed when using larger flip angles such as 90° and the signal decays faster than those derived from smaller flip angles 45° which are preserved for longer periods at greater levels.

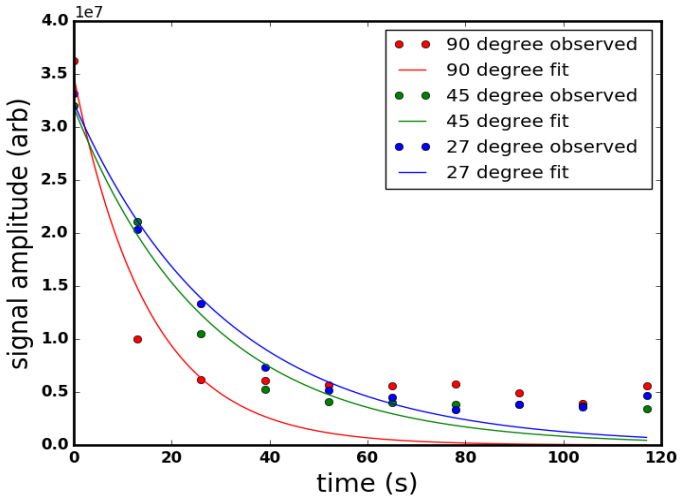


Figure 4.9: The measured signal decays of the hyperpolarised sample in earth magnetic field using different flip angles with exponential decay fitting. There is close agreement between the calculated results in (figure 4.8) and the measured data.

The free induction decay of the same hyperpolarised sample using different flip angles compared to that of 500 ml of water and plotted in Figure 4.10.

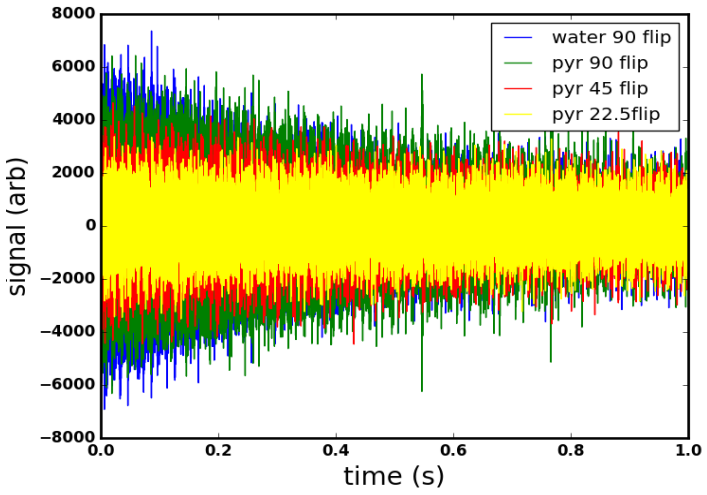


Figure 4.10: The measured FID decays of the pyrazine at flip angles of 90°, 45° and 22.5° compared to water

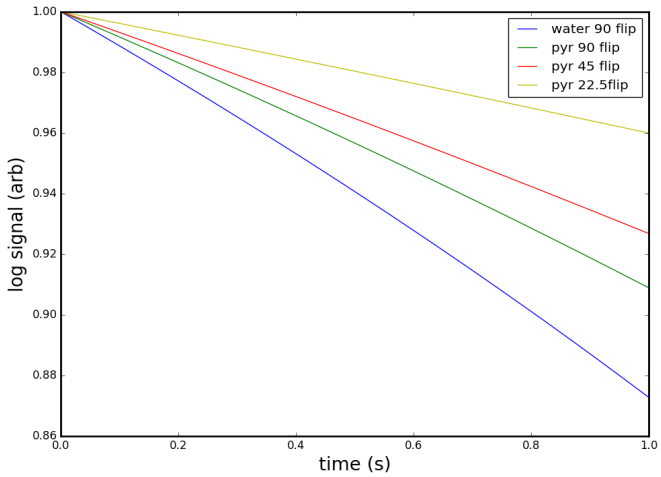


Figure 4.11: The log predicted decay of FIDs of pyrazine at flip angles of 90°, 45° and 22.5° compared to water.

The calculated slope observed in Figure 4.11 as a result of using (90° water , and pyrazine at flip angles of 90° , 45° and 22.5° ) excitation pulses were - 98633 , -73184 , - 52953 and - 26717 respectively. This indicates that the FID observed from the 90° excitation pulse of water sample decays faster than those of other excitation pulses with pyrazine followed by 90° pyrazine , 45° pyrazine and 22.5° pyrazine respectively.

### 4.3.3 Parahydrogen in solution following a dissolving shake

The amount of parahydrogen dissolved in the liquid sample following the initial dissolving shake would be expected to decrease significantly within a few seconds. This would be because any large bubbles would rise to the top of the sample and disperse into the headspace, and microbubbles would collapse and the enclosed gas would enter the sample and a new solution/headspace equilibrium of partial pressure would be established. Parahydrogen itself might also be converted into orthohydrogen and thus lost as far as the SABRE process is concerned. The rate at which this parahydrogen amount decreases can be measured. This is done by shaking the sample that includes parahydrogen in the headspace of the tube manually in the earth's magnetic field and then followed immediately by inserting it into the probe. The time between the

end of the dissolving shake and the beginning of the measurements was varied from 1 s to 18 s. The mean of 10 observations for each time point were taken. Figure 4.12 shows the relationship between the signal amplitude and the delay between shaking and measurements. This indicates that the observed signal is strongly related to the amount of parahydrogen available and dissolved in the liquid sample.

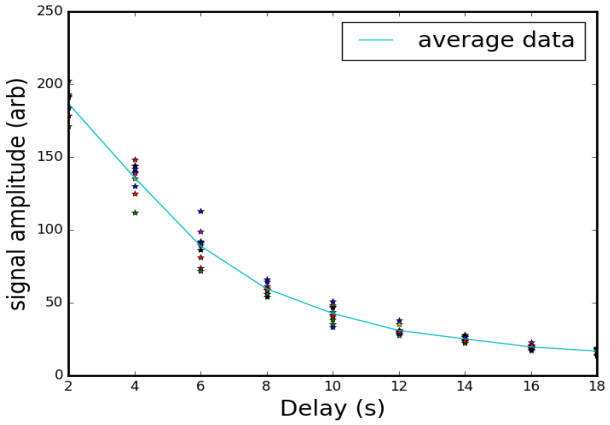


(a) signal amplitude

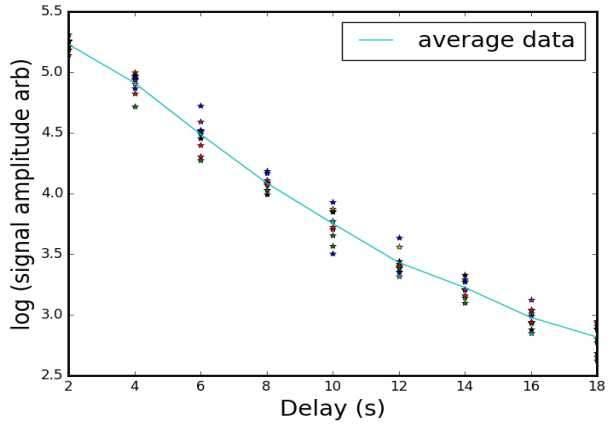


(b) log signal

Figure 4.12: Two plots showing the rate of parahydrogen loss following the shaking of the sample as a function of delay.

The amount of available parahydrogen and hence the sample signal decreases significantly with time. To evaluate the diffusion rate the scan time of each pulse sequence must be short enough to allow several repetitions while parahydrogen is still dissolved in the sample. That is to say, applying the polarisation pulse for 6 s or less has to be performed (rather than the optimal 60 s) to

measure this rate. Figure 4.13 shows that a sequence using 60 s polarisation duration is impractical.

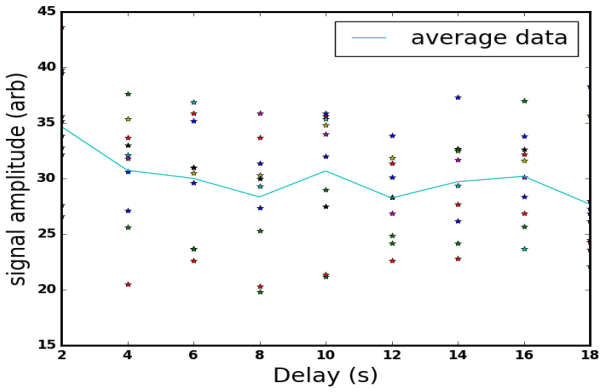


(a) signal amplitude

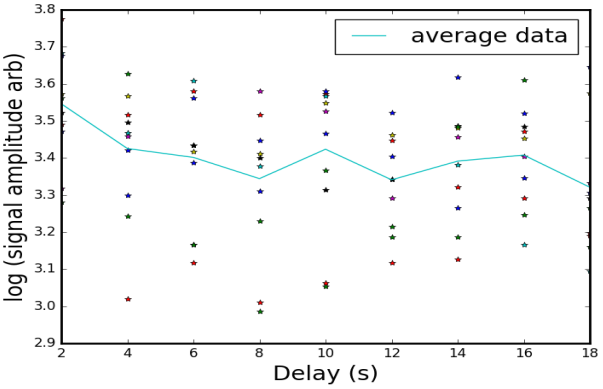


(b) log signal amplitude

Figure 4.13: Two plots showing that applying the polarisation field for 60 s is not feasible in order to study the effect of polarisation loss immediately after shaking the sample because the process of loss occurs in a time much shorter than the optimal polarisation duration.

Figure 4.13 shows that using a polarisation duration of 60 seconds is not feasible to study the the rate of polarisation decline if accomplished immediatly after shaking the sample. This is because large part of signal decay happens in the first 18 seconds as shown in Figure 4.12. Therefore, we excluded the use of polarisation duration of 60 seconds.

### 4.3.4 $^{1}$H NMR signal enhancement

The values of the best polarising fields and 90° flip angles that were found in previous sections were used in a range of single shake and drop experiments

to investigate the maximum 1H NMR signal enhancements using SABRE hyperpolarisation in the earth's magnetic field. Signal enhancement per mole of each hyperpolarised molecule were compared to that of water in thermal equilibrium. In 500 ml of water in the earth's magnetic field, there would be only 1 nucleus out of 2.7 billion nuclei contributing to the total $^{1}$H NMR signal (from theory). But by calculating the signal per mole, rather than the signal per net contributing nucleus, we can easily compare signal enhancements across substrates.

The mole amount of protons in the water sample can be estimated to be 500 x 2/18.015. This is because there was 500 grammes of water, the molecular weight of water is 18.015 and there are two Hydrogen for molecule. This the number of moles of Hydrogen in the water sample can estimated to be 55.51. Similar calculations can be performed for the other substrates.

The FID and signal amplitude of each of the three substrates (Pyrazine, nicotinamide and aminothiazole) have been compared to those of a water signal Figure 4.14. The flip angle and the polarising duration were set for each substrate according to the optimal values based on previous sections.

The hyperpolarised pyrazine shows a signal enhancement of about 60,700 fold per mole compared to that observed from the water sample. That is equivalent to saying that one nucleus of SABRE polarised sample out of 45,000 contributes to the total signal and this is equivalent to performing a normal, unhyperpolarised, NMR experiment not in the earth's field but in one 60,700 times higher, that is about 2.25 Tesla. Hyperpolarised Nicotinamide and Aminothiazole shows signal enhancements of 22,900 and 14,000 receptively compared to the signal per mole in water in the earth's magnetic field.

Table 4.1 compares signal enhancements per mole of water in thermal equilibrium and in hyperpolarised samples.

| Molecule | contribution to signal (1 particle per) | signal enhancement |
|---|---|---|
| Water | 2.7 billion | 1 |
| pyrazine | 45,181 | 60,759 |
| Nicotinamide | 119,737 | 22,926 |
| Aminothiazole | 195,789 | 14,021 |

Table 4.1: Table comparing signal enhancements (per mole) of hyperpolarised samples compared to water at thermal equilibrium.

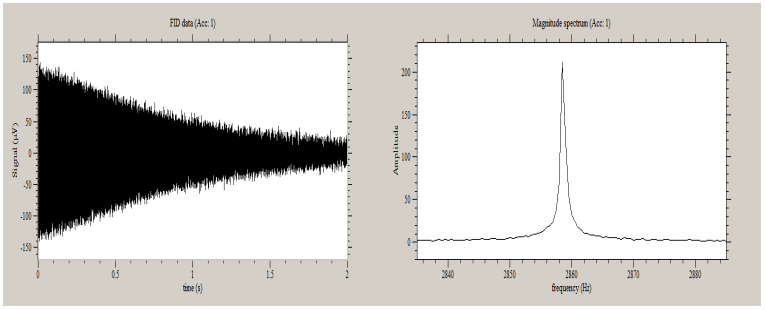


(a) water at thermal equilibrium

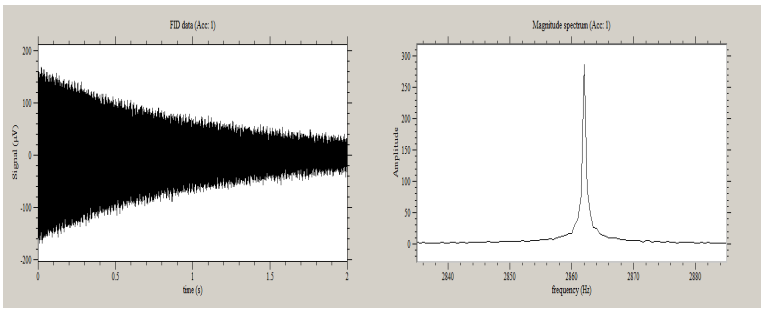


(b) hyperpolarised pyrazine

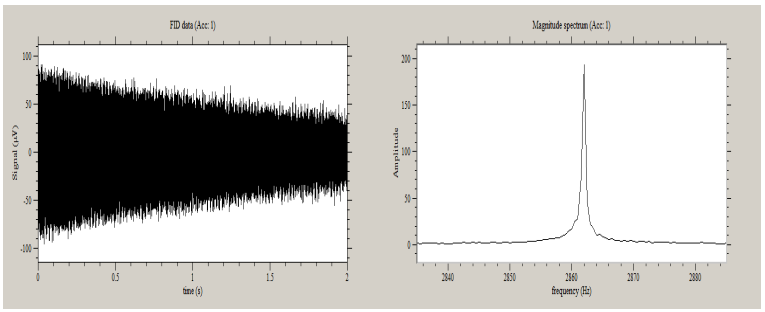


(c) hyperpolarised nicotinamide

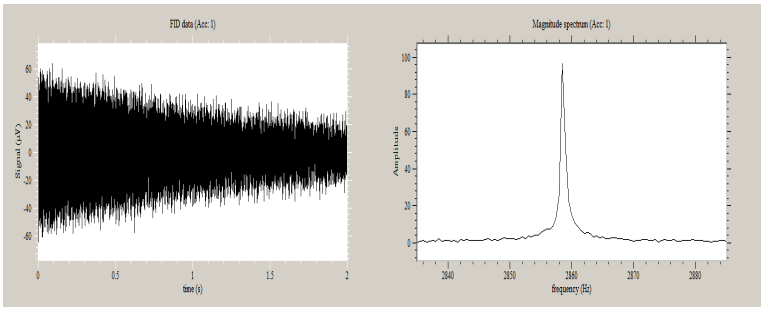


(d) hyperpolarised aminothiazole

Figure 4.14: Four plots comparing 1H NMR signal enhancements of hyperpolarised (pyrazine, nicotinamde and aminothiazole) substrates to water at thermal equilibrium.

### 4.3.5 SABRE signal decay

A single shake, for 10 s, and drop experiment was conducted using SABRE with a solution that contained 25 mg pyrazine, 10 mg catalyst dissolved in 3 ml $d_4$-methanol. A pulse sequence was used that consisted of a 6 mT prepolarisation pulse which was applied for 4 s then excited by a 90° excitation pulse and a 200 ms measurement period to detect the signal. This was repeated 1666 times separated by 12 s TR and total scan time of 18000 s. Data collection started about 20 s after the end of shaking the sample. The mean of the background signal was measured (0.72 on an arbitrary scale) to distinguish it from SABRE signal Figure 4.15.

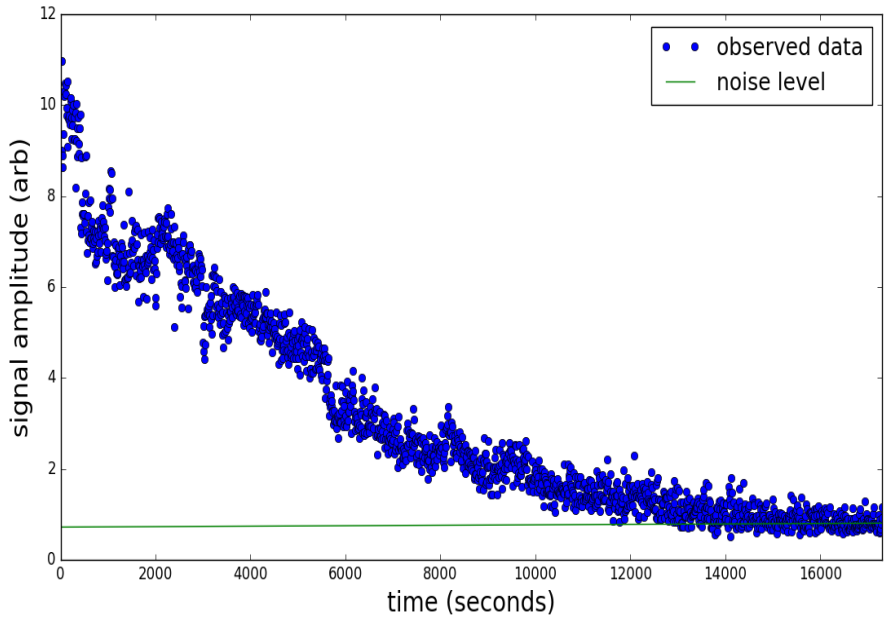


Figure 4.15: Signal decay from hyperpolarised pyrazine.

The result shows a slow decay of the signal that remained for 16528 seconds (4 hours 35 min) until it reached the level of the background signal. The long duration of the signal cannot be explained as being due to the persistence of a signal from an individual polarisation but may be due to the continued diffusion of pressurised parahydrogen from the top of tube into the liquid sample. This indicates the possibility of using SABRE hyperpolarisation in low magnetic field for very long experiments without the

need to re-shake the sample or to refill the headspace with fresh parahydrogen. However, a sufficient amount of parahydrogen at suitable pressure (e.g. 3 bar) is important to keep the diffusion process lasting as long as possible. If for example, the pressure dropped significantly or parahydrogen was released it is assumed that the signal will drop sharply and immediately. The next section will describe the effect of opening the tube at certain time to allow parahydrogen to flow out of the test tube.

### 4.3.6 The effect of releasing parahydrogen from the test tube

A SABRE signal results from the magnetisation transfer to a ligand that has been driven from the parahydrogen to the target molecule. It was shown that increasing the concentration of the parahydrogen in the liquid solution - by increasing the pressure of parahydrogen- increases the amplitude of the detectable hyperpolarisation [Mewis et al., 2014]. Hence, we hypothesised that if we open the tube and allow the pressurised parahydrogen to be released from the test tube so that the pressure decreased dramatically to about atmospheric pressure, the signal should decay significantly.

A single shake and drop experiment was done where all parameters remained fixed as those in Section 4.3.5. However, the pressurised parahydrogen at the headspace of the test tube was released after 2000 s. Following the time when the tube was opened there was a marked decrease in the SABRE signal. It was possible to estimate how the amount of polarisation was affected at a given time, the signal before and after this event were compared. The percentage the signal decreased was calculated.

When the tube was opened the signal dropped significantly from the level of 14 to 4 and continued with a slow decay until it has vanished completely after about 14000 seconds instead of about 16528 when the tube was kept closed (in the previous experiment). This indicates that when tube opened the pressure and therefore the concentration of parahydrogen at the headspace decreases and thus, the rate of polarisation transfer process reduced, supporting the hypothesis that the long duration of polarisation found in the previous section is due to continued diffusion into the solution.

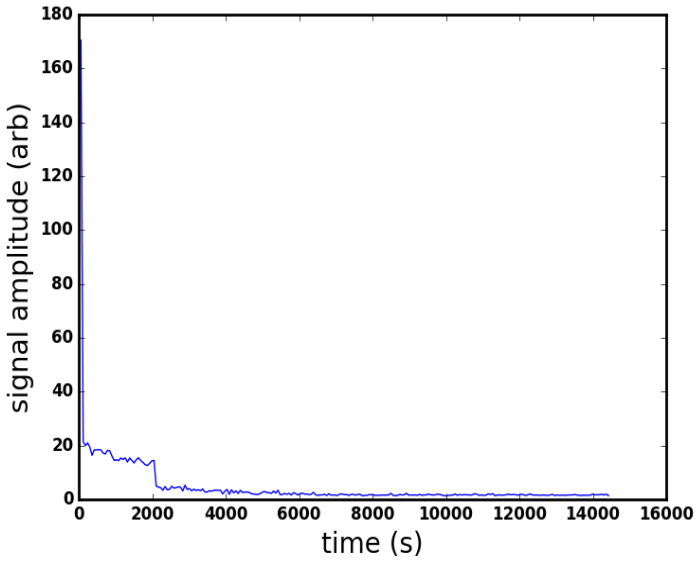


Figure 4.16: Signal decay of hyperpolarised pyrazine when the tube was opened after 2000 s.

The region where the signal dropped as shown in Figure4.17 showing about 3.5 fold decrease in the level of the signal amplitude.

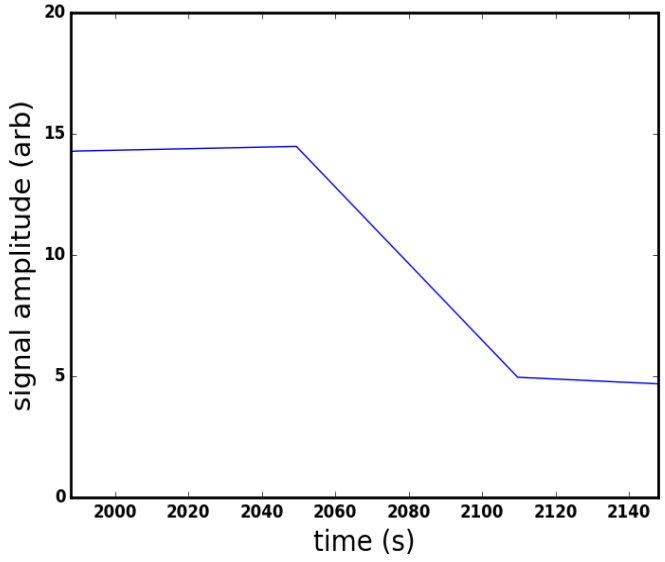


Figure 4.17: Plot shows zoomed area where signal drops sharply due to releasing pressurised parahydrogen from the headspace of the test tube after 2000 s.

To summarise, releasing the pressurised parahydrogen from the tube

significantly influences the diffusion rate between the headspace and the liquid sample and therefore, the SABRE amplitude. This indicates that the consistency of SABRE signal is strongly related to parahydrogen pressure.

### 4.3.7 The effect of multiple shakes of the sample

Typically in SABRE, the maximum signal enhancement is observed immediately following the shake and drop process and decays in as a fairly rapid function of time. In our measurements, signal losses of about 90 percent - from about 170 to 10 - of its amplitude occurs in the first 20 seconds and continues with a slower decay rate. Therefore, we assume that if we shake the sample later we will increase the signal enhancement but with less amount than the previous shake. This is because some amount of parahydrogen was consumed.

A several shakes experiment with the same parameters as the above was conducted but with several shakes Figure 4.18 using increment of 10 seconds instead of single shake of the sample. Maximum signals following each shake were observed to investigate the decay rate of parahydrogen availability with time.

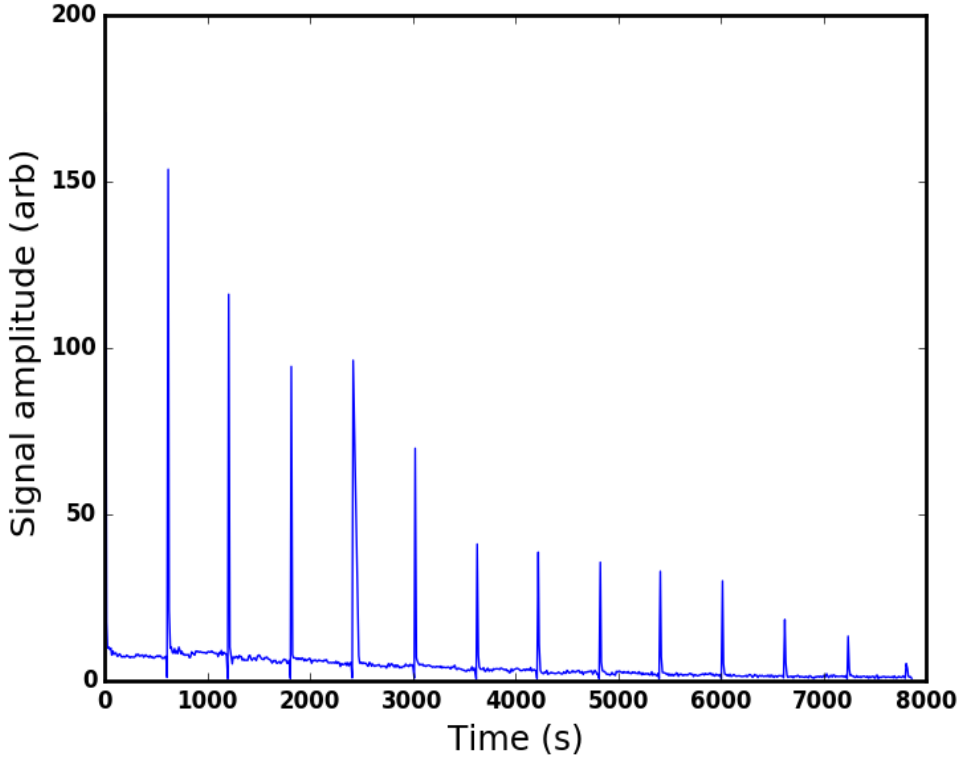


Figure 4.18: Signal decay from hyperpolarised pyrazine .

The results in Figure 4.18 show a significant signal enhancement following every shake but with values lower than the previous shake. When the maximum signals after the shakes are compared, there was an exponential decay with time. The decay rate is such that it decrease by half in about 2720 seconds.

When the same experiment was performed but without shaking the sample Figure 4.19 using the same y-scale factor as in Figure 4.18, an initial signal enhancement of 37,350 fold was obtained and it decayed gradually remaining at the level of 6,047 fold enhancement after 6000 seconds when compared to the water signal.

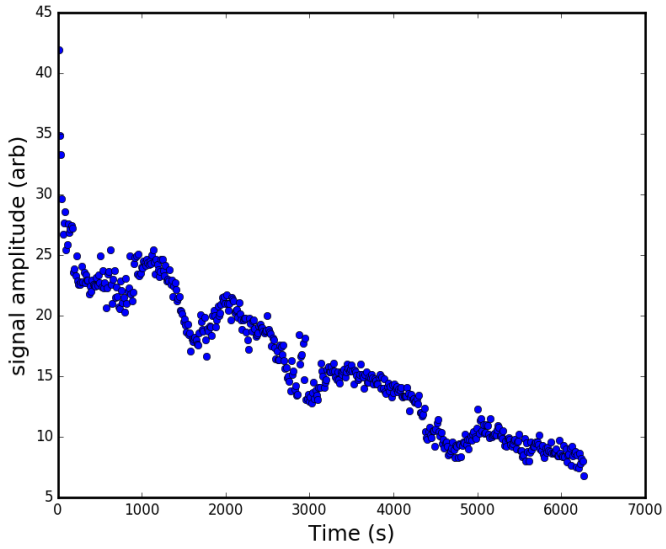


Figure 4.19: Signal decay from hyperpolarised pyrazine without shaking the sample.

### 4.3.8 The effect of heart tissue of a rat on the signal decay

When heart tissue of a rat was cut in to small pieces and immersed in the liquid sample, parahydrogen added, sample shaken and dropped in the spectrometer both initial signals of the two samples (without and with heart tissue) were observed at high levels of 197,425 and 182,311 fold respectively Figure 4.20. This was followed by a sharp drop and then the signals decayed gradually with time. The integral of an exponential decay of the sample with heart tissue Figure 4.20a behaved exactly as that of the sample without heart tissue but at slightly lower level. This would seem to indicate that the heart tissue does not affect the decay of the signal and that parahydrogen or substrate is interacting with the tissue.

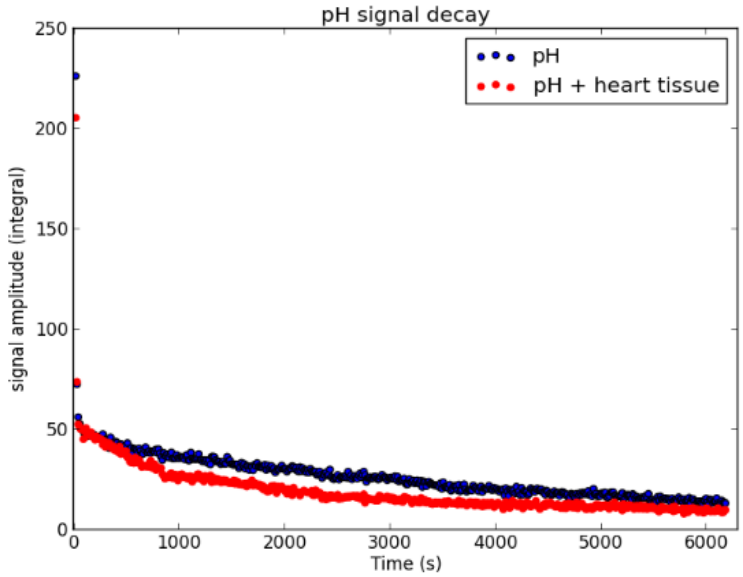


(a) with shaking the sample

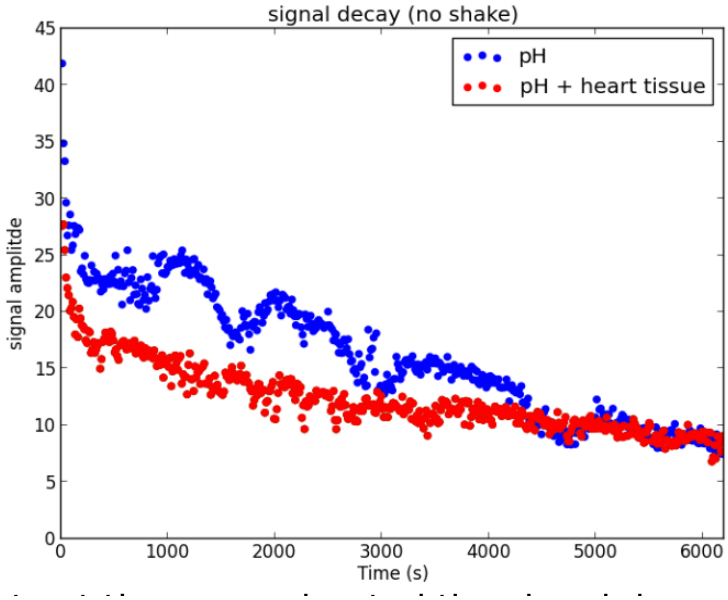


(b) without shaking

Figure 4.20: Signal decay of heart tissue immersed in liquid hyperpolarisation sample. (a) with shaking the sample (b) without shaking.

### 4.3.9 Two dimensional imaging

The liquid sample was prepared by dissolving 10 mg of [Ir(IMes)(COD)Cl] catalyst and 25 mg of pyrazine in 3 ml $d_4$−methanol using 10 mm tubes fitted with a Young's tap. Then, the tube was filled with parahydrogen at 3 bar pressure and shook for 10 seconds and dropped at the center of the EFNMR

probe.

A two dimensional vertical (zx) spin-echo image of 3.75 mm resolution was conducted using different repetition times and the other parameters remained the same as in previous optimisation experiments in this chapter. Data was collected and the 2D image using a 12 s TR and 60 s TR were reconstructed Figure 4.21. In this experiment a 90° flip angle was used for the excitation pulse and 180° for refocusing. other parameters were set as 32 x 32 matrix, spatial resolution of 3.75 (120 mm/32), polarisation field of 6 mT applied for 2 s, echo time 200 ms, 2893.5 Hz frequency and 32 Hz bandwidth. The total scan time was 25 minutes for 12 s TR and 128 minutes for 60 s TR.

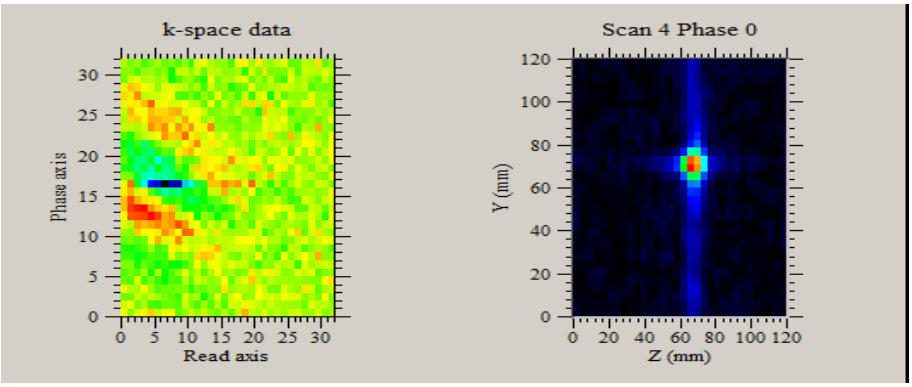


(a) TR = 12 S

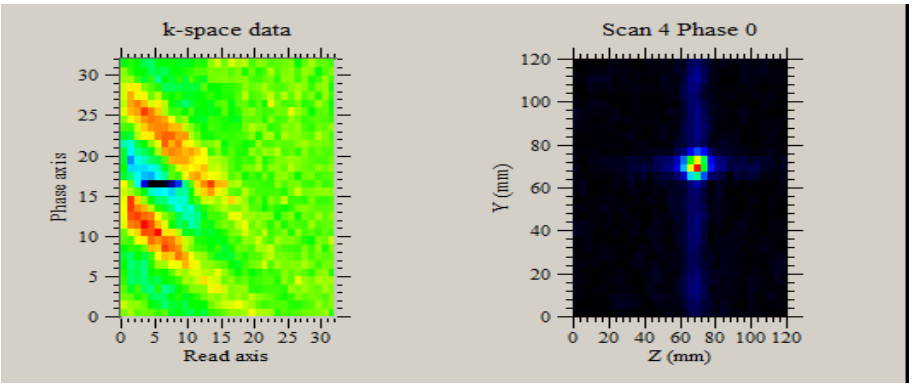


(b) TR = 60 S

Figure 4.21: Two dimensional imaging of SABRE in low magnetic field.

The result shows a 1 mm resolution imaging in both experiments indicating the possibility of collecting the small signal remain for a long time necessary for imaging.

## 4.4 Conclusions

Results from this chapter shown the relationship between the signal intensities and the magnitude of the RF pulse of different molecules. Data have been characterised for three molecules (Pyrazine, nicotinamide and aminothiazole) and compared to that observed from water sample. The 90° and the 180° were determined and compared for all samples. In addition, the best polarising field that would produce the maximum polarising transfer in SABRE have been observed for the used molecules. These values have been used to investigate other properties of SABRE in the earth's magnetic field such as

the decay time, the ability to use the hyperpolarised signal several times, the effect of parahydrogen pressure in the tube on the signal enhancement, the effect of shaking the sample several times on the signal amplitude, the effect of immersing heart tissue of a rat in the liquid sample on the signal decay and finally, the possibility of achieving a 2D imaging by using the optimal parameters.

# Chapter 5

# Automated pulse sequences in low field and SABRE

## 5.1 Introduction

In this chapter, EFNMR signal is not only enhanced by optimising the SABRE hyperpolarisation methods but also by improving the hardware and the software of a purpose built measurement system (and still using the coils of the terranova to excite and detect the signal) employed to produce a versatile earth's field spectrometer. This was done by developing a flexible Data AcQuisition system (DAQ) based on a DAC capable of performing complex NMR investigations for research purposes, designed by the operator, such as those requiring special pulse sequences that contain a range of digital triggering capabilities and multiple composite excitation pulses.

Many low field NMR spectrometers available today, including the Magritek Terranova system used in chapters 3 and 4 can only perform simple, conventional, NMR measurements such as SE and GE sequences. Moreover, the ability to modify those pulse sequences is often very limited. For example, sometimes it is hard to trigger any pulse in response to other events in the pulse sequence or even changing the number or the envelope shape of the transmit pulses. This fact may hinder the effort to develop new methods for NMR signal investigations in the earth's magnetic field. The concept of this

purpose built system resembles that made by [Asfour, 2011], except that this study relies only on the earth's magnetic field (50 $\mu$T) instead of using the pair of Helmholtz coils in their study to produce a higher magnetic field of 4.5 mT [Asfour, 2011]. The device here could easily be modified to also work at other magnetic field values.

In addition, instead of being limited to a hard pulse it is possible to use this new system to generate trains of sine-pulses or any other pulse shapes. In particular it is possible to create long sequences of, differing, arbitrary shapes (composite pulses). These are, in theory, useful when one wished to convert singlet states into observable magnetisation, of on the other hand to store magnetisation as a singlet and thus create a long-lived reservoir of magnetisation. It is also easy to shape the excitation pulse or pulses. All of this can be done with commands programmed in a high level language (Python) to create different pulse envelopes based on specific algorithms. In this system, sensitive electronics are also exploited to manage the excite-measurement pathway to and from the transmit-receive coil. The electronics are designed so that they can operate safely by employing diodes to allow the appropriate current to flow in one direction and prevent noise currents from travelling in the opposite direction which may lead damage to the electronics or incorrect measurements. This is subtly different from the methods used at the very high RF frequencies used in standard NMR and MRI machines.

The aim of this chapter was to develop a flexible, cheap, easy to make, purpose-built DAQ system capable of performing SABRE measurements in the earth's magnetic field. This system is made of group of items that - when working together - can separate the transmit and receive signals. These electronics are also sensitive enough to isolate the NMR signal from the background noise as far as possible Figure 5.1. This was achieved by employing two Data Acquisition (DAQ) boards that work interchangeably and are completely controlled by a software programming environment(Python) based around the DAC and ADC processes. Prior to any experiment, the shapes and timing of all components of the pulse sequence can easily be tailored digitally by the operator depending on the purpose of the experiment.

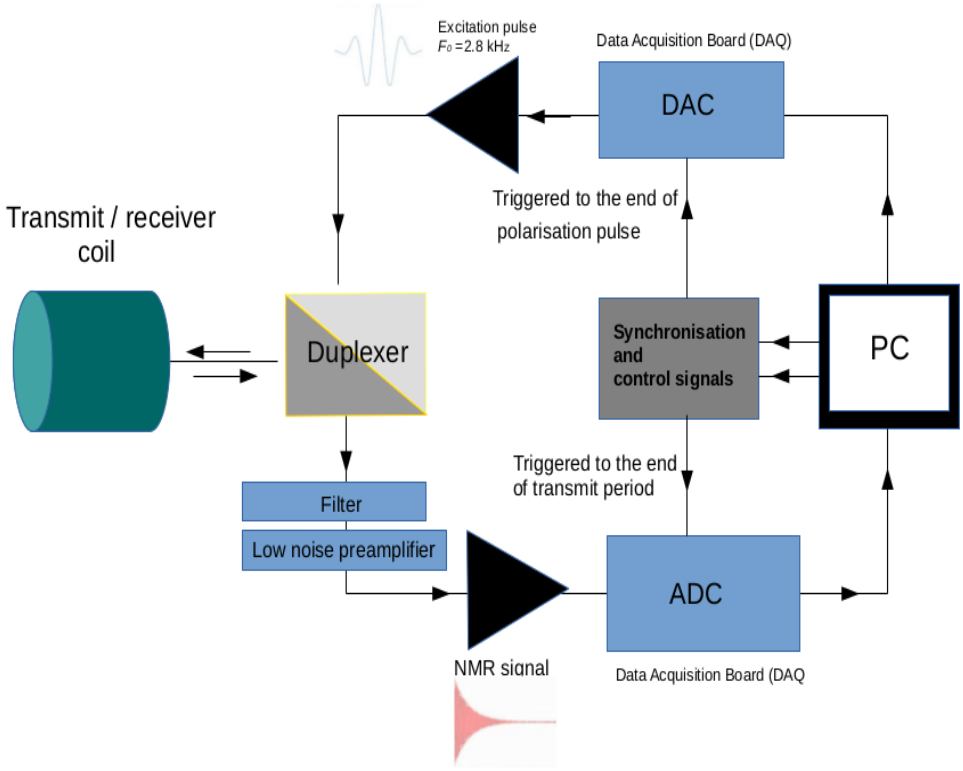


Figure 5.1: Purpose-built earth's field NMR transmite recieve system based on commercially available DAQ boards.

This purpose-built system is not only carrying out the same function as conventional earth's field NMR devices but it is also capable of providing a wide range of more flexible (and still sensitive) imaging options.

This chapter consists of three main sections: Section one will describe the main architecture and hardware of the NMR spectrometer which is based on the generation of transmit pulses and receiving the resultant NMR signal using commercially available DAQ boards. Section two will discuss the control software, signal detection and signal processing. Section three will show how that system can be used to optimise an EFNMR signal using the automated system both for water at thermal equilibrium and SABRE hyperpolarised samples.

## 5.2 Architecture and hardware

### 5.2.1 Agilent U2353A

This section describes the features and functions of the Agilent U2353A USB DAQ device used in our study (U2300A Series Multifunction USB Data Acquisition board by Agilent). This device allows an analogue input operation mode, an analogue output operation mode, digital I/O as well as input/output triggering of both analogue input and output.

Digital to Analogue conversion (DAC) is the process where the digital data created by the user by programming is converted to an analogue signal. In this thesis this process is used to create transmit pulses. The process of Analogue to Digital Conversion (ADC) converts analogue voltage signals to digital data, which then allows the computer to easily process and save the detected, receive, signals.

By allowing full control of the definition of the transmit pulse in the digital domain, the user can manipulate all aspects of the transmit sequence and even have multiple, switchable, transmit channels or even simultaneous excitation of multiple, parallel transmit coils.

Typically, transmit sequences are triggered in response to particular events, Similarly, measurement signals can be acquired following inout from trigger sources. When the condition of a trigger is met, the ADC acquisition automatically starts and the acquired data buffered in a FIFO (First In First Out) buffer. The analogue input and outputs have to have voltages between $\pm -10$ V to $\pm 10$ V. This implies that for measurement purposes the signal from receive coils has to be amplified and that for transmit pulses, the voltage has to be converted to a suitable current to create a magnetic field from the transmit coil. The following flow chart Figure 5.2 illustrates the functional block diagram of the Agilent U2353.

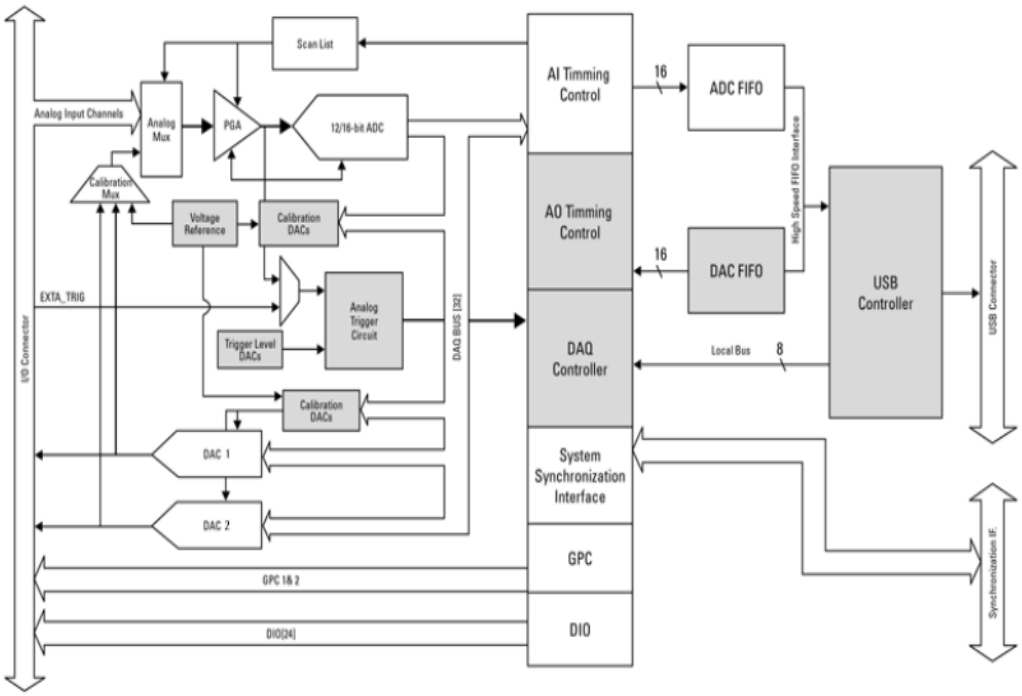


Figure 5.2: Functional block diagram of Agilent U2353. Image from (docs-europe.electrocomponents.com/webdocs/0d87/0900766b80d871b4.pdf)

The Agilent U2353A (U2300A Series Multifunction USB Data Acquisition board by Agilent, 2013) has to be connected to a computer using a USB connection. It can be powered through the USB cable or can use an Agilent power supply in a rack that can house multiple Agilent USB devices. When the U2353A is switched on, the system loads the calibration constants from an on-board EEPROM (Electrically Erasable Programmable Read Only Memory) to insure that both the DACs and PGA (Programmable Gain and AC/DC coupling) are working accurately and are calibrated. Python commands were used to create the correct sequence of data that is sent over the USB to fully configure the U2353A. These are used to set the input configuration in the scan list (channels used), sample rates, trigger source, and the trigger mode. The DAQ can be preconfigured with various scan data acquisition parameters and timings, and be programmed to wait until the trigger condition is matched, then all analogue outout and input automatically takes places. The information then transfers from or to the memory of the system employing appropriate data transfer modes over the USB.

### Sampling rate and sampling points

The U2353A is capable of acquiring data at sample rates upto 500 K Samples per second on upto 16 input channels. Since the U2353A DAQ device comes with a multiplexing analogue input, the maximum sampling rate when using multiple channels is based on ADC's maximum sampling rate and the entry number in the scan list. This flexibility of having a channel scan list means that it is possible to have very different sample rates for different channels. But the maximum rate, across the scan list is limited by the maximum sample rate for the system. Therefore, the user needs to define suitable sampling rates for each input channel, and specify the number of acquisition points for that channel. The software developed for this board as part of this study made this easily possible for arbitrary analogue inout schemes (Agilent Technologies, Inc, 2013, USA).

### Analogue output operation

One of the two available D/A channels in the U2353A DAQ device was been used to produce a single transmit signal. Multiple boards were present in the system allowing the possibility of parallel transmit, Each channel is able to generate a maximum current of 5 mA. This is not sufficient to drive an excite coil so a booster amplifier was used on the output of each channel. The analogue output channel was used to drive the transmit coil.

### Digital I/O

There are four digital input/output channels (CH 501, CH 502, CH 503 and CH 504) Figure 5.10 on the U2353A. Each allows 24- bits of General- Purpose digital I/O (GPIO) which are programmable as either input or output. When the system starts operating or after a reset, these I/O pins are reset to the input configuration. This was taken into account in the driving software for the system so that it was not possible to have inappropriate connections of the transmit/receive coil or measurement electronics to high voltages or currents.

In addition, the U2353A has a USB programmable, modular, switch matrix

block which allows arbitrary connection pathways through the matrix block. Unfortunately, this matrix block does allow precise timing of the switching of the input/output connections, so it was not used in this thesis for the final work. A different method of switching signal paths was developed using reed relays.

#### Triggers

Two types of triggers have been used in our pulse sequences. First, a **Delay trigger**, this is used to delay the data acquisition of the NMR signal for certain amounts of time following a specified trigger event. The delay value can be varied easily by the user. Second, a **Digital trigger**, this allows the specification of either a positive or a negative trigger. Here, the system detects the rising or falling edge of the signal Figure 5.3.

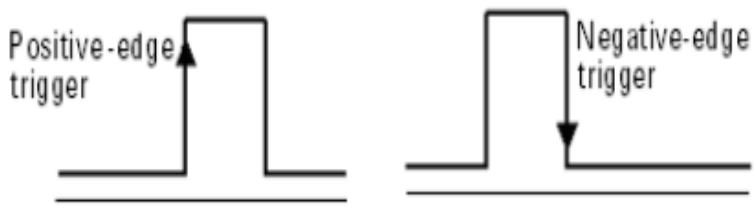


Figure 5.3: Positive and negative edges of trigger signals used for triggering the pulse sequence following the polarisation field.

### 5.2.2 Transmitting the excitation pulse

Typically, the transmit/receiver coil was tuned to $^{1}$H nuclei and the system was shimmed before performing any measurements. Python commands were created that could be sent to the core Magritek system to output appropriate currents to allow the shimming of the system coils. Here, because we use the purpose-built DAQ system (instead of the Magritek core system) for signal production and detection, the excitation pulse is synthesised, digitally, at a low frequency of approximately (depending on the value of the earth's magnetic field for each experiment) 2.8 kHz using Python commands which can be easily modified by the operator when required. One of the data acquisition

boards was employed as the transmit pulse generator. The DAQ board has been chosen due to its powerful features as it is a powerful device that can provide a high sampling rate coverage of the analogue output with a maximum amount of 3 MSa/s for a single channel. This allows for a 3 Msa/s with 16 bit resolution for a single channel.

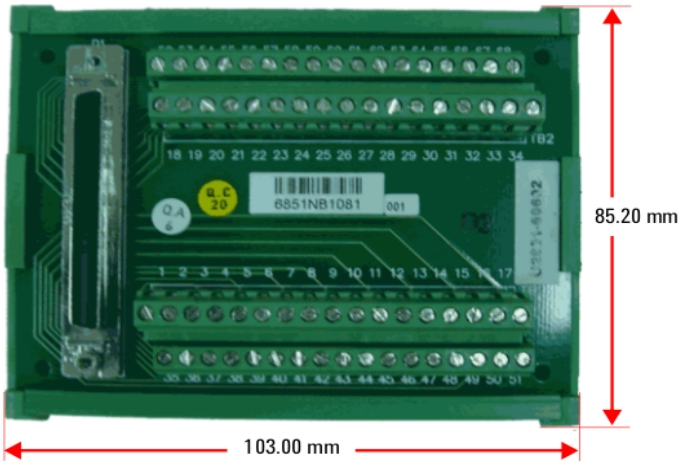


(a) Front view

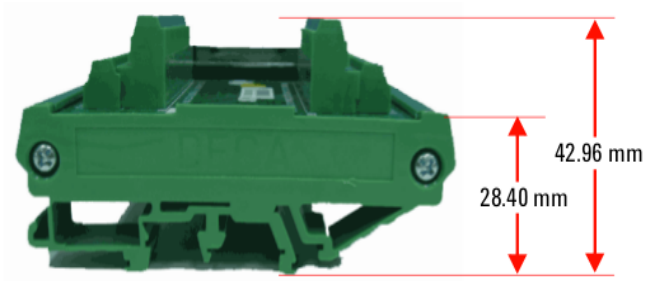


(b) Side view

Figure 5.4: The electronic schematic of a DAQ board (a) shows that pins arranged in the top and bottom are associated with different multifunction channels. The left part illustrates the Dsub connector which is used to offer a connection between the DAQ board and Agilent U2353 via a USB extension cable. The side view (b) shows the dimensions of the board. Image from (docs-europe.electrocomponents.com/webdocs/0d87/0900766b80d871b4.pdf).

The analogue transmit/receive pulses need to be adjusted before reaching the

NMR probe (for excitation) and before returning back to the computer (for processing) between the DAQ boards and the probe. This was done by using integrated operational amplifiers **op-amp** consisting of groups of electronics (e.g resistors, diodes and transistors) to provide suitable amplifier gain and bandwidth. The function of the amplifiers can easily modified manually by changing the values of each item. For example, if we need to reduce the output current a resistor with a greater value (e.g 10 kΩ) is placed manually instead of the lower value resistor (e.g 1 kΩ). The two operational amplifier circuits are fed by a low voltage (digimess Concept series) power supply with an appropriate voltage (5 V) Figure 5.5. The current of the circuit is such that battery operation for low noise is possible. One of these amplifiers is used to amplify the excitation pulse and the other is used to amplify the observed signal. This amplification achieved by the combination of these items that are arranged in a circuit to work together. This unit is important to allow voltage rapidly and stabilises it at appropriate value. Thus it is designed to have a wide bandwidth with no overshoot. The Bipolar single transistor (model BD243C) Figure 5.6 that is used has the advantage of low noise.

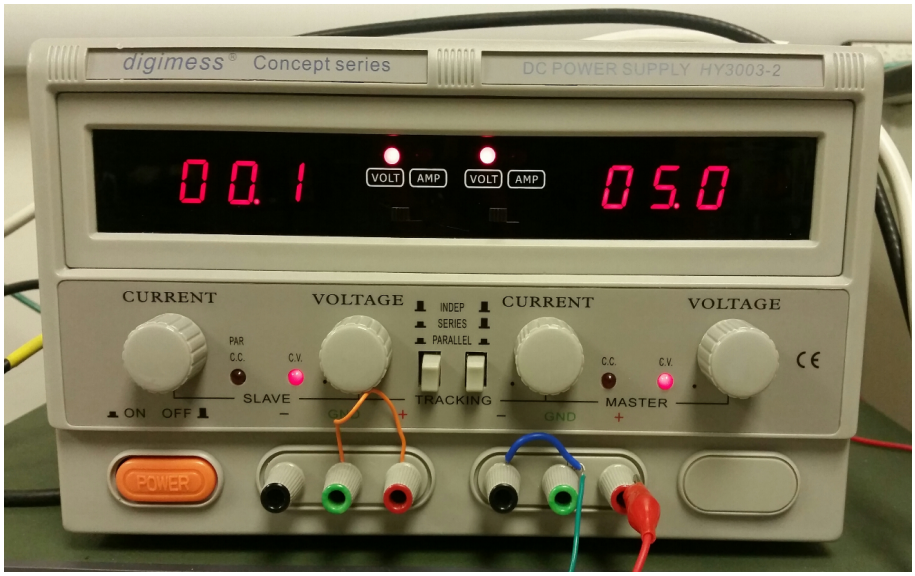


Figure 5.5: The power supply device used to supply the two amplifiers used in the purposed-built system.

NPN Figure 5.6 is one of two Bipolar Junction transistors (BJT). It is consist of P-doped semiconductor known as "The base" between two N-doped

layers. When a small current enters the base it is amplified to generate a collector and emitter current. When the two conditions are met the transistor becomes active. First, if there is a positive potential difference measured from the emitter to the base. Meaning that the base is high relative to the emitter. Second, similarly, if there is positive potential detected from the base to the collector. Therefore, it becomes in the on state, and charge flow between the collector and the emitter.

BJTs in this study was used as amplifiers and switches which usually can be found in wide range of electronics (e.g computers , televisions and audio amplifiers).

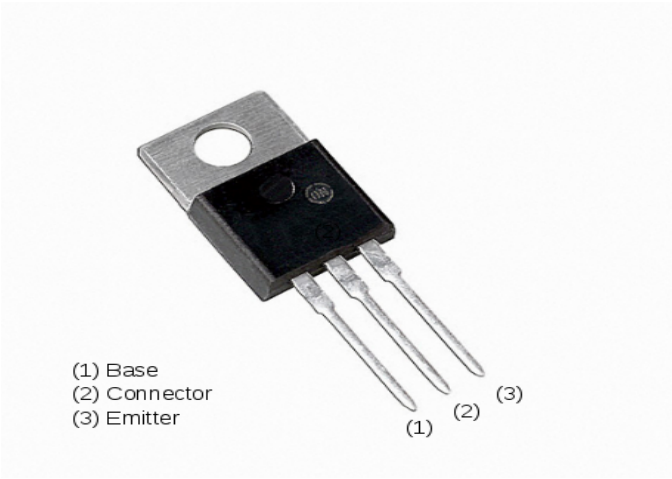


(a) Front view

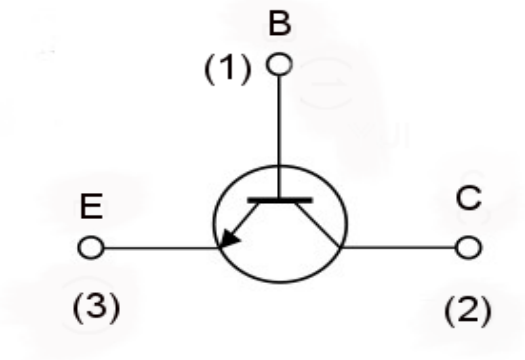


(b) Side view

Figure 5.6: The design of the NPN transistor.

Figure 5.7 demonstrates the electric circuit used for the transmit/ receive process. The reed relays (the orange box) are thin, flat blades that achieve multiple functions (as conductor, contacts, springs, and magnetic armatures). When a blanking current flows, the electromagnetic coil energised and the normally open contacts are pulled together and contact. The contacted area is usually covered with rhodium to reduce resistance during the contact mode. The other terminal of the electromagnetic coil is connected to a diode to allow this current to flow in only one direction and avoid any back currents. Because the electromagnetic coil is very sensitive to magnetic fields originating from the surrounding area, it is important to be shielded or kept at proper distance away from any magnetic or electric sources during the operation to avoid magnetic interactions. It is also important to keep it away from any other relays.

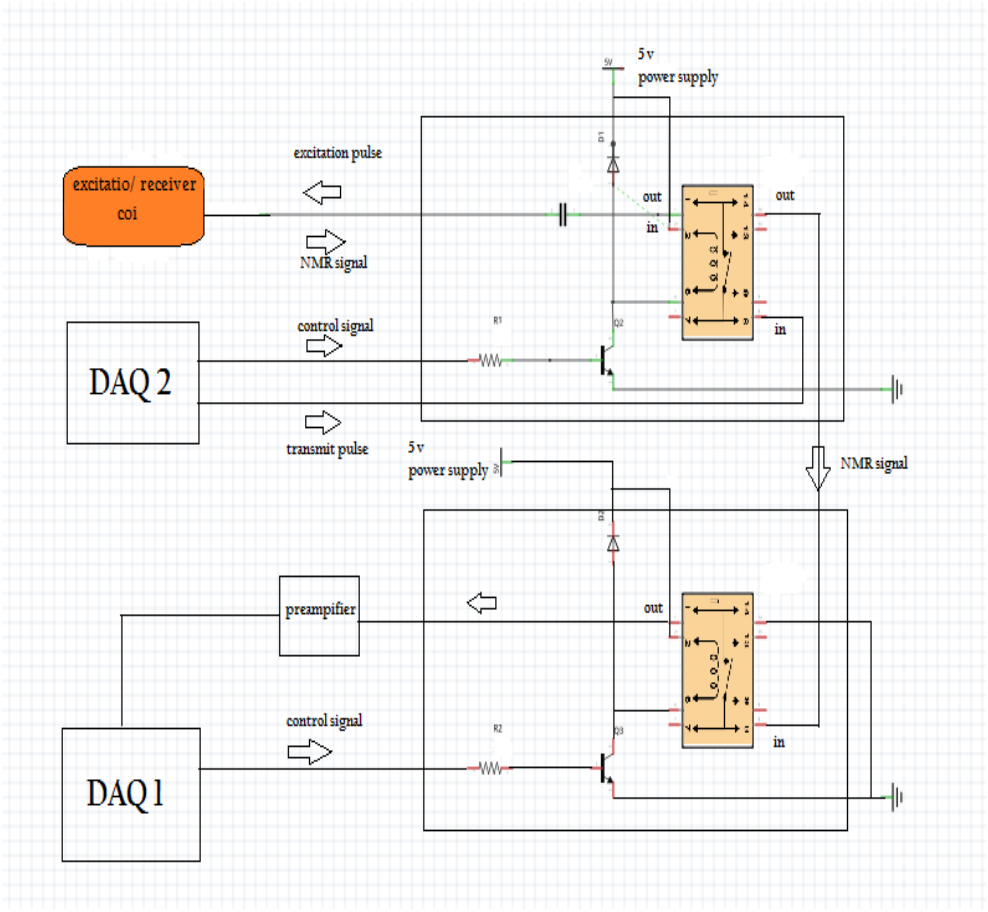


Figure 5.7: Electric amplifier circuit illustrates the path of transmit/received signal synchronised with control pulses.

The control signal which has synchronised with transmit period is triggered to the negative edge of the polarising pulse. This means that one channel of the DAQ board is used as a sensor connected to the polarising source to detect the voltage change related to the polarising pulse which rises from zero to about 5 volts when it starts (On) and continues for a period of time depending on the polarising duration defined earlier. Then the voltage drops sharply from 5 volts to zero as soon as the polarising period ended. When the voltage reaches the zero level the control signal triggered automatically and generated through a programmable DIO of channel 502.

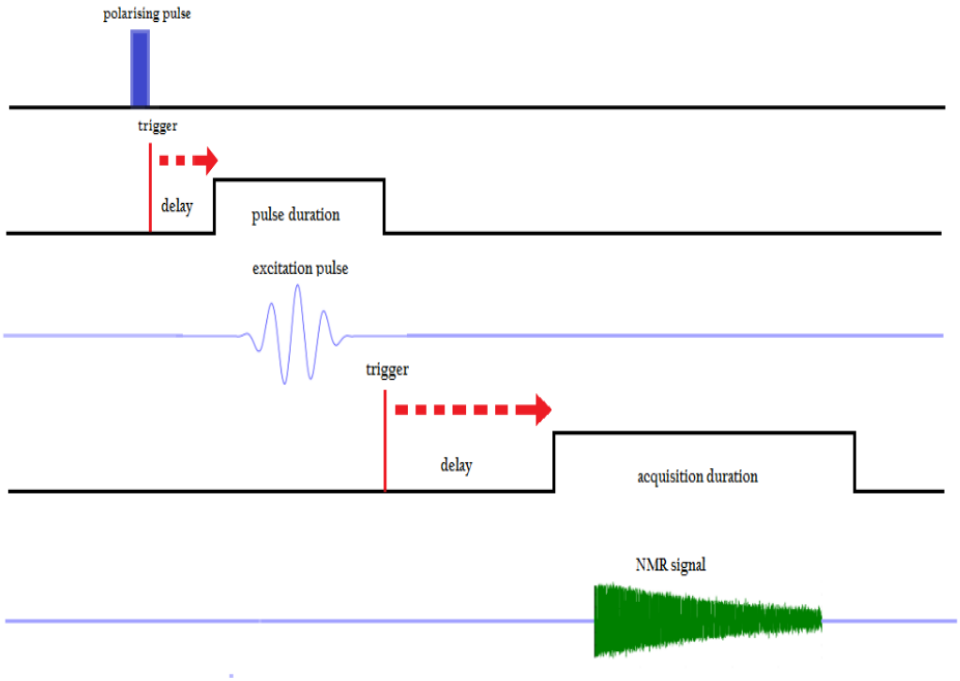


Figure 5.8: Components and timing of the pulse sequence.

A signal from a transistor was sent to a dual line reed relay (W171DIP). This reed relay has the advantage of fast performance and the ability to operate using a very little power from a control line.

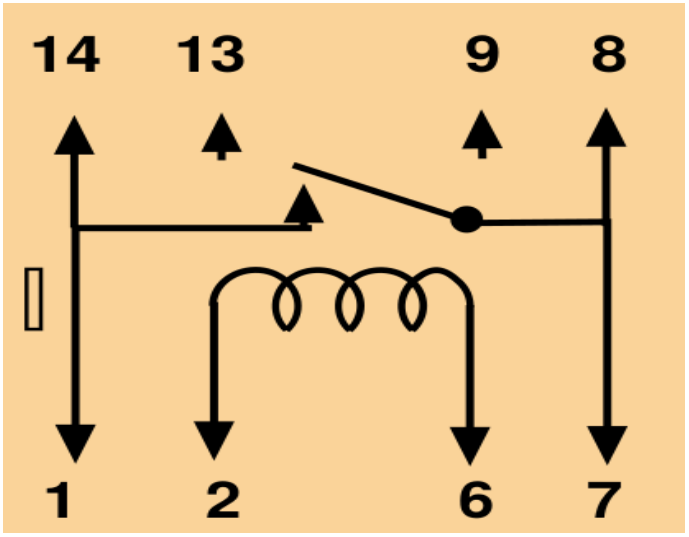


Figure 5.9: A schematic representation of (W171DIP) read relay.

The control signal associated with the transmit period then travels through this amplifier circuit via the 10 k ohm resistor then to the base terminal of the NPN transistor which is grounded through the Emitting terminal. The output signal is sent through the Connector terminal toward terminal number 6 of the reed relay Figure 5.9. This terminal delivers the input voltage to the electromagnetic coil inside the reed relay.

Therefore, terminal 1 and terminal 8 inside the reed relay become contacted for a period of time. The transmit signal is thus synchronised automatically with this period so when the switch is in the On state and gate is open, pin AO202 (Analogue output) channel of DAQ board generates the positive voltage (transmit signal) and proceed through terminal 8 and 1. A 3.9 $n$F capacitance was used to allow coarse tuning of the transmit / receiver coil to excite the sample. All pulses and timing are visualised on a high performance LeCroy waverunner 6000A series oscilloscope (LeCroy Corporation, 2007, NY). During this process, the gate for receiving mode is closed. Fine tuning was carried out using a bank of switched capacitors in parallel with this main capacitor.

When the voltage associated with the control signal of the transmit pulse ends, the electromagnetic coil of the relay is not excited and the contacts separate by their own spring tension and therefore, cut the flowing current to close the

gate to end the signal transmit period.

## 5.3 Software and Processing

A set of Python commands was written to allow the system to control the EFNMR probe automatically. The programming commands start by importing modules necessary for transmit pulse generation, signal detection, processing and analysis. Different functions were assigned to the two DAQ boards that have been used in this system for signal production and detection. Before running the system all instruments were reset and ensured to be cleared to prevent the influence of any previous experiments. The system was probed to find all attached instruments by serial number and then defined the two existed instruments as DAQ1 and DAQ2. Digital channels 501 and 502 of DAQ1 and DAQ2 Figure 5.10 were set up for digital input and output respectively depending on each experimental design. This is done by resetting all bits of both DAQs to zero. The Sampling rate (in Hertz) and the length of signal acquisition (in seconds) required for DAC and ADC were specified. Specific channels in DAQ1 and DAQ2 boards were selected to perform DAC or ADC at defined sampling rates and for a set number of points Figure 5.10.

The sampling rate of the DAC in this study was set to 100 kHz, to allow accurate generation of the transmit pulse with a frequency of about 2.8 kHz required to excite $^{1}$H nuclei in the earth's magnetic field. The frequency of the excitation pulse was identified following the shimming and tuning of the transmit/receive coil with tiny variations (few Hertz) on different days even if the probe was in the same location and in similar conditions. Other parameters such as the number of repetitions and echo time (in SE sequence) was defined.

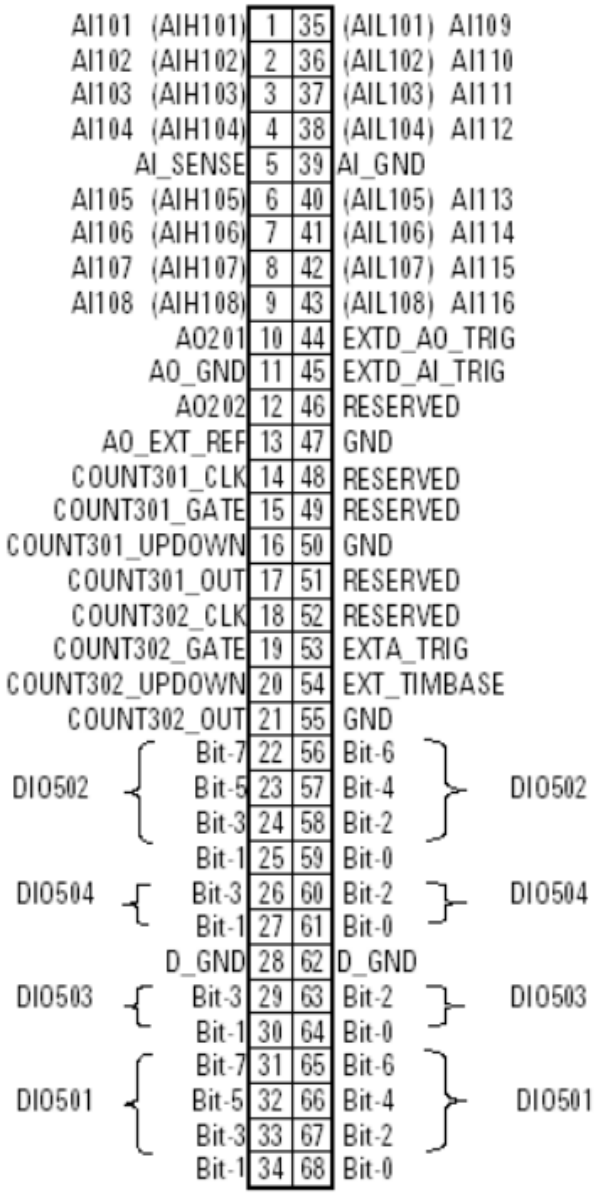


Figure 5.10: Schematic representation of DAQ connection pins. Here, channel 502 of DAQ2 used as an output source for transmit production and channel 501 of DAQ1 used as a source for NMR signal input. Channel (AIO202) of DAQ2 was used as a pulse generator. Image from (docs-europe.electrocomponents.com/webdocs/0d87/0900766b80d871b4.pdf).

When all pins on particular channels have been chosen to perform different tasks and set to zero, the pulse sequence components should be defined digitally and be ready to be generated e.g. excitation pulse signals, triggers, delays

and post processing. An effective excitation pulse can be made in different shapes such as square or using a Gaussian envelope. In this study, a Gaussian envelope was used.

The flip angle is defined by two components, pulse duration (in ms) and transmit gain (in volts). An appropriate flip angle was digitally synthesised based on operations using Python commands, a full Python code will be listed in the appendix of this thesis.

Channel (AIO202) of DAQ2 was programmed to use a buffer waveform and then the sine pulse of the transmit channel sent to it. Pin number 59 of channel DIO502 used to send a control signal and synchronised with the excitation pulse. Pin number 68 of CH 502 was triggered by the negative edge of the polarisation pulse as it detects the change in voltage related to the end of the polarisation field. The control signal of the transmit period was synchronised with the total time needed to generate excitation pulses so that it was equal to the duration needed for a number of excitation pulses and delays. Short delays before the first transmit pulse and after the last pulse are essential to avoid potential lags occurring.

After the transmit signal is sent to the coil, the system has to be ready for the incoming measurement signal. Just like triggering the transmit pulse by the negative edge of the polarising field, similarly, a control signal for the receiving period was triggered by the negative edge at the end of the control signal for the transmit period. Avoiding the ring down signal must be considered and this was done by allowing a short delay time long enough to allow this signal to decay completely but without missing major part of the NMR signal. The ring down signal appears because that the resonance system is formed by the $B_1$ coil and the associated tuning capacitance this always results in energy left in this circuit following the application of transmit pulses. The decaying factor of this voltage is estimated to be about $(exp\ (-0.5)\ in\ Q/2pi)$ cycles, more details about the ring down properties of the $B_1$ coil can be found in the (Terranova-MRI EFNMR Users Manual).

Th received NMR signal was converted from analogue to digital form to allow further analysis and for the signal to be saved and retrieved later when

needed. Fourier transformation was used to convert the FID from the time to the frequency domain. If additional processes are needed in order to enhance the detected signal such as signal averaging, the user can add more mathematical operations to the programming commands to allow the system to perform this task. When analogue data of the NMR signal has been converted to digital data a graphical representation of both the FID and the maximum signal is viewed using the (pylab) package so that data can be reviewed and analysed using numpy and scipy.

## 5.4 Experiments to optimise NMR signal using Automated EFNMR system

The results in Chapter 5 show that the automated DAQ system is capable of exciting and detecting the SABRE signal in the earth's magnetic field. This system is flexible and easy to build so that it is always amendable and can be improved to further optimise NMR signals. For example, automated capacitors can be used to tune the $B_1$ coil to excite other nuclei rather than $^1$H such as Carbon and Nitrogen. This is because these nuclei have gyromagnetic ratio lower than that of $^1$H which therefore produce much smaller signals. In this case, this method of course requires other relative modifications in the pulse sequence such as employing the best transmit pulse carrier frequency to accommodate the requirements for these other nuclei. The aim of this chapter is to characterise the SABRE signal in the earth's magnetic field using the automated purpose-built system which will provide hopefully a powerful diagnostic tool in the near future.

### 5.4.1 Tailored transmit pulse for earth's field NMR/MRI

The maximum NMR signal can only observed by applying RF pulses characterised by high selectivity in the frequency domain. This kind of pulses can be produced as single pulse of weak irradiation for a long period or as a group of hard pulses with intervening durations of free precession. The idea of selectivity is to excite spins at particular frequency without affecting the

neighbouring frequencies. For particular flip angle, selectivity can be determined by the total duration of the soft pulse if a single pulse used or by sum durations of the train of pulses.

The simplest envelope shape is the square,hard, pulse but this comes with disadvantages of having side lobes on both sides of the main signal and a very wide bandwidth. This could of course lead to ambiguous results [Bauer et al., 1984] Figure 5.11. The reason for this is that in the solenoid of the polarising field and in the volume of the receive coil, the actual field within the coil is not homogeneous. The field decreases both towards the ends of the coils and across their diameter. Thus, a wide bandwidth transmit pulse will excite more regions of the volume of the transmit coil and the signal received will also emanate from different regions with differing frequencies. In spectroscopy this means that the line width of the components of the spectra will be broader than would be predicted if the equipment were optimised, it also means that imaging experiments will have a much lower resolution that can be achieved if a more selective pulse is used.

and recangular pulse envelope.png and recangular pulse envelope.png

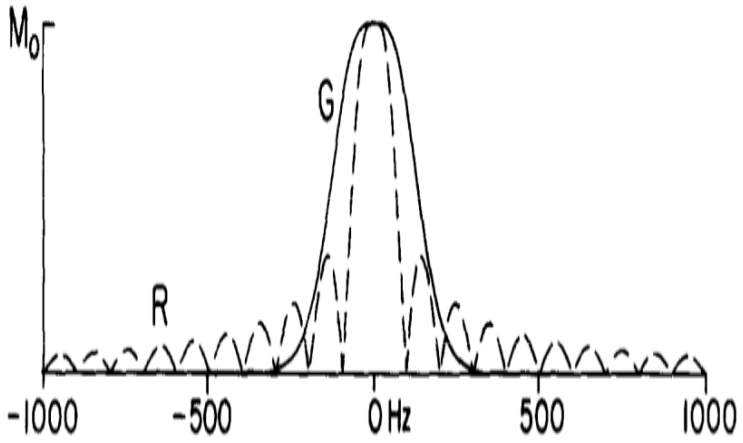


Figure 5.11: Comparison between frequency domain of Gaussian pulse (G) and Rectangular pulse (R), image from [Bauer et al., 1984].

Therefore, to suppress these unwanted side lobes and to produce a narrower main lobe, it is important to create an envelope capable of eliminating the step function discontinuity because the pulse effect on nuclear spin is not only an

approximating relationship whereas the actual excitation is from all frequency regions of the excitation pulse..

Particular algorithms within Python have been used to achieve a numerical simulation of two types of transmit pulse (square and Gaussian) in order to evaluate and optimise the performance of each shape of the pulse. The excitation by square pulse displays a broad bandwidth out to quite large frequency offsets, whilst the Gaussian pulse drops off monotonically in the frequency domain also in a Gaussian manner which leads to better selectivity Figure 5.12c, 5.12d, 5.12a, 5.12b. These results agreed with previous study conducted by [Bauer et al., 1984] Figure 5.11.

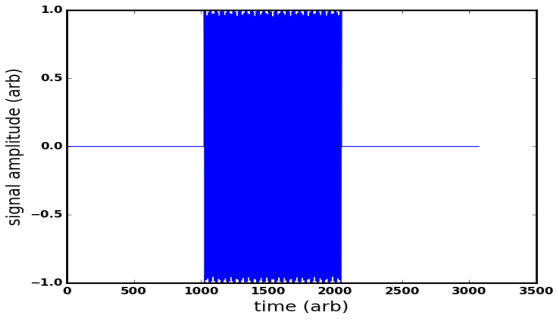


(a) Square rf pulse

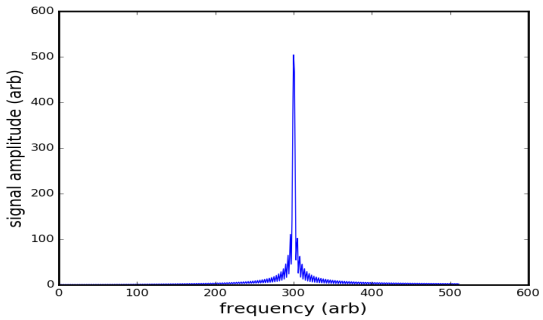


(b) Signal of square pulse after fourier transformation

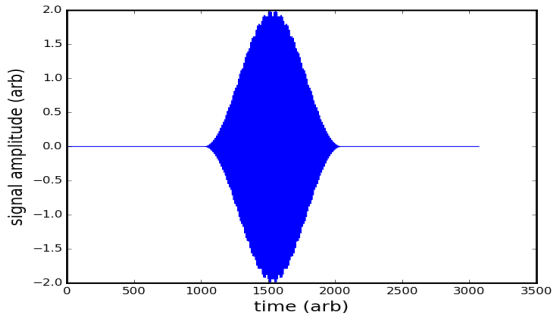


(c) Gaussian rf pulse

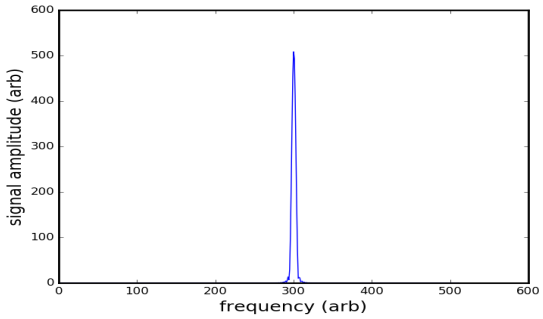


(d) Signal of Gaussain pulse after fourier transformation

Figure 5.12: Numerical simulations of (a) Gaussian envelope transmit pulse and (b) signal after Fourier transformation (c) square envelope pulse and (d) signal after Fourier transformation.

Zoomed graphs of the base lines of Figures 5.12b and 5.12d are shown in Figure 5.13a and 5.13b.

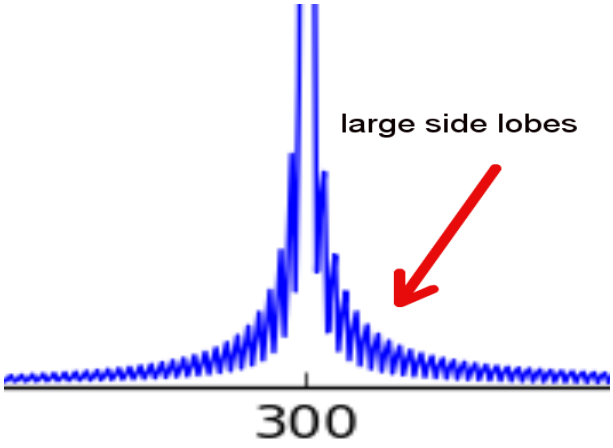


(a) Square envelope transmit pulse

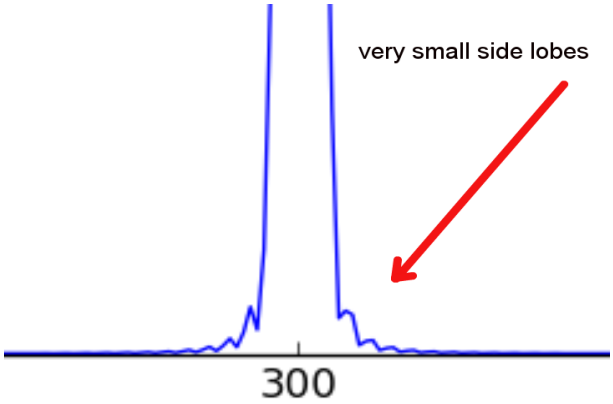


(b) Gaussian envelope transmit pulse

Figure 5.13: Zoomed views of base lines of the square and Gaussian transmit pulses showing the difference between the size of side lobes. As the size of the lobes increases the pulse becomes less selective.

### Results

Transmit pulses can be used for excitation , refocusing and inversion on nuclei of interest. So to investigate the 90° and 180° flip angle of both types of pulse envelopes, a calibration process of parametrically varying the pulse duration or transmit gain is necessary to define the maximum and minimum signals relevant to defining the 90° and 180° flip angles which will be discussed

in the next section.

Different shapes of frequency selective RF pulses which are normally used in high resolution NMR studies of liquid samples were analysed in the earth's magnetic field to investigate the optimum signal. These envelopes are Rectangular and Gaussian envelope pulses.

The following parameters have been used: Frequency 2.8 kHz, polarisation field is 18.8 mT, polarisation duration is 5s, receiver gain 50 k, acquisition time 1 s, TR is 12 s in the earth's magnetic field of about 50 microTesla. The optimum flip angle of both transmit envelope shapes have been obtained Figure 5.14. A 1.5 ms pulse duration was defined for the transmit pulse duration whereas the transmit gain has been varied from 0 to 2.0 with increments of 0.1 using a sample of 500 ml of water.

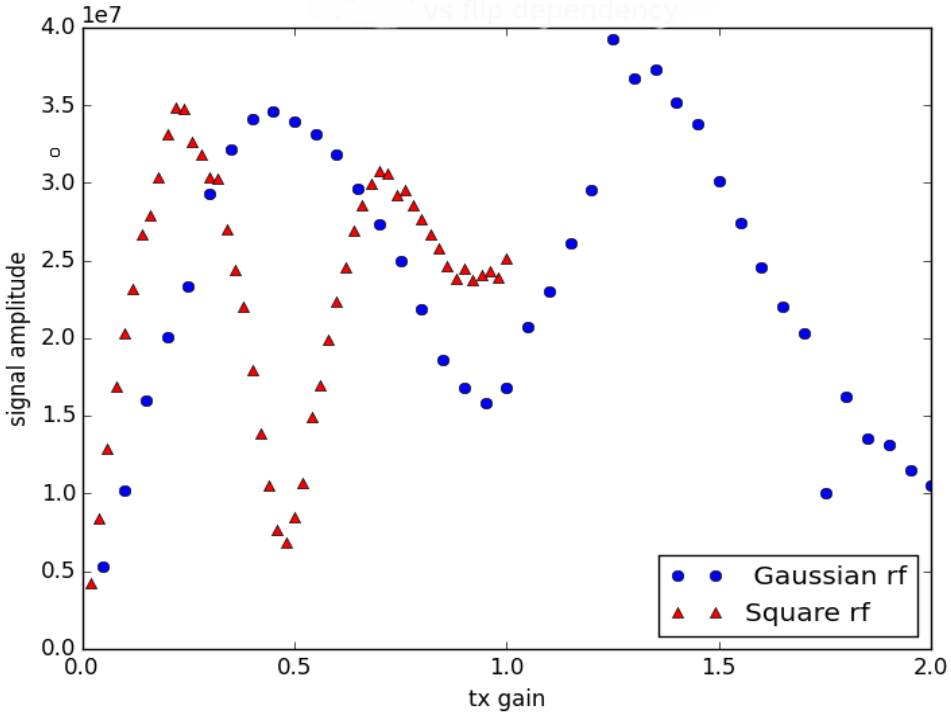


Figure 5.14: NMR signal as a function of transmit gain for rectangular and Gaussian pulses of 1.5 ms duration.

This result means that optimum signal can be reached at lower transmit gain if square RF pulse has been used. To obtain the same amount of NMR signal with Gaussian pulse about double amount of gain is required than that of

square pulse. In other words, square pulse deliver more energy than Gaussian pulse if pulse duration and transmit gain are fixed in both shapes. However, this large energy pulse is less selective Figure 5.14.

### 5.4.2 Flip angle calibration

Flip angle calibration for a given sample is important to define the appropriate 90 and 180 degree transmit pulses. The calibration of flip angle and polarisation values are particularly important every time the probe is moved from its location as the value of the earth's magnetic field and its homogeneity may change. This system is capable of changing the two main factors of flip angle (pulse duration and transmit gain) automatically. Data were collected and analysed using python where the mean is calculated for each point and plotted as shown in Figure 5.15. No data were removed due to response inaccuracy. The result shows how the NMR signal amplitude changes with different flip angles. In 500 ml water sample, the maximum signal is achieved at a transmit gain equals to 0.5 (90 degrees) and lowest signal at 1.2 gain (180 degrees) for hard, rectangular envelope pulses.

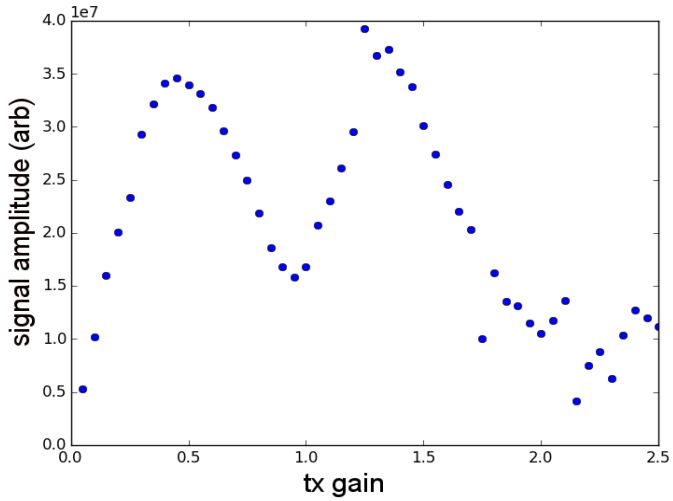


(a) Flip dependency of 500 ml water using DAQ

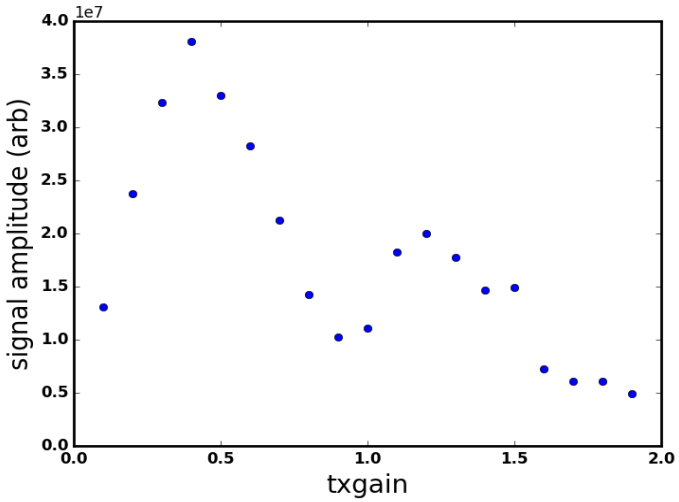


(b) Flip dependency of pyrazine using DAQ to generate the Gaussian transmit pulse

Figure 5.15: Flip dependency of (a) Water (rectangular envelope pulse) (b) Pyrazine using DAQ for transmit (Gaussian envelope pulse) and receiving.

These values can be used as the 90 and 180 degree transmit pulses respectively. However, the 90 and 180 values obtained from the 3 mg of hyperpolarised pyrazine using Gaussian excitation pulse are 0.4 and 0.8 respective. This difference may be due to 1) a dielectric effect or 2) the sample layout in the coil because the water bottle is 14 cm in length and the pyrazine sample is only 4 cm long. As the signal is then sum of all signals along the samples then one might expect the means to be the same but the bandwidth to be smaller for the pyrazine sample. In fact the flip angle dependency is different and so

this would imply that the response of the sample to the transmit pulse differs significantly.

### 5.4.3 Preamplifier Gain

A low noise (model 5113) preamplifier was used in my work. It has already predicted that increasing the preamplifier gain would increase the signal intensity of water and hyperpolarised pyrazine using the developed system. A series of experiments using the DAQ board to generate the Gaussian excitation pulse and another DAQ used to receive the detected NMR signal have been conducted. All parameters remained fixed and the preamplifier gain was varied from 0 to 50 k as follows (1 k , 2.5 k , 5 k , 10 k , 25 k , 50 k). Enhancement of water and hyperpolarised signal were probed to test the gain linearity. Figure 5.16 shows how the $^{1}$H NMR signal of both samples are proportional to the amount of gain. When the 1 k gain was employed, the resulting signal attained a minimum at a level where it is hard to distinguish between the NMR signal and the background noise signal. Signal intensities rise gradually as the gain increases from 1 k to 5 k for both samples by equal rates.

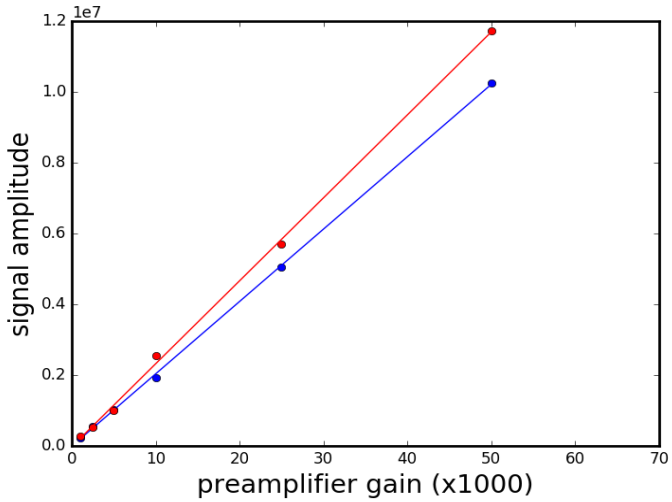


Figure 5.16: NMR signal from water (blue) and hyperpolarised pyrazine (red) as a function of preamplifier gain.

However, Figure 5.16 shows that the NMR signal increases linearly with preamplifier gain.

### 5.4.4 Signal Averaging

FID averaging is an important method used to improve the SNR in NMR images. Because the images are formed as a result of Fourier transformation of FID and averaging in the frequency domain is equivalent to averaging in the spatial domain, averaging would therefore enhance the image quality. This can be achieved by collecting several FIDs at a certain data collection position within k-space. FID averaging is expected to increase the SNR by the square root of the number of averaged FIDs [Nalcioglu and Cho, 1984].

In our experiment the total time needed for 166 averages was 36 minutes. The SNR was expected to increase as the number of FIDs increases until it reaches a point in which FID noise is not due to random uncorrelated white noise any more, but due to many other systematic errors where they present as correlated noise [Nalcioglu and Cho, 1984].

There are many possibilities for the source of the noise, first, the long term stability and drift of magnetic field and the pick up from other sources. However, in NMR imaging it is important to understand the characteristics of the system noise which basically limits the SNR , therefore limiting the improvement of image quality [Nalcioglu and Cho, 1984]. The architecture of different systems e.g RF coil design , signal processing etc [Lee and Cho, 1984] would significantly influence the noise.

In order to probe this effect, a series of experiments were conducted in which signal enhancement was monitored as a function of number of averages. The summed signal amplitude is illustrated in Figure 5.17.

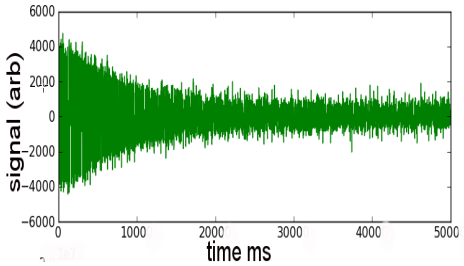


(a) water FID (on signal)

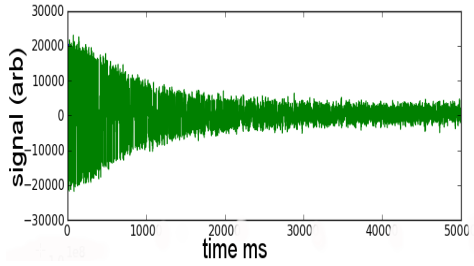


(b) water FID with 8 averages

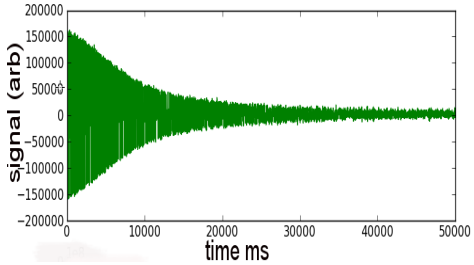


(c) water FID with 64 averages

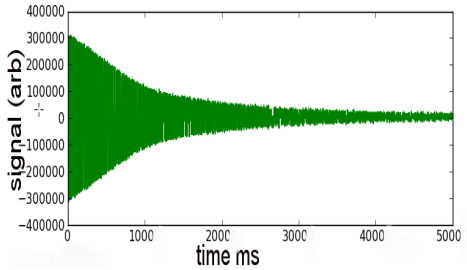


(d) water FID with 128 averages

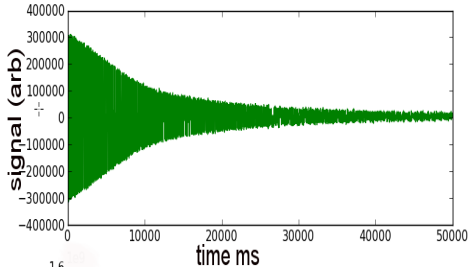


(e) water FID with 256 averages

Figure 5.17: Plots of NMR FID amplitude obtained from 500 ml of tap water as a function of the number of averages.

All parameters were fixed and number of was averages varied from 1 to 256. It is obvious that the FID of the sample increases and becomes smoother as the number of scans increases. However, averaging of the hyperpolarised signal is not feasible because the signal drops significantly even a few seconds after the first signal acquisition, which may worsen the FID as the number of scans increases.

### 5.4.5 Sample size

The magnitude of the $^{1}$H NMR signal is derived from the summed signal across the total volume of the tap water sample, so it is expected that an increase in the relative amount of water will lead to greater signal , if the number of averages remains fixed for all experiments. In order to investigate this effect, a series of experiments were conducted in which the signal magnitude was monitored as a function of sample size.

Figure 5.18 confirms that increasing the amount of water does indeed increases the magnitude of the $^{1}$H NMR signal amplitude linearly. More importantly, as the sample size increases it occupies a larger volume inside the NMR probe. Therefore, because the total signal is the sum of all signals along the sample, weaker signals will be collected from the far edges than those in the centre of the probe. The next section describes the effect of position on the total NMR signal.

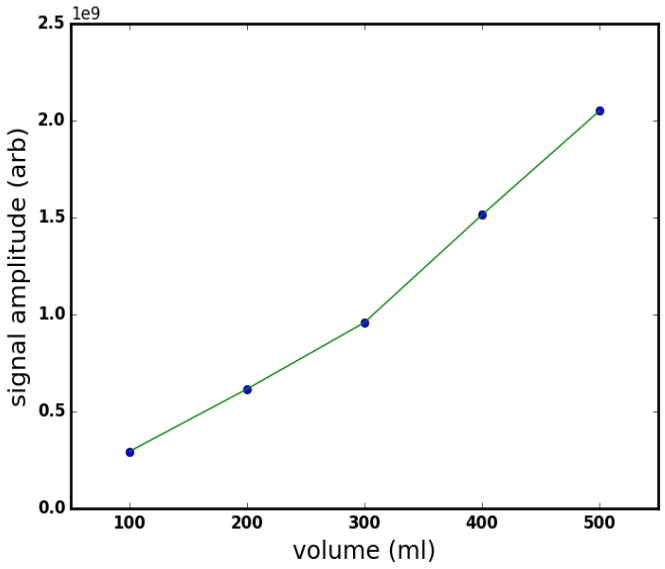


Figure 5.18: The effect of sample size on signal intensity.

### 5.4.6 Signal dependence on position inside polarisation and detection coils

The homogeneity and strength of the polarising and $B_1$ field are crucial to optimise the NMR signal. Here, then detection efficiency of the coil has been tested as a function of position. The total amount of signal was expected to vary in different positions of the along the coil. The $^1$H NMR signal from 500 ml tap water has been collected for each 2 cm of the probe Figure **??**. There is a high agreement between the calculated (blue) and measured (red) data shown in this Figure. It is clear that signal intensity is much bigger in the centre of the coil and reduced gradually as the sample moved further toward the ends. The rate of signal decline is equal on both sides of the coil. The Python mathematical operation used for the calculated curve will be included in the appendix of this thesis.

and measured B1 effeciency.png and measured B1 effeciency.png

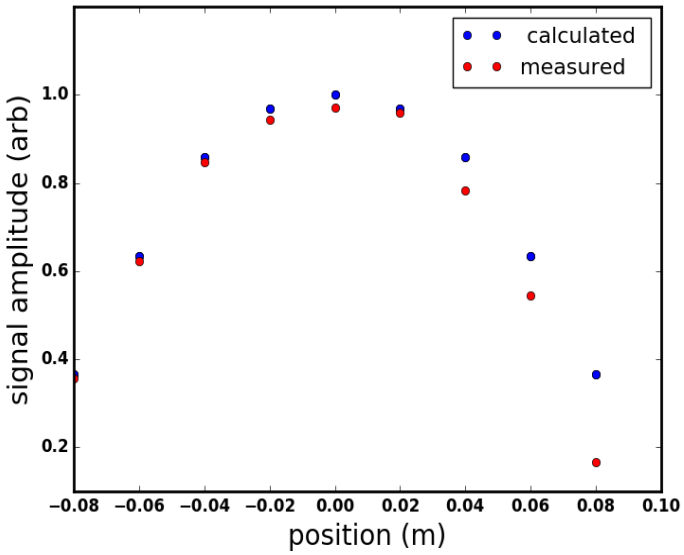


Figure 5.19: Graph showing a high agreement between the calculated and measured $B_1$ efficiency.

It can be concluded that, it is possible to improve the FID and relative NMR signal from small samples by placing it in the most efficient regions of the coil. It is also possible to optimise the signal by changing the shape of a small amount of sample to be placed in the middle of the coil.

## 5.5 Conclusions

In this chapter, an automated DAQ system working at the earth's magnetic field (about 50 micro Tesla) was presented. This system enabled then acquisition of $^1$H NMR signals of both water in thermal equilibrium and hyperpolarised pyrazine. The system was shown to provide flexible NMR measurements in the earth's magnetic field. However, further hardware and software developments are needed to boost its performance in future work.

The efficiency of this system to be used in the earth's magnetic field has been demonstrated experimentally. This includes, generating advanced sequences of shaped pulses, employing DAQ boards for both DAC and ADC and synchronisation and triggering of control signals and tx/rx pulses. Therefore, these observations serve to illustrate that the SABRE hyperpolarisation method in

earth magnetic field can be controlled automatically using DAQ system.

Furthermore, many signal optimisation methods have presented which provide a solution to overcome the lower observed signal amplitudes detected directly from the coil. This includes finding the optimum flip angle , polarisation duration , signal averaging , the effect of sample size , $B_1$ coil efficiency and the relationship between signal intensity and preamplifier gain.

# Chapter 6

# Advanced SABRE measurements in the earth's magnetic field

## 6.1 Introduction

Although it still in its infancy, the need to use SABRE for human imaging in the future will require that many limitations such as the short nuclear spin lifetime are overcome. Therefore, the optimal SABRE enhancement should be maintained for as long as possible and hence transported successfully to the region of interest. This can be done by employing an automated polariser to transport the polarised sample to the target within sufficient time but will still mean that relaxation will continue and may even be accelerated once injected into the body. The first section of this chapter will discuss the ability to polarise the sample in one place and perform the excitation and detection in another place manually as a preparation step to use the automated system [Mewis et al., 2014] in later studies. The second section will investigate the possibility of there being long lived states which can act as stores of SABRE hyperpolarisation including for $^{1}$H in the earth's magnetic field.

## 6.2 Probing SABRE using an NMR flow system

### Water

As mentioned earlier in Section 3.3.2, the EFNMR system consists of three coils Figure 3.12a. These coils are mounted together and measurements are typically performed while the sample is placed at the centre of the probe that contains these coils. Here in this chapter we separated the polarising coil from the other two coils (gradient and excitation coils). The aim of this is to polarise the sample in one place using the polarising coil and move it quickly to the $B_1$ coil for excitation and detection. The transportation of the polarised sample and the excitation and detection occurs in the earth's magnetic field.

The EFNMR probe was firstly tuned and shimmed while all coils were together in the same location. The polarising coil then was separated and placed about one meter distance from the gradient and excitation coils which remain attached Figure 6.1. First an experiment was performed using 500 ml of tap water to compare it with the SABRE signal observed from pyrazine. The water sample was held manually in the centre of the polarising coil and polarised at 18.8 mT for 6 seconds and moved immediately to the centre of the $B_1$ coil for excitation and acquisition. The time taken to move the sample from the polarising coil to the excitation coil was about 2 seconds. The parameters used were the following : polarising field 18.8 mT, polarising duration 6 s, frequency 2989 Hz, flip angle 2.6 ms, transmit gain 1.5, acquisition time 2 s, TR 12 s. This experiment was repeated 10 times, the mean and standard deviation were calculated and compared to that of the SABRE signal.

(a) The polarisation coil (b) The gradient and excitation coils

Figure 6.1: Images show how the polarisation coil (a) is separated from the gradient and excitation coils (b). Here the polarising of the sample occurs in one place and the excitation and signal are collected in a different location

**SABRE**

A second experiment was carried out by observing the signal derived from SABRE in the earth's magnetic field. The sample was prepared by dissolving 10 mg of [Ir(IMes)(COD)Cl] catalyst and 25 mg of substrate pyrazine in 3 ml $d_4-$methanol using 10 mm tubes fitted with a Young's tap. Before placing the liquid sample into the polarising coil for 6 seconds, the sample was filled with parahydrogen at 3 bar pressure and shaken for 10 seconds. The sample was then moved after polarisation immediately (about 2 seconds) to the excitation/gradient coils for measurement. Sample shaking and observations were performed in the earth's magnetic field. The parameters were used as following : polarising field 6.5 mT, polarising duration 6 s, frequency 2989 Hz, flip angle 1.5 ms, transmit gain 1.5, acquisition time 2 s, TR 12 s. This was repeated 10 times while all parameters and the experiment conditions remained fixed.

### 6.2.1 results

Figure 6.2 shows the observed signals from water at thermal equilibrium and from SABRE using the shake and drop method with a single pulse and collect pulse sequence. The signal amplitude of water was about 22 on an arbitrary scale compared to a signal amplitude of about 102 acquired from the SABRE sample. The transfer time between the polarisation and excitation (about 2 seconds) allows the bulk magnetisation that was initially built by polarisation pulse to decline significantly due to the short $T_1$ value of water and leads to a small signal compared to normal conditions when excitation occurs immediately within milliseconds after polarising the sample. However, in the case of SABRE, the process of polarisation transfer between parahydrogen and substrate (25 mg) via catalyst (10 mg) lasts for a longer time as the $T_1$ for pyrazine is an order of magnitude greater than that of water, which results in a signal about 5 times greater than that of water.

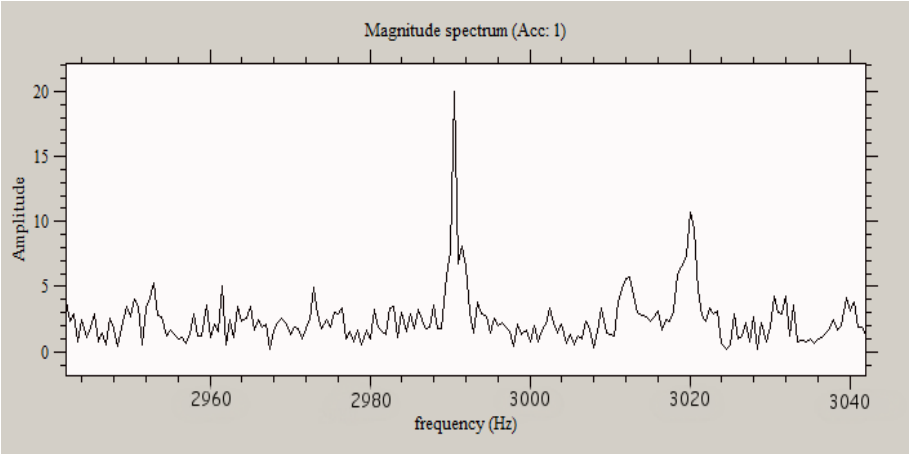


(a) Signal observed from 500 ml of water sample. The sample was polarised in 18.8 mT field in the polarisation coil and moved manually to $B_1$ coil for excitation and detection. The time taken to transport the sample was about 2 seconds.

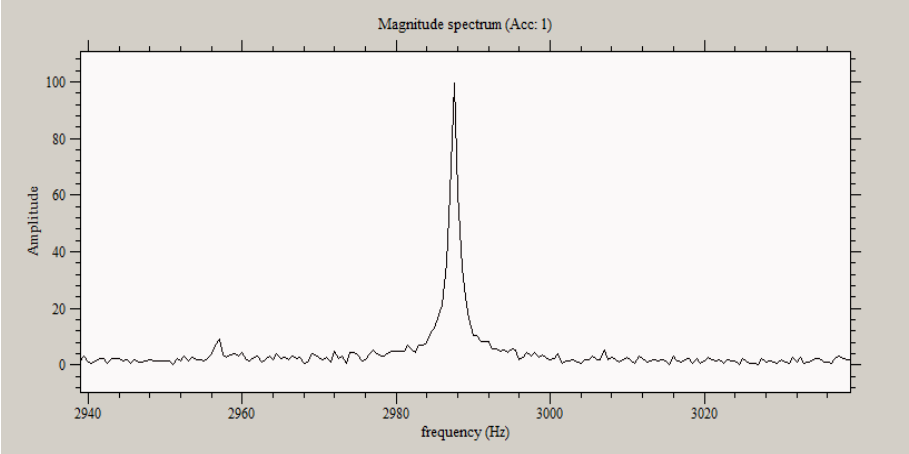


(b) Signal observed from 25 mg of hyperpolarised pyrazine. The sample was polarised in 6.5 mT field in the polarisation coil and moved manually to $b_1$ coil for excitation and detection. The time taken to transport the sample was about 2 seconds.

Figure 6.2: Images show a comparison between the signal intensities of (a) water in thermal equilibrium and (b) hyperpolarised pyrazine using separated polarisation and excitation/detection coils.

## 6.3 Long-lived states to sustain SABRE in earth's magnetic field

It is known that the applicability of MR technique in the liquid state is limited by low sensitivity and short lifetimes of nuclear spin coherence. Recently, there have been a great deal of interest in creating magnetic spins that have long lifetimes to address these issues. Nuclear singlet states are non-magnetic states of nuclear spins that may produce remarkably long lifetimes

[Carravetta et al., 2004, Carravetta and Levitt, 2004, Levitt, 2010]. For example, the decay time constant of a $^{15}N$ pair is about 25 minutes in solution [Pileio et al., 2008]. Employing spin states that have lifetimes long enough to be detectable after travelling to the region of interest inside the body would provide valuable diagnosis potential in clinical MR. Long lifetimes also have benefits to allow NMR spectroscopy to study slow motions, slow chemical exchange [Ahuja et al., 2009, Cavadini et al., 2005, Sarkar et al., 2008, Sarkar et al., 2007] , and the transport of hyperpolarised spin states [Vasos et al., 2009, Warren et al., 2009]. The singlet decay rate has also proved to carry information on the neighbouring magnetic nuclei [Tayler et al., 2010]. Of course a singlet state in itself is not observable. The state is unaffected by both magnetic fields and by excitation in that these effects rotate the state such that it has the same components with the same amplitudes.

To access the long-lived states it is important to be able to make the states evolve into an observable condition across or between the nuclei of interest. However, new methods have recently shown that it is possible to access these states even though when the nuclei are almost magnetically equivalent [Tayler and Levitt, 2011]. The spin systems are also referred to as being called nearly-equivalent or extremely-strongly-coupled when the chemical shifts of two nuclear sites are similar in which spin-spin is greater than the difference in chemical shift frequencies. Therefore, due it the fact that the spin-spin coupling suppresses the influence of the tiny chemical shift difference, the NMR spectrum of nearly-equivalent spin pairs shows a single peak. This is the case at high magnetic fields when the chemical shifts of two protons are very close, and is common situation for NMR in low fields [Tayler and Levitt, 2011].

The technique to detect signals for singlet states based on trains of 180 degree pulses that are synchronised with the spin-spin coupling between the involved nuclei. Three experimental steps are required to exploit the nuclear singlet order.

It is also possible to harness long-lived states that are derived from SABRE in high magnetic fields. An example of this is the study carried out by Olaru et al. (2016) in which it was shown that SABRE derived hyperpolarisation can be employed to build this long-lived magnetisation using 2-Aminothiazole

[Olaru et al., 2016]. In this study, the SABRE catalyst was varied to optimise the efficiency of of this process. This process demonstrated an easy and efficient route to create hyperpolarised long-lived states in seconds, Figure 6.3, that may be amendable in future for use *in-vivo* studies.

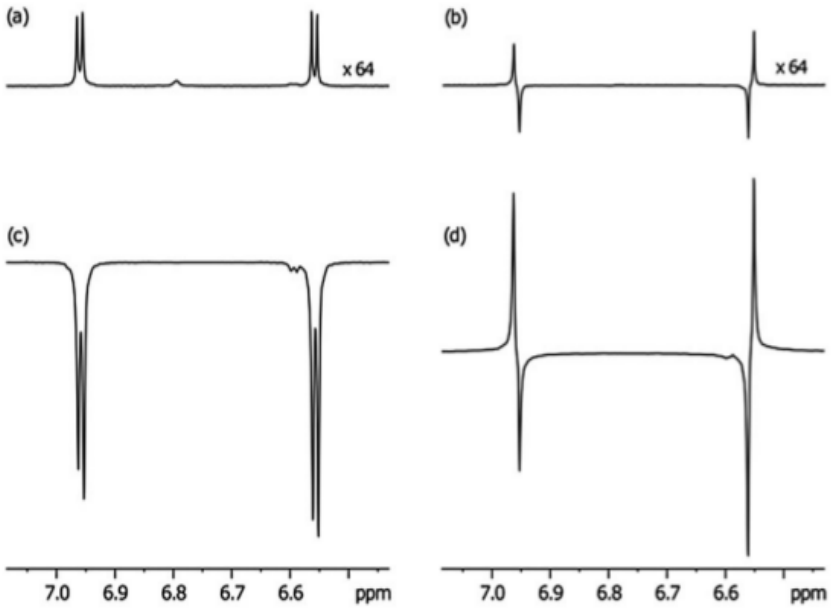


Figure 6.3: Graphs demonstrating the $^{1}$H NMR signals of Aminothiazole at 400 MHz for (a) $^{1}$H NMR spectrum taken in a single shot at thermal equilibrium (b) a $S_0$ derived spectrum of Aminothiazole which is created and investigated 1 s later by the method of Levitt, (c) the relative 3a derived SABRE hyperpolarised Aminothiazole spectrum and (d) the $S_0$ state 1 s following it was created through SABRE and a spin-lock. image taken from [Olaru et al., 2016]

.

Another example of observing long-lived states that are derived from SABRE in high field is the study done by Roy et al. (2016) in which they found more than 4 % net $^{1}$H polarisation in a long-lived form that remained observable for more than 90 seconds see Figure 6.4 by reference to pairs of protons in nicotinamide and pyrazine [Roy et al., 2016b]. The in vivo imaging of these two biologically important and safe molecules might provide a new route to study many diseases in the future.

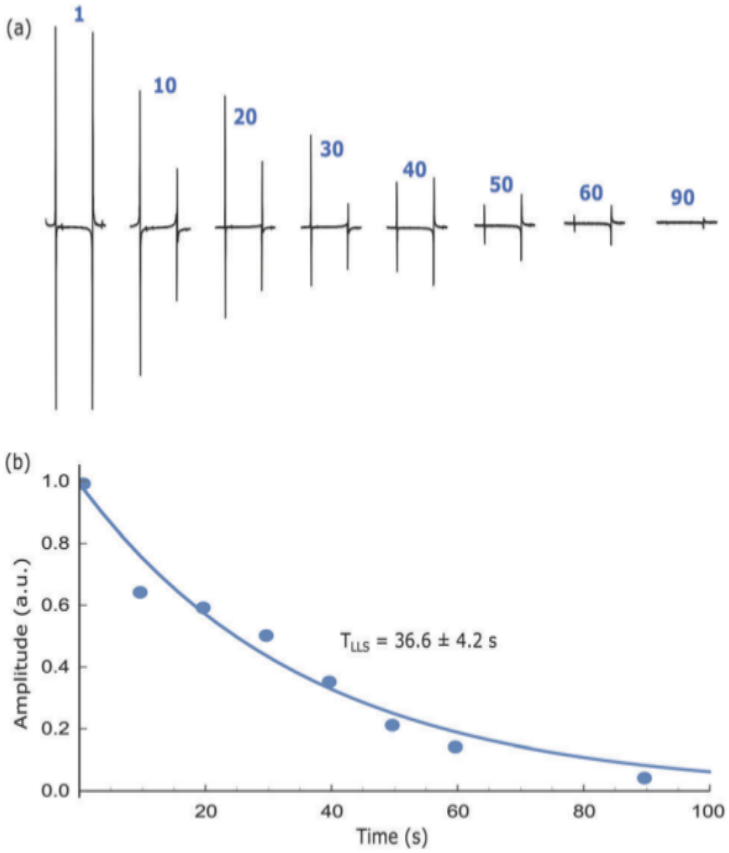


Figure 6.4: (a) Hyperpolarised singlet order based NMR spectra as a function of spin-lock duration. (b) corresponding integrated values demonstrating the signal decay due to relaxation. The $T_{LLS}$ is 36.6 ± 4.2 s and $T_1$ is about 10 s for the same system according to the exponential fit of the data. image taken from [Roy et al., 2016b].

### 6.3.1 Observing long lived states of Aminothiazole in the earth's magnetic field

Aminothiazole was chosen for its powerful features as well as its improved polarisation level gives it an advantage to act as a small molecule for metabolic measurements [Kurhanewicz et al., 2011], [Davis et al., 1998]. In addition, it has been recently used as a building block in drugs that demonstrate wide ranging activities [Kalgutkar et al., 2005], [Pieroni et al., 2014].

We used a pulse sequence 6.6 similar to that used by [Roy et al., 2016a] (figure 6.5) which consists of a polarisation field followed by a $90^{\circ}_{0}$ transmit pulse with a 90 degree phase Figure 6.8. Then, a composite pulse which consists of three

pulses ($90^{\circ}_{0}$ - $180^{\circ}_{90}$ - $90^{\circ}_{0}$ ) where the time $\tau = 1/4J$ (J about 5 Hz) is the duration between each $90^{\circ}_{0}$ and $180^{\circ}_{90}$ and J is the scalar coupling constant. The timing stability of the composite pulses were checked using the oscilloscope. The composite pulse sequences were repeated up to 96 times where the number of composite pulses increased from 1 to 96 and the observed signal recorded for each scan and the results are plotted in Figure 6.8. The best flip angle and the optimal polarisation field of Aminothiazole were employed as were optimised earlier in Chapter 4. The automated DAQ system (described in details in Chapter 5) was used to create the pulse sequence and therefore to run the experiment.

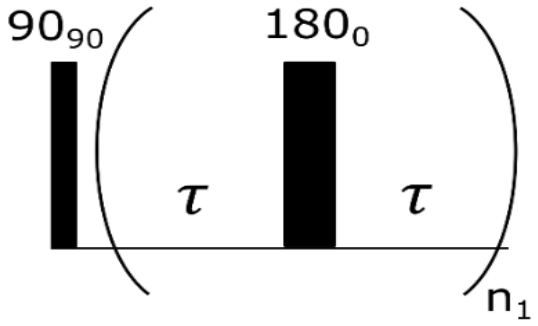


Figure 6.5: Pulse sequence used to investigate the J-synchronization experiment.Image from [Roy et al., 2016a].

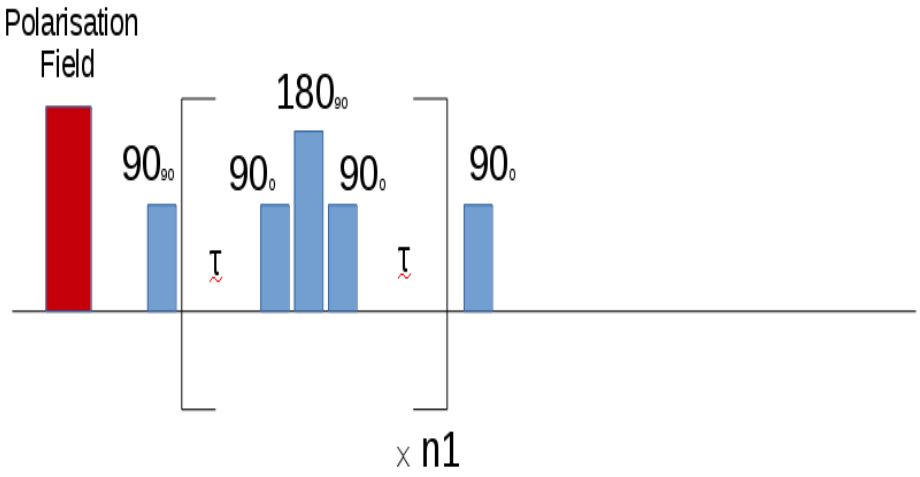


Figure 6.6: Magnetisation to singlet M2S RF pulse sequence. The Python listing for composite pulse sequence will be in the Appendix in this thesis.

An experiment was carried out to investigate how the signal amplitude of the observed magnetisation from the singlet state would change as the number of composite pulses grew varied as illustrated in Figure 6.7 while keeping $\tau$ at a constant value as was shown in [Roy et al., 2016a].

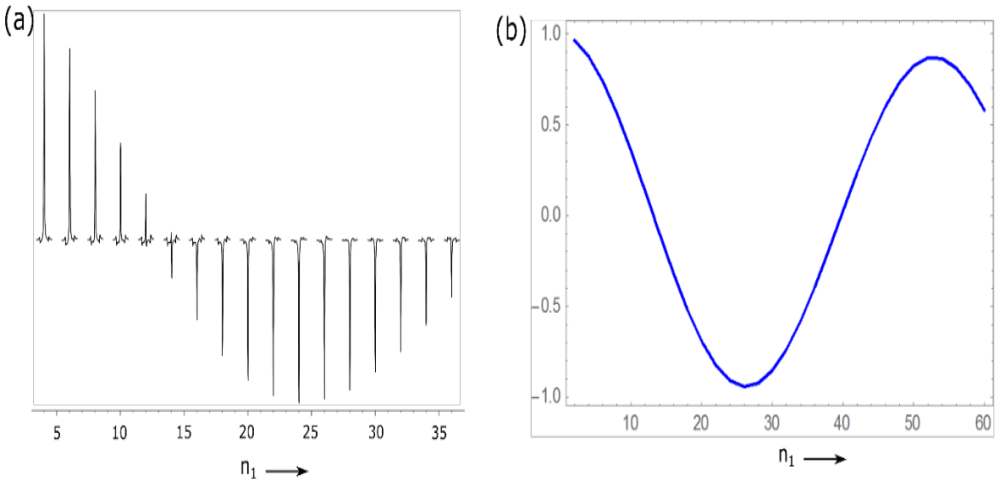


Figure 6.7: (a) $^1$H NMR based experimental spectra (b) expected signal amplitude with varying number of composite pulses while keeping $\tau$ at a constant value. Image from [Roy et al., 2016a].

However, the result see Figure 6.8 shows irregular signal amplitudes as we increased the number of pulses. For all experiments, the observed signal amplitude remained close to the level of the noise signal which means that the singlet state was not observable in this case.

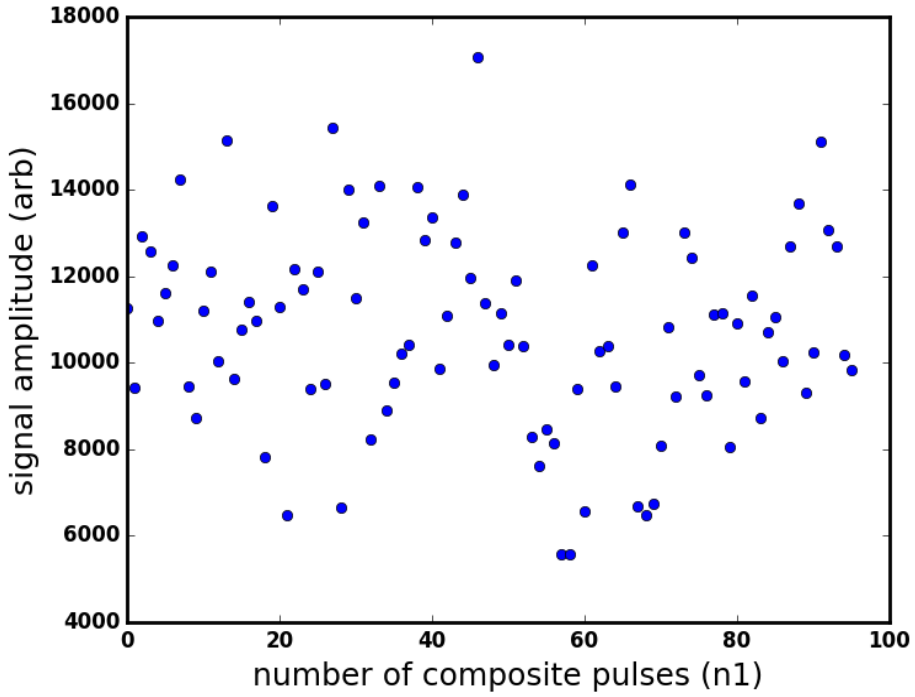


Figure 6.8: Signal amplitude vs number of composite pulses

### 6.3.2 Investigating long lived states of 3-Fluoropyridine in the earth's magnetic field

In order to obtain a spectrum of Fluorine nuclei, we can easily use the relationship $\omega$=$\gamma$B$_0$ to calculate the Larmor frequency at which Fluorine should resonate:

$$\omega_{\mathrm{F}}=\frac{\gamma_F}{\gamma_H}\omega_{\mathrm{H}}=\frac{2.517}{2.675}\omega_{\mathrm{H}}=0.941 \tag{6.1}$$

For example, if $\omega_{\mathrm{H}}$=2990Hz, then $\omega_{\mathrm{F}}$=2813Hz. Therefore, it is possible

to use the same instruments settings which typically are used for Hydrogen to record the Fluorine spectra. This is because the fluorine frequency is close to the frequency of proton. However, to acquire better Fluorine spectra the system need to be retuned. This can be done by the software-controlled capacitance C of the $B_1$ coil. It should be noted that the capacitance of the coil is related to the resonance frequency as $\omega \propto \frac{1}{\sqrt{C}}$. Further calculations are required to change the resonance frequency to that of fluorine as the following:

$$\mathrm{C_F}=\mathrm{C_H}\frac{\omega_H^2}{\omega_F^2}=\mathrm{C_H}(\frac{\gamma_H}{\gamma_F})^2=1.063^2\mathrm{C_H}=1.129\mathrm{C_H} \tag{6.2}$$

Because in our experiments we need to obtain both F and H nuclei in the same spectrum, we will choose a capacitance mid-way between the resonance capacitances of H and F. This can be doe by the following calculations:

$$\mathrm{C_{midway}}=\frac{C_H+C_F}{2}=\mathrm{C_H}(\frac{1+\frac{\gamma_H}{\gamma_F}}{2})^2=\mathrm{C_H}(\frac{1+1.129}{2})=1.065\mathrm{C_H} \tag{6.3}$$

similarly, the frequency midway between H and F resonances should be ;

$$\omega_{\mathrm{midway}}=\frac{\omega_H+\omega_F}{2}=\omega_{\mathrm{H}}(\frac{1+\frac{\gamma_H}{\gamma_F}}{2})^2=\omega_{\mathrm{H}}(\frac{1+0.941}{2})=0.970\omega_{\mathrm{H}} \tag{6.4}$$

**SABRE experiment to observe Hydrogen and Fluorin simultaneously**

The sample composition was prepared as for a single shake and drop experiments: 10 mg of IMes = 15.625 mM and 3-Fluoropyridine 98.08 g/mol so, in 1:5 proportion the amounts become 10 mg IMes : 7.66 mg of 3-Fluoropyridine in 3 ml solvent $d_4-$methanol. The sample was filled with 3 bar Parahydrogen and shaken for 10 seconds and placed in the probe. Even when measuring the enhanced signal immediately it only gave a poor enhancement of both H

and F . However, the spectra Figure 6.9 is appropriate in terms of location of the peaks and the separation is about 132 Hz with H signal resonates at 2990 Hz and F resonates at 2858 Hz Figure 6.9a. The frequency of H is at a similar frequency to that obtained from the 500 ml water Figure 6.9b. Using 90◦ flip angles were different from that used for water and shows lower levels of enhancement.

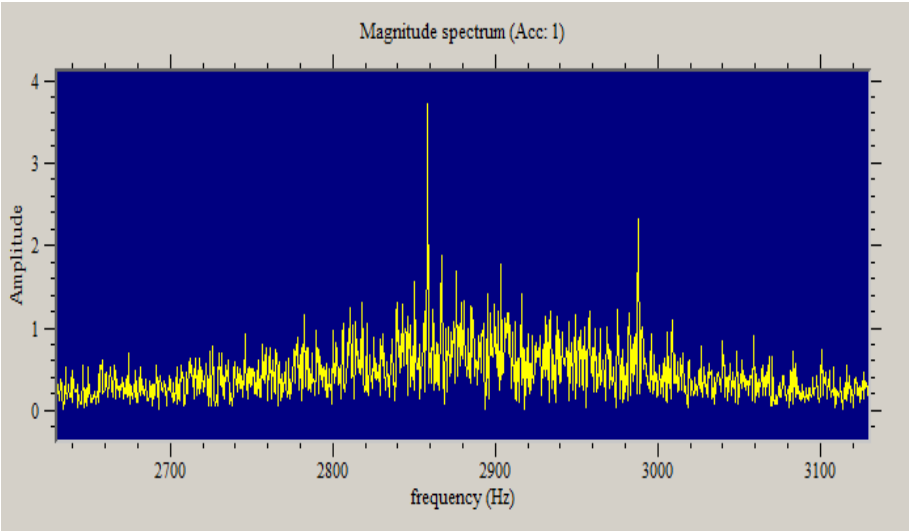


(a) 3-Fluoropyridine spectra

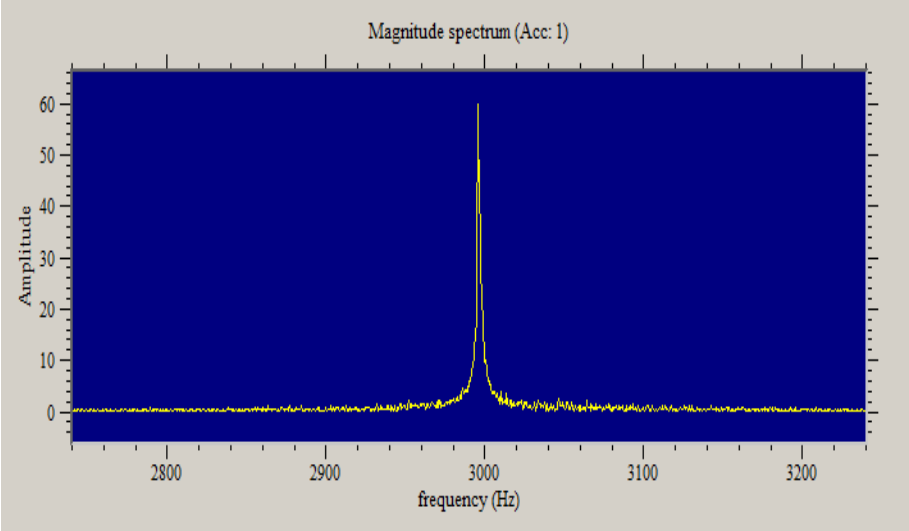


(b) Water spectrum

Figure 6.9: A comparison between (a) 3-Fluoropyridine spectra and (b) water spectrum.

We suggest that one method to overcome the poor signal is to use a raw sample that only contains 3-Fluoropyridine in 3 ml $d_4-$methanol and repeat

the experiment for 200 times to get the average signal in thermal conditions. However, we found no significant signal and this may be due to the small sample used in thermal conditions in the presence of the low magnetic field.

Although H and F are detectable, the enhancement level are still poor using SABRE and the S2M pulse sequence could not obtain the singlet state signals. This is discussed again in Chapter 7 as a possible future direction for research.

**Singlet state experiment**

The sample was prepared as in the previous experiment Section 6.3.2 and a pulse sequence was designed to observe the singlet state of the sample Figure 6.11. We used a pulse sequence similar to that used by [Roy et al., 2016a] Figure (6.10) which consists of a polarisation field followed by 90° and 180° separated by delay = 1/4J (where J about 5 Hz). Then another 90° but with phase = 90 separated by $(\frac{1}{4J} + \frac{1}{2\Delta v})$. A third 90° with 0 phase was placed after a period of time called spin lock consists of $(\frac{1}{\Delta v} + \text{delay(ms)} + \frac{1}{\Delta v})$. The first part of the pulse sequence which starts from the first 90° to the beginning of the delay period called M2S and the second part from the end of the delay to the signal acquisition called S2M.

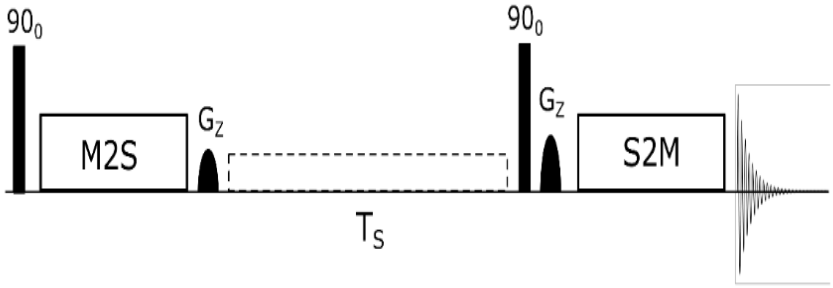


Figure 6.10: The M2S and S2M pulse sequence used to measure the singlet state lifetimes in a strongly coupled spin pair. Image from [Roy et al., 2016a].

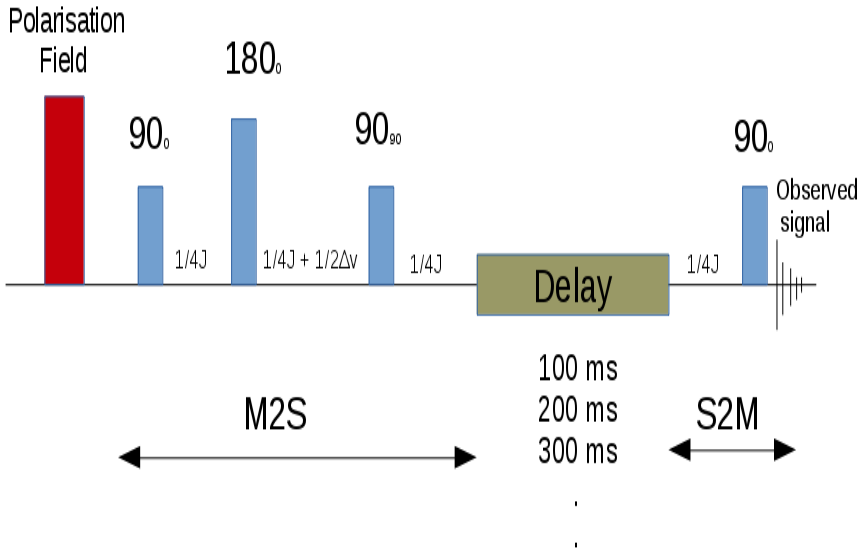


Figure 6.11: The M2S and M2S pulse sequence. All the components were fixed while the delay have been incremented from 100 ms to 2 s.

The sample was prepared, filled with parahydrogen, shaken and placed in the probe and the pulse sequence was run immediately. This was repeated several times with fixed increments of the delay time from 100 ms to 2 s. The observed signal amplitudes are plotted in Figure 6.12 to show the influence of changing the spin lock delay on the enhancement of the singlet state.

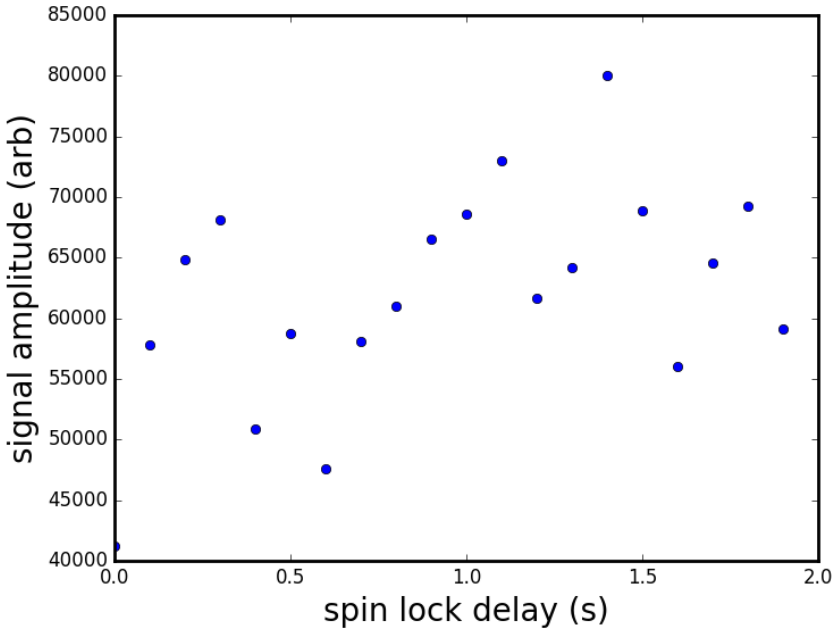


Figure 6.12: The effect of spin lock delay on the singlet state signal amplitude.

No significant signal variations observed when we increased the time delay. The only observation was an irregular signal values which were clear in Figure 6.12 and may not agree with the theory presented in [Roy et al., 2016a]. Therefore, more developments are needed to detect this effect in the earth's magnetic field. This will be discussed later in the discussion chapter.

## 6.4 Discussion and future work

The data presented in Section 6.3.1 and Section 6.3.2 show no evidence for singlet states. We used similar samples and pulse sequences as were used in [Roy et al., 2016a] which successfully created the hyperpolarised signal in $^{1}$H using SABRE and stored it in a long-lived singlet (LLS) form after suitable radiofrequency (RF) pulses. However, our results show no significant findings. This could be due to the different physics and chemistry behind the build up of singlet state which forms in the earth's magnetic field compared to that achieved in high fields [Roy et al., 2016a]. To solve this issue in the future, we would have to develop a pulse sequence with suitable transmit pulses and delays corresponding to the J-coupling in the earth's magnetic field and also

to manage the amplitude and timings of the pulses. In addition, it is may be necessary to employ much more sensitive detectors such as SQUIDs to be able to trace the tiny signals and therefore overcome the inherently poor sensitivity and insufficient nuclear spin lifetime.

## 6.5 Conclusions

The main aim of this chapter was to investigate the ability of measuring the long lived states of $^{1}$H nuclei in different substrates in the earth's magnetic field and therefore transport the sample after polarisation for excitation and detection. The results shows that it is possible to polarise the sample in one place and excite/detect the signal in another when we separate the polarisation and $B_1$ coil. However, this experiment was based on transporting the sample manually which may require an automated polariser in the future works.

# Chapter 7

# Conclusions and future work

## 7.1 Conclusions

The main aim of this project was to improve the signal enhancement of SABRE in the earth's magnetic field to afford a powerful, portable, cheap and easy to construct EFNMR system. Biocompatible substrates were chosen that would allow further studies to be extended to include living tissues and then applied to humans in the future.

In **Chapter 4**, we optimised several parameters were optimised that (if employed) would achieve the maximal possible SABRE enhancement in the earth's magnetic field. This included the calibration of the amplitude of transmit excitation pulse to find the best 90° and 180° flip angle. The 90° values were 2, 1.17, 2.17 and 0.97 for water, pyrazine, nicotinamide and aminothiazole respectively. While the 180° values were 4.16, 4.42, 4.44 and 4.70 for water, pyrazine, nicotinamide and aminothiazole respectively. I also optimised the polarisation field and there was a strong agreement between my findings and those predicted in [Adams et al., 2009b] where the values of the best possible polarisation field were 18, 6.44, 5.80 and 5.73 mT for water, pyrazine, nicotinamide and aminothiazole respectively.

In addition, I tested the effect of allowing the pressurised parahydrogen at the top of test tube to be released at particular time during the experiment and continued recording the signal which showed a sharp decline of the signal

amplitude from 14 to 4 on an arbitrary scale due to the reduced pressure immediately by the time the tube was opened. This chapter also included a comparison between signal amplitudes observed from different molecules using optimal parameters and SABRE to those of water in thermal equilibrium. Where the signal enhancement of different molecules compared to that of water were 60.7 k (k= kilo), 22.9 k and 14.02 k times greater for pyrazine, nicotinamide and aminothiazole respectively.

The decay of the SABRE signal as a function of time was also tested and compared to the same sample but containing heart tissue. We found the heart tissue does not affect the decay of the signal and that parahydrogen or substrate is interacting with the tissue. After that, the effect of multiple shakes of the sample separated by fixed time (10 min) on the signal amplitude was examined. It was found that the signal amplitude gradually decreased following every shake on an arbitrary scale as the following 160, 153, 116, 94, 96, 70, 41, 38, 35, 33, 30, 18, 13, and 5. Finally, 2D imaging of the SABRE signal was demonstrated showing the validity of using different imaging methods of 1 mm resolution image with SABRE in the earth's field due to the long persistence of the signal generated from the sample.

In **Chapter 5**, I constructed an improved proposed-built hardware and software system. This was done to enable the operator to design any pulse sequence based on DACs and ADCs to excite and detect SABRE signals in the earth's field. I successfully designed pulse sequences that consisted of trains of sine-pulse envelope (composite pulse). I was also able to shape the excitation pulse (hard or Gaussian pulses) using Python commands based on different algorithms. This system was capable of separating the transmit and detected signals automatically. Measurements observed from this system were similar to that observed from the commercial Magritek system.

In **Chapter 6**, I performed polarisation and remote detection by separating the polarisation coil from the excitation/detection coil. I compared signal amplitudes observed from water sample (about 21 on an arbitrary scale) in thermal equilibrium and SABRE hyperpolarised pyrazine (about 100 on an arbitrary scale). However, because the transportation of the samples between the two coils was done manually (about two seconds) these results were effected

by the time needed for the transmission. Therefore, an automated system is required to get more accurate results. The second part of this chapter discussed different experiments that were conducted to observe the long lived states of different molecules in earth's field. Although significant signals were observed in high fields [Roy et al., 2016a] no long lived states were observable in the earth's magnetic field when similar samples and sequences were used.

## 7.2 Future work

Using SABRE in the earth's magnetic field have been optimised in this project from different aspects including the development of automated hardware/software systems and by studying the characteristics of the SABRE molecules. Further work in the future is required, This includes:

Further work is required to achieve better signal enhancement. This can be done by, first, employing more sensitive detectors such as SQUID or SQUID untuned detector with a gradiometer [Myers et al., 2007]. This would therefore reduce the effect of the noise and increase the signal to noise ratio. In addition, because our system works best in 5-6 mT and is designed to only read out what is happening in the single $^1$H it is of great importance (instead of performing triplet to singlet magnetisation) to construct a system that would shield the magnetic field from the surrounding to allow us to go further down to the range of nanoTesla to be able to measure signals that would arise from more than one atom, e.g. singlet states.

The development of an autotuning system combined with our automated pulse sequence circuit to provide the ability to detect atoms rather than $^1$H in different molecules would be useful to investigate wider range of biologically relevant molecules. It would be beneficial to extend the investigations of SABRE in the earth's field to include the acquisition of *in-vivo* studies. This would be done by optimising a biocompatible solvent system [Spannring et al., 2016]. There is a need to employ an automated probing system for the transport of a sample and parahydrogen successfully between the polarisation and the $B_1$ coils to perform a remote SABRE measurements.

## .1 Appendix A. Python codes

### .1.1 The code to run the singlet to magnetisation experiment

```
# S2M

from visa import *
import struct
import pylab
import numpy
from time import sleep
from scipy.signal import hilbert
import binascii
import ctypes
import scipy
import scipy.signal
from scipy import stats
import scipy.signal.signaltools as sigtool
from datetime import datetime




def find_instrument_by_serial(serial):
    all_instruments=get_instruments_list(False)
    #print(all_instruments)
    no_instruments=len(all_instruments)

    for i in range(no_instruments) :
        curr_instrument=instrument(all_instruments[i])
        #print curr_instrument
```

```
            # replace it.
            instname = all_instruments[i].split('::')
            if len(instname) >= 3:
                if instname[2] == '7704':
                    continue


            try:
                curr_instrument.write('*IDN?')
                model=curr_instrument.read()
                # Find the serial number as the 3rd element and if it
                # matches, return the instrument object
                if model.split(',')[2] == serial:
                    return curr_instrument
            except VisaIOError, e:
                pass

        return None

YNIC_ALIASES = {'DAQ1': 'TW51431501',
                'DAQ2': 'TW51061551',
                'WAVEGEN1': 'MY48490007',
                'WAVEGEN2': 'MY48480010',
                'MULTIMETER': 'MY48330044',
                'SWITCH': 'MY52390003'}

def find_instrument(alias):
    return find_instrument_by_serial(YNIC_ALIASES[alias])

#do interactive plotting
pylab.ion()
pylab.close('all')



daq1_instrument=find_instrument('DAQ1')
```

```
daq2_instrument=find_instrument('DAQ2')
wavgen1_instrument=find_instrument('WAVEGEN1')
switch1_instrument=find_instrument('SWITCH')

#reset all the instruments and ensure they are clear (page 53)
daq1_instrument.write("*RST")
daq2_instrument.write("*RST")
wavgen1_instrument.write("*RST")
switch1_instrument.write("*CLS")
switch1_instrument.write("*RST")
switch1_instrument.write("*IDN?")
switch1_instrument.read()

#Configure the digital channel to INPUT
#Configure the digital channel as OUTPUT (page 59)

daq2_instrument.write("CONF:DIG:DIR INP, (@501)")
daq2_instrument.write("CONF:DIG:DIR OUTP, (@502)")
#also set digital output on daq1
daq1_instrument.write("CONF:DIG:DIR OUTP, (@502)")
#set all bits to zero on channel 502 for both daq1 and daq2
daq2_instrument.write("SOUR:DIG:DATA 0, (@502)")
daq1_instrument.write("SOUR:DIG:DATA 0, (@502)")
delay_clock=45000000
# Set sample rate and length of aquisition (in Hz and s)
#for the analogue to digital converter
acq_samp_rate = 50000
#for the digital to analogue converter
dac_samp_rate=100000
#how long we acquire for in seconds


acq_dur = 2
```

```
sum_fid=numpy.zeros((acq_dur*acq_samp_rate,))
fft_fid=numpy.zeros((acq_dur*acq_samp_rate,))
counter = 1


gain_step=0.05
freq=2986



max_count=1
max_value=numpy.zeros((max_count+1,1))
for inc in range(1,max_count+1):


    #set all bits to zero on channel 502 for both daq1 and daq2
    daq2_instrument.write("SOUR:DIG:DATA 0, (@502)")
    daq1_instrument.write("SOUR:DIG:DATA 0, (@502)")
    #dac_dur=dac_step

    #analog to digital conversion
    #this sets daq1 to do adc on channel 101
    #at a sampling rate and for a set number of points
    daq1_instrument.write("ROUT:SCAN (@101)")
    daq1_instrument.write("ACQ:SRAT %d" % acq_samp_rate)
    daq1_instrument.write("ACQ:POIN %d" % (acq_samp_rate*acq_dur))


    dac_dur = 0.0015    # 90 dac duration
    dac_dur2 = 0.0015
    adc_delay=int((dac_dur+0.050)*delay_clock)

    #set up dac waveform
```

```
sig_no_pts=int(dac_dur*dac_samp_rate)
t_mask=numpy.linspace(0,1.0, sig_no_pts)
mask=(1.0-numpy.cos(2.0*numpy.pi*t_mask))/2.
\begin{lstlisting}

sig_no_pts2=int(dac_dur2*dac_samp_rate)
t_mask2=numpy.linspace(0,1.0, sig_no_pts2)
#mask2=(1.0-numpy.cos(2.0*numpy.pi*t_mask2))/2.

#mask=numpy.ones(numpy.shape(t_mask))
#mask[0]=0.0
#mask[-1]=0.0
#pylab.plot(mask)

mask2=numpy.ones(numpy.shape(t_mask))
mask2[0]=0.0
mask2[-1]=0.0
#pylab.plot(mask2)




tx_gain= 0.5      #transmit gain ''initial 90  (phase = 90)
buffer_dur=0.001     #1 mseconds
buffer_pts=int(buffer_dur*dac_samp_rate)
buffer1=numpy.ones(buffer_pts)*32768

t_carrier=numpy.linspace(0,dac_dur, sig_no_pts)
carrier=tx_gain*numpy.sin(2.0*numpy.pi*t_carrier*freq)
sinpulse=((0.5 *(mask* carrier+1.00)*65375.0)).astype(int)

tj=0.0125         # tj/4  delay
tj4= 0.070
# composite pulse (90, 180, 90)
```

```
    tx_gain2= tx_gain          # 90 (phase = 90)
    buffer_dur2=tj
    buffer_pts2=int(buffer_dur2*dac_samp_rate)
    buffer2=numpy.ones(buffer_pts2)*32768
    t_carrier2=numpy.linspace(0,dac_dur, sig_no_pts)
    carrier2=tx_gain2*numpy.sin(2.0*numpy.pi*t_carrier2*freq + 1.57)
    sinpulse2=((0.5 *(mask* carrier2+1.00)*65375.0)).astype(int)



    tx_gain3= 1.0          #240  (phase = 0)
    buffer_dur3=buffer_dur # time between 90 and 240
    buffer_pts3=int(buffer_dur3*dac_samp_rate)
    buffer3=numpy.ones(buffer_pts3)*32768
    t_carrier3=numpy.linspace(0,dac_dur, sig_no_pts2)
    carrier3=tx_gain3*numpy.sin(2.0*numpy.pi*t_carrier3*freq)
    sinpulse3=((0.5 *(mask* carrier3+1.00)*65375.0)).astype(int)



    #S2M   N1=....    , N2 =....

    rf_sig=numpy.concatenate((buffer1,sinpulse))        #90 (phase = 0)
# first 90 rf pulse

    rf_sig=numpy.concatenate((rf_sig,buffer2))   # 1/4  tj

    composite_sig=numpy.concatenate((buffer1  , sinpulse2))
#90   (phase=90)              #1      # composite pulse
    composite_sig=numpy.concatenate((composite_sig,sinpulse3))
#180  (0)
```

```
    composite_sig=numpy.concatenate((composite_sig,sinpulse2))
#90    (phase=90)

    composite_sig=numpy.concatenate((composite_sig,buffer2))
# (1/4 tj)



    transmit_sig=numpy.concatenate((rf_sig, composite_sig ))
# transmite signal = rf pulse + composite signal

    for x in range(96):
        transmit_sig=numpy.concatenate((transmit_sig, composite_sig ))

        dacval=tuple(transmit_sig)    # digital to analog

        #dacval=tuple(sinpulse)
        l=len(dacval)

        s = struct.pack('<%dh' % l, *dacval)
        comm ="DATA:USER #8%.8d" % (2*l)
        comm += s

        #set daq2 for dac operation
        #turn the dac off
        daq2_instrument.write("OUTP OFF")
        #say which dac to use ie dac1
        daq2_instrument.write("ROUT:ENAB ON, (@201)")

        #send the waveform to the buffer
        daq2_instrument.write(comm)

        #say how many times to send the waveform out
        daq2_instrument.write("OUTP:WAV:ITER 1")
```

```
#set the dac sampling rate
daq2_instrument.write("OUTP:WAV:SRAT 100000")

#tell the dac that it is using the buffer waveform

daq2_instrument.write("APPL:USER (@201)")




#tx period
#select the trigger to be external on extd A0 trig (page 78)
daq2_instrument.write("OUTP:TRIG:SOUR EXTD")


#say what the trigger type is
daq2_instrument.write("OUTP:TRIG:DTRG:POL POS")
daq2_instrument.write("OUTP:TRIG:TYPE DEL")


daq2_instrument.write("OUTP:TRIG:DCNT 100")


daq2_instrument.write("OUTP ON")


#rx period
#also set up adc to be triggered (page 78)
daq1_instrument.write("TRIG:SOUR EXTD")
#trigger is positive going edge
daq1_instrument.write("TRIG:DTRG:POL POS")
#daq1_instrument.write("TRIG:TYP POST")
```

```
        daq1_instrument.write("TRIG:TYP DEL")
        adc_delay=int((dac_dur+0.002+0.1 + 2.5444)*delay_clock)
#### rx period delay
        daq1_instrument.write("TRIG:DCNT "+str(adc_delay))
#for how long the rx delay is ?
        #starts acquisition
        daq1_instrument.write("DIG")









        #but does not do anything until trigger pulse
        # received on line 44

        #this code detects the polarisation gate signal going
        #from 1 on bit 0 to 0 on bit 0
        #this is detected on digital lines going into 501 on line 68
        t1=0
        t2=0

        while t1==0 :
            daq2_instrument.write("MEAS:DIG:BIT? 0,(@501)")
# To read back the digital value of bit 0 at channel 501
            trig_level=daq2_instrument.read()
            #print int(trig_level)
            if trig_level=='1' :
                #now get when goes back to 0
                t1=1
                while t2==0 :
                    daq2_instrument.write("MEAS:DIG:BIT? 0,(@501)")
                    trig_level=daq2_instrument.read()
                    if trig_level=='0' :
```

```
                        #negative edge on bit 1 for daq2
                        daq2_instrument.write("SOUR:DIG:DATA 1, (@502)")



                        #negative edge on bit 1 for daq1
                        daq1_instrument.write("SOUR:DIG:DATA 1, (@502)")


                        t2=1

            #has sent trigger to DAC and to ADC
            #so wait for a little while until we switch to receive mode




            #wait 105 msecond to allow transmit of second pulse
            stime2 = etime = time.time()
            tgttime = stime2 + 0.8
#   duration of tx period  (... msec)
            while etime < tgttime:
                etime = time.time()
            daq2_instrument.write("SOUR:DIG:DATA 0, (@502)") #line 59
            #about to enter receive mode so can collect data
            #this switches us to receive mode

            daq2_instrument.write("SOUR:DIG:DATA 2, (@502)")
            #sets the switch to allow signal through unit 1
```

```
        #wait 30 msecond to open next channel
# line 25
        stime2 = etime = time.time()
        tgttime = stime2 + 0.030
        while etime < tgttime:
            etime = time.time()



        daq1_instrument.write("SOUR:DIG:DATA 6, (@502)")
         #sets the switch to allow signal through unit 1 and unit 3
                                                        #line 58
        #wait until acquisition has finished
        while True :
            daq1_instrument.write("WAV:COMP?")
            if daq1_instrument.read() =='YES':
                break
        #print 'finished a run'




        daq1_instrument.write("WAV:DATA?")
        res=daq1_instrument.read()
        numpts = int(res[2:10])/2
        #print 'Unpacking %d points' % numpts
        data = struct.unpack('%dh' % numpts, res[10:])
        data_a = numpy.array(data)
        sum_fid = sum_fid + data_a
```

```
mean_fid = sum_fid/counter


#data_a=numpy.mean(data_a)
#ifreq = numpy.diff(numpy.unwrap(numpy.angle(hilbert(data_a))))
freqs = numpy.fft.fftfreq(numpts,1.0/acq_samp_rate)




pylab.close('all')
pylab.subplot(211)

#data_a=numpy.mean(data_a)

pylab.plot(mean_fid[0:sig_no_pts])
pylab.plot(mean_fid) ###fid



#pylab.plot(mean_fid[0:200])
pylab.subplot(212)
freq_data=numpy.fft.fft(data_a)
fft_fid=fft_fid+freq_data

pylab.plot(transmit_sig) # to plot the rf signal



#print('gain %f' % tx_gain)
print( 'max value is %f ' %max_value[inc])
```

```
        #switching back to transmit
        #daq2_instrument.write("SOUR:DIG:DATA 0, (@502)")

        counter = counter =+1
```

### .1.2 Analytical solution field along the axis of the B1 coil

```
import numpy
from matplotlib import *
import pylab
from numpy import *
from matplotlib.pyplot import *


R= 0.041          # Coil radius in metres
maxz = 0.081      # maximum z value for calculation
minz = -0.080     # minimum z value for calculation
stepz = 0.02     # step size along the z axis
leng = 0.130       # length of coil in metres
N= 4160           # Number of turns
I= 1              # Current



B1 =np.arange (0 ,(maxz-minz)/stepz ,1)
cnt = 0


for z in arange(minz , maxz , stepz): # Step along z axis
```

```
    B1[cnt] = -((z-leng/2)/sqrt(R**2+(z-leng/2)**2))
    B1[cnt] = B1[cnt]+((z+leng/2)/sqrt(R**2+(z+leng/2)**2))
    cnt = cnt + 1

#.....................................................
# Calculate B1 as function of position
    x = np.arange(minz,maxz,stepz)
    B1 = I*4*B1*pi*1e-7*N/(leng*2)
#.....................................................


# Calculate efficiency of B1 coil to detect magnetization
effB1 = B1/max(B1)
plot(x,effB1 , 'o')

plot(x,effB1 )
ylim(0 , 1.1)


xlabel('position m')
ylabel ('effeciency')

title("Detection efficiency of B1")
```

# Glossary

| | |
|---|---|
| 2D | Two dimensional |
| 3D | Three dimensional |
| AI | Analogue Input |
| ALTADENA | Adiabatic Longitudinal Transfer After Dissociation Engender Nuclear Align |
| AC | Alternating Current |
| ADC | Analogue to Digital Converter |
| AO | Analogue Output |
| ATP | Adenosine TriPhosphate |
| BJT | Bipolar Junction Transistor |
| CE | Cross Effect |
| COPD | Chronic Obstructive Pulmonary Disease |
| COSY | COrrelation SPectroscopy |
| CPMG | Carr-Purcell-Meiboom-Gill |
| CSF | CerebroSpinal Fluid |
| DAQ | Data AQuisition |
| DC | Direct Current |
| DI | Digital Input |
| DIO | Digital Input/Output Module |
| DNP | Dynamic Nuclear Polarisation |
| DO | Digital Output |
| DSP | Digital Signal Processor |
| EEPROM | Electrically Erasable Programmable Read Only Memory |
| EFNMR | Earth Field Nuclear Magnetic Resonance |
| EPR | Electron Paramagnetic Resonance |
| FFT | Fast Fourier Transform |
| FID | Free Induction Decay |
| FIFO | First In First Out |
| fMRI | Functional Magnetic Resonance Imaging |
| FOV | Field Of View |
| GE | Gradient Echo |
| GF | Frequency Gradient |

| | |
|---|---|
| GS | Slice selective Gradient |
| GP | Phase Gradient |
| GPIO | General- Purpose digital I/O |
| HP | HyperPolarisation |
| INEPT | Insensitive Nuclei Enhancement By Polarisation Transfer |
| IR | Inversion Recovery |
| LLS | Long-Lived Singlet |
| MEG | MagnetoEncephaloGraphy |
| MR | Magnetic Resonance |
| MRI | Magnetic Resonance Imaging |
| MRS | Magnetic Resonance Spectroscopy |
| MSR | Magnetically Shielded Room |
| NMR | Nuclear Magnetic Resonance |
| NMV | Net Magnetic Vector |
| NOE | Nuclear Overhauser Effect |
| NPN | transistor with P-doped semiconductor (the "base") between two N-doped layers |
| OPSY | Only Parahydrogen SpectrscopY |
| PASADENA | Parahydrogen And Synthesis Allow Dramatically Enhanced Nuclear Alignment |
| PC | Personal Computer |
| PCC | Printed planar resonance Copper Coil |
| PD | Proton Density |
| PGA | Programmable Gain and AC/DC coupling |
| PHIP | ParaHydrogen Induced Polarisation |
| ppm | parts per million |
| PSGE | Pulse Gradient Spin Echo |
| RAD | Radian |
| RF | Radio Frequency, sometimes referred to as (rf) |
| RT | Room-Temperature |
| SABRE | Signal Amplification By Reversible Exchange |
| SD | Standard Deviation |
| SE | Spin Echo |

| | |
|---|---|
| SNR | Signal to Noise Ratio |
| SQUID | Superconducting Quantum Interference Device |
| SSI | Simple Serial Interface |
| TE | Echo Time |
| TM | Thermal Mixing |
| TOCSY | TOtal Correlated SpectroscopY |
| TR | Repetition Time |
| TSC1 | Tuned SQUID Circuit (TSC) |
| ULF | Ultra Low magnetic Field (or Ultra-low Frequency) |
| USB | Universal Serial Bus |
| WCC | Wire-wound resonance Copper Coil |

# Bibliography

[Abragam and Goldman, 1978] Abragam, A. and Goldman, M. (1978). Principles of dynamic nuclear polarisation. *Reports on Progress in Physics*, 41(3):395.

[Abragam et al., 1982] Abragam, A., Goldman, M., and Redfield, A. G. (1982). Nuclear magnetism: Order and disorder. *Physics Today*, 35:61.

[Adams et al., 2009a] Adams, R. W., Aguilar, J. A., Atkinson, K. D., Cowley, M. J., Elliott, P. I., Duckett, S. B., Green, G. G., Khazal, I. G., López-Serrano, J., and Williamson, D. C. (2009a). Reversible interactions with para-hydrogen enhance nmr sensitivity by polarization transfer. *Science*, 323(5922):1708–1711.

[Adams et al., 2009b] Adams, R. W., Duckett, S. B., Green, R. A., Williamson, D. C., and Green, G. G. (2009b). A theoretical basis for spontaneous polarization transfer in non-hydrogenative parahydrogen-induced polarization. *The Journal of chemical physics*, 131(19):194505.

[Aguilar et al., 2007] Aguilar, J. A., Elliott, P. I., Lopez-Serrano, J., Adams, R. W., and Duckett, S. B. (2007). Only para-hydrogen spectroscopy (opsy), a technique for the selective observation of para-hydrogen enhanced nmr signals. *Chemical Communications*, (11):1183–1185.

[Ahuja et al., 2009] Ahuja, P., Sarkar, R., Vasos, P. R., and Bodenhausen, G. (2009). Diffusion coefficients of biomolecules using long-lived spin states. *Journal of the American Chemical Society*, 131(22):7498–7499.

[Altes and Salerno, 2004] Altes, T. A. and Salerno, M. (2004). Hyperpolarized gas mr imaging of the lung. *Journal of thoracic imaging*, 19(4):250–258.

[Ardenkjær-Larsen et al., 2003] Ardenkjær-Larsen, J. H., Fridlund, B., Gram, A., Hansson, G., Hansson, L., Lerche, M. H., Servin, R., Thaning, M., and Golman, K. (2003). Increase in signal-to-noise ratio of¿ 10,000 times in liquid-state nmr. *Proceedings of the National Academy of Sciences*, 100(18):10158–10163.

[Asfour, 2011] Asfour, A. (2011). Low-field nmr/mri systems using labview and advanced data acquisition techniques. *Practical Applications and Solutions Using Labview TM Software*, pages 17–40.

[Atkins and De Paula, 2006] Atkins, P. and De Paula, J. (2006). Atkins physical chemistry, chapter 5.

[Atkinson et al., 2008] Atkinson, K. D., Cowley, M. J., Duckett, S. B., Elliott, P. I., Green, G. G., López-Serrano, J., Khazal, I. G., and Whitwood, A. C. (2008). Para-hydrogen induced polarization without incorporation of para-hydrogen into the analyte. *Inorganic chemistry*, 48(2):663–670.

[Atkinson et al., 2009] Atkinson, K. D., Cowley, M. J., Elliott, P. I., Duckett, S. B., Green, G. G., Lopez-Serrano, J., and Whitwood, A. C. (2009). Spontaneous transfer of para hydrogen derived spin order to pyridine at low magnetic field. *Journal of the American Chemical Society*, 131(37):13362–13368.

[Banerjee et al., 2013] Banerjee, D., Shimon, D., Feintuch, A., Vega, S., and Goldfarb, D. (2013). The interplay between the solid effect and the cross effect mechanisms in solid state 13 c dnp at 95ghz using trityl radicals. *Journal of Magnetic Resonance*, 230:212–219.

[Bauer et al., 1984] Bauer, C., Freeman, R., Frenkiel, T., Keeler, J., and Shaka, A. (1984). Gaussian pulses. *Journal of Magnetic Resonance (1969)*, 58(3):442–457.

[Béné, 1967] Béné, G. (1967). High resolution nmr spectroscopy in the terrestrial magnetic field range. *Magnetic Resonance and Relaxation, North-Holland Publishing Company, Amsterdam*, pages 903–916.

[Bennett et al., 1996] Bennett, L., Wang, P., and Donahue, M. (1996). Artifacts in magnetic resonance imaging from metals. *Journal of applied physics*, 79(8):4712–4714.

[Bernarding et al., 2006] Bernarding, J., Buntkowsky, G., Macholl, S., Hartwig, S., Burghoff, M., and Trahms, L. (2006). J-coupling nuclear magnetic resonance spectroscopy of liquids in nt fields. *Journal of the American Chemical Society*, 128(3):714–715.

[Blanchard et al., 2013] Blanchard, J. W., Ledbetter, M. P., Theis, T., Butler, M. C., Budker, D., and Pines, A. (2013). High-resolution zero-field nmr j-spectroscopy of aromatic compounds. *Journal of the American Chemical Society*, 135(9):3607–3612.

[Bloch, 1946] Bloch, F. (1946). Nuclear induction. *Physical review*, 70(7-8):460.

[Bottomley and Andrew, 1978] Bottomley, P. A. and Andrew, E. R. (1978). Rf magnetic field penetration, phase shift and power dissipation in biological tissue: implications for nmr imaging. *Physics in Medicine and biology*, 23(4):630.

[Bowers and Weitekamp, 1986] Bowers, C. R. and Weitekamp, D. P. (1986). Transformation of symmetrization order to nuclear-spin magnetization by chemical reaction and nuclear magnetic resonance. *Physical review letters*, 57(21):2645.

[Bowers and Weitekamp, 1987] Bowers, C. R. and Weitekamp, D. P. (1987). Parahydrogen and synthesis allow dramatically enhanced nuclear alignment. *Journal of the American Chemical Society*, 109(18):5541–5542.

[Brewer, 1977] Brewer, W. D. (1977). Review paper:brute-force nuclear orientation: A survey of accomplishments and problems to date. *Journal of Low Temperature Physics*, 27(5-6):651–682.

[Brown and Thompson, 1961] Brown, R. J. and Thompson, D. D. (1961). Second-order effects in low-field nmr for ammonium ion solutions. *The Journal of Chemical Physics*, 34(5):1580–1583.

[Carravetta et al., 2004] Carravetta, M., Johannessen, O. G., and Levitt, M. H. (2004). Beyond the t 1 limit: singlet nuclear spin states in low magnetic fields. *Physical review letters*, 92(15):153003.

[Carravetta and Levitt, 2004] Carravetta, M. and Levitt, M. H. (2004). Long-lived nuclear spin states in high-field solution nmr. *Journal of the American Chemical Society*, 126(20):6228–6229.

[Carver and Slichter, 1953] Carver, T. and Slichter, C. (1953). Polarization of nuclear spins in metals. *Physical Review*, 92(1):212.

[Cavadini et al., 2005] Cavadini, S., Dittmer, J., Antonijevic, S., and Bodenhausen, G. (2005). Slow diffusion by singlet state nmr spectroscopy. *Journal of the American Chemical Society*, 127(45):15744–15748.

[Chhem and Brothwell, 2007] Chhem, R. K. and Brothwell, D. R. (2007). *Paleoradiology: imaging mummies and fossils*. Springer Science & Business Media.

[Clarke et al., 2007] Clarke, J., Hatridge, M., and Mößle, M. (2007). Squid-detected magnetic resonance imaging in microtesla fields. *Annu. Rev. Biomed. Eng.*, 9:389–413.

[Colpa et al., 1980] Colpa, J., Stehlik, D., and Vieth, H. (1980). Radio frequency (rf-) saturation spectroscopy as detected via optical nuclear polarization, mechanisms due to esr and nmr transitions in excited triplet states. *Chemical Physics*, 47(1):73–85.

[Cowley et al., 2011] Cowley, M. J., Adams, R. W., Atkinson, K. D., Cockett, M. C., Duckett, S. B., Green, G. G., Lohman, J. A., Kerssebaum, R., Kilgour, D., and Mewis, R. E. (2011). Iridium n-heterocyclic carbene complexes as efficient catalysts for magnetization transfer from para-hydrogen. *Journal of the American Chemical Society*, 133(16):6134–6137.

[Davis et al., 1998] Davis, T. L., Kwong, K. K., Weisskoff, R. M., and Rosen, B. R. (1998). Calibrated functional mri: mapping the dynamics of oxidative metabolism. *Proceedings of the National Academy of Sciences*, 95(4):1834–1839.

[Dong et al., 2010] Dong, H., Zhang, Y., Krause, H.-J., Xie, X., Braginski, A., and Offenhäusser, A. (2010). Comparison of different detectors in low field nmr measurements. In *Journal of Physics: Conference Series*, volume 234, page 042008. IOP Publishing.

[Eisenschmid et al., 1987] Eisenschmid, T. C., Kirss, R. U., Deutsch, P. P., Hommeltoft, S. I., Eisenberg, R., Bargon, J., Lawler, R. G., and Balch, A. L. (1987). Para hydrogen induced polarization in hydrogenation reactions. *Journal of the American Chemical Society*, 109(26):8089–8091.

[Falk and Gibson, 2001] Falk, D. and Gibson, K. R. (2001). *Evolutionary anatomy of the primate cerebral cortex*. Cambridge University Press.

[Farkas, 1935] Farkas, A. (1935). Orthohydrogen, parahydrogen and heavy hydrogen.

[Fekete et al., 2013] Fekete, M., Bayfield, O., Duckett, S. B., Hart, S., Mewis, R. E., Pridmore, N., Rayner, P. J., and Whitwood, A. (2013). Iridium (iii) hydrido n-heterocyclic carbene–phosphine complexes as catalysts in magnetization transfer reactions. *Inorganic chemistry*, 52(23):13453–13461.

[Ferreira and Kaiser, 2012] Ferreira, S. B. and Kaiser, C. R. (2012). Pyrazine derivatives: a patent review (2008-present). *Expert opinion on therapeutic patents*, 22(9):1033–1051.

[Frangioni, 2008] Frangioni, J. V. (2008). New technologies for human cancer imaging. *Journal of clinical oncology*, 26(24):4012–4021.

[Franken and Colegrove, 1958] Franken, P. and Colegrove, F. (1958). Alignment of metastable helium atoms by unpolarized resonance radiation. *Physical Review Letters*, 1(9):316.

[Golman et al., 2002] Golman, K., Ardenkjær-Larsen, J.-H., Svensson, J., Axelsson, O., Hansson, G., Hansson, L., Jóhannesson, H., Leunbach, I., Månsson, S., Petersson, J. S., et al. (2002). ¡ sup¿ 13¡/sup¿ c-angiography. *Academic Radiology*, 9(2):S507–S510.

[Golman et al., 2001] Golman, K., Axelsson, O., Jóhannesson, H., Månsson, S., Olofsson, C., and Petersson, J. (2001). Parahydrogen-induced polar-

ization in imaging: Subsecond 13c angiography. *Magnetic resonance in medicine*, 46(1):1–5.

[Golman et al., 2006a] Golman, K., Lerche, M., Pehrson, R., Ardenkjaer-Larsen, J. H., et al. (2006a). Metabolic imaging by hyperpolarized 13c magnetic resonance imaging for in vivo tumor diagnosis. *Cancer research*, 66(22):10855–10860.

[Golman et al., 2003] Golman, K., Olsson, L., Axelsson, O., Månsson, S., Karlsson, M., and Petersson, J. (2003). Molecular imaging using hyperpolarized 13c.

[Golman et al., 2006b] Golman, K., Thaning, M., et al. (2006b). Real-time metabolic imaging. *Proceedings of the National Academy of Sciences*, 103(30):11270–11275.

[Green et al., 2012] Green, R. A., Adams, R. W., Duckett, S. B., Mewis, R. E., Williamson, D. C., and Green, G. G. (2012). The theory and practice of hyperpolarization in magnetic resonance using parahydrogen. *Progress in nuclear magnetic resonance spectroscopy*, 67:1–48.

[Halse, 2006] Halse, M. (2006). Terranova-mri efnmr student guide. *Magritek Limited (New Zealand)*.

[Harel et al., 2008] Harel, E., Schröder, L., and Xu, S. (2008). Novel detection schemes of nuclear magnetic resonance and magnetic resonance imaging: applications from analytical chemistry to molecular sensors. *Annu. Rev. Anal. Chem.*, 1:133–163.

[Harkness and Deming, 1932] Harkness, R. W. and Deming, W. E. (1932). The equilibrium of para and ortho hydrogen. *Journal of the American Chemical Society*, 54(7):2850–2852.

[Hausser and Stehlik, 1968] Hausser, K. and Stehlik, D. (1968). Dynamic nuclear polarization in liquids. *Adv. Magn. Reson*, 3:79–139.

[Hennessy, 2005] Hennessy, M. (2005). Industrial applications of magnetic resonance. In *Materials Processing in Magnetic Fields*, volume 1, pages 347–351.

[Hills, 1995] Hills, B. (1995). Food processing: An mri perspective. *Trends in Food Science & Technology*, 6(4):111–117.

[Hirsch et al., 2015] Hirsch, M. L., Kalechofsky, N., Belzer, A., Rosay, M., and Kempf, J. G. (2015). Brute-force hyperpolarization for nmr and mri. *Journal of the American Chemical Society*, 137(26):8428–8434.

[Hopkins and Rilling, 2000] Hopkins, W. D. and Rilling, J. K. (2000). A comparative mri study of the relationship between neuroanatomical asymmetry and interhemispheric connectivity in primates: implication for the evolution of functional asymmetries. *Behavioral neuroscience*, 114(4):739.

[Hovav et al., 2012] Hovav, Y., Levinkron, O., Feintuch, A., and Vega, S. (2012). Theoretical aspects of dynamic nuclear polarization in the solid state: the influence of high radical concentrations on the solid effect and cross effect mechanisms. *Applied Magnetic Resonance*, 43(1-2):21–41.

[Hovener et al., 2014] Hovener, J.-B., Schwaderlapp, N., Borowiak, R., Lickert, T., Duckett, S. B., Mewis, R. E., Adams, R. W., Burns, M. J., Highton, L. A., Green, G. G., et al. (2014). Toward biocompatible nuclear hyperpolarization using signal amplification by reversible exchange: Quantitative in situ spectroscopy and high-field imaging. *Analytical chemistry*, 86(3):1767–1774.

[Hwang and Hill, 1967] Hwang, C. F. and Hill, D. A. (1967). Phenomenological model for the new effect in dynamic polarization. *Physical Review Letters*, 19(18):1011.

[Inglis et al., 2013] Inglis, B., Buckenmaier, K., SanGiorgio, P., Pedersen, A. F., Nichols, M. A., and Clarke, J. (2013). Mri of the human brain at 130 microtesla. *Proceedings of the National Academy of Sciences*, 110(48):19194–19201.

[Jeffries, 1957] Jeffries, C. (1957). Polarization of nuclei by resonance saturation in paramagnetic crystals. *Physical Review*, 106(1):164.

[Kalgutkar et al., 2005] Kalgutkar, A. S., Gardner, I., Obach, R. S., Shaffer, C. L., Callegari, E., Henne, K. R., Mutlib, A. E., Dalvie, D. K., Lee, J. S.,

Nakai, Y., et al. (2005). A comprehensive listing of bioactivation pathways of organic functional groups. *Current drug metabolism*, 6(3):161–225.

[Kessenikh et al., 1963] Kessenikh, A., Lushchikov, V., Manenkov, A., and Taran, Y. V. (1963). Proton polarization in irradiated polyethylenes. *Soviet Phys.-Solid State (English Transl.)*, 5.

[Kleinman, 1997] Kleinman, A. (1997). *Writing at the margin: Discourse between anthropology and medicine*. Univ of California Press.

[Koukourakis et al., 2005] Koukourakis, M. I., Giatromanolaki, A., Sivridis, E., Gatter, K. C., Harris, A. L., Tumor, Group, A. R., et al. (2005). Pyruvate dehydrogenase and pyruvate dehydrogenase kinase expression in non small cell lung cancer and tumor-associated stroma. *Neoplasia*, 7(1):1–6.

[Kraus Jr et al., 2014] Kraus Jr, R., Espy, M., Magnelind, P., and Volegov, P. (2014). *Ultra-Low Field Nuclear Magnetic Resonance: A New MRI Regime*. Oxford University Press.

[Kurhanewicz et al., 2011] Kurhanewicz, J., Vigneron, D. B., Brindle, K., Chekmenev, E. Y., Comment, A., Cunningham, C. H., DeBerardinis, R. J., Green, G. G., Leach, M. O., Rajan, S. S., et al. (2011). Analysis of cancer metabolism by imaging hyperpolarized nuclei: prospects for translation to clinical research. *Neoplasia*, 13(2):81–97.

[Lauterbur et al., 1973] Lauterbur, P. C. et al. (1973). Image formation by induced local interactions: examples employing nuclear magnetic resonance. *Nature*, 242(5394):190–191.

[Leawoods et al., 2001] Leawoods, J. C., Yablonskiy, D. A., Saam, B., Gierada, D. S., and Conradi, M. S. (2001). Hyperpolarized 3he gas production and mr imaging of the lung. *Concepts in Magnetic Resonance*, 13(5):277–293.

[Ledbetter et al., 2009] Ledbetter, M., Crawford, C., Pines, A., Wemmer, D., Knappe, S., Kitching, J., and Budker, D. (2009). Optical detection of nmr j-spectra at zero magnetic field. *Journal of Magnetic Resonance*, 199(1):25–29.

[Lee and Cho, 1984] Lee, S. and Cho, Z. (1984). Limited angular view planar-integral projection reconstruction in nmr imaging. *Nuclear Science, IEEE Transactions on*, 31(4):974–982.

[Legchenko et al., 2002] Legchenko, A., Baltassat, J.-M., Beauce, A., and Bernard, J. (2002). Nuclear magnetic resonance as a geophysical tool for hydrogeologists. *Journal of Applied Geophysics*, 50(1):21–46.

[Levitt, 2008] Levitt, M. H. (2008). *Spin dynamics: basics of nuclear magnetic resonance*. John Wiley & Sons.

[Levitt, 2010] Levitt, M. H. (2010). Singlet and other states with extended lifetimes. *eMagRes*.

[Lloyd et al., 2014] Lloyd, L. S., Asghar, A., Burns, M. J., Charlton, A., Coombes, S., Cowley, M. J., Dear, G. J., Duckett, S. B., Genov, G. R., Green, G. G., et al. (2014). Hyperpolarisation through reversible interactions with para hydrogen. *Catalysis Science & Technology*, 4(10):3544–3554.

[Maly et al., 2008] Maly, T., Debelouchina, G. T., Bajaj, V. S., Hu, K.-N., Joo, C.-G., Mak-Jurkauskas, M. L., Sirigiri, J. R., van der Wel, P. C., Herzfeld, J., Temkin, R. J., et al. (2008). Dynamic nuclear polarization at high magnetic fields. *The Journal of chemical physics*, 128(5):052211.

[Månsson, 2002] Månsson, S. (2002). *Hyperpolarized Nuclei for NMR Imaging and Spectroscopy–Methodology and model studies of lung and vascular function*. PhD thesis, Lund University.

[Matlachov et al., 2004] Matlachov, A. N., Volegov, P. L., Espy, M. A., George, J. S., and Kraus Jr, R. H. (2004). Squid detected nmr in microtesla magnetic fields. *Journal of Magnetic Resonance*, 170(1):1–7.

[McDermott et al., 2004] McDermott, R., Lee, S., Ten Haken, B., Trabesinger, A. H., Pines, A., and Clarke, J. (2004). Microtesla mri with a superconducting quantum interference device. *Proceedings of the National Academy of Sciences of the United States of America*, 101(21):7857–7861.

[McDermott et al., 2002] McDermott, R., Trabesinger, A. H., Mück, M., Hahn, E. L., Pines, A., and Clarke, J. (2002). Liquid-state nmr and scalar couplings in microtesla magnetic fields. *Science*, 295(5563):2247–2249.

[Merck et al., 1967] Merck, M., Sechehaye, R., Erbeia, A., and Béné, G. (1967). Free precession experiments in terrestrial magnetic field. *Magnetic Resonance and Relaxation, North-Holland Publishing Company, Amsterdam*, pages 952–956.

[Mewis, 2015] Mewis, R. E. (2015). Developments and advances concerning the hyperpolarisation technique sabre. *Magnetic Resonance in Chemistry*, 53(10):789–800.

[Mewis et al., 2014] Mewis, R. E., Atkinson, K. D., Cowley, M. J., Duckett, S. B., Green, G. G., Green, R. A., Highton, L. A., Kilgour, D., Lloyd, L. S., Lohman, J. A., et al. (2014). Probing signal amplification by reversible exchange using an nmr flow system. *Magnetic Resonance in Chemistry*, 52(7):358–369.

[Michal, 2010] Michal, C. A. (2010). A low-cost spectrometer for nmr measurements in the earth's magnetic field. *Measurement Science and Technology*, 21(10):105902.

[Mohorič et al., 2004] Mohorič, A., Planinšič, G., Kos, M., Duh, A., and Stepišnik, J. (2004). Magnetic resonance imaging system based on earth's magnetic field. *Instrumentation science & technology*, 32(6):655–667.

[Morris and Freeman, 1979] Morris, G. A. and Freeman, R. (1979). Enhancement of nuclear magnetic resonance signals by polarization transfer. *Journal of the American Chemical Society*, 101(3):760–762.

[Myers et al., 2007] Myers, W., Slichter, D., Hatridge, M., Busch, S., Mößle, M., McDermott, R., Trabesinger, A., and Clarke, J. (2007). Calculated signal-to-noise ratio of mri detected with squids and faraday detectors in fields from 10$\mu$t to 1.5 t. *Journal of Magnetic Resonance*, 186(2):182–192.

[Nalcioglu and Cho, 1984] Nalcioglu, O. and Cho, Z. (1984). Limits to signal-to-noise improvement by fid averaging in nmr imaging. *Physics in medicine and biology*, 29(8):969.

[Natterer and Bargon, 1997] Natterer, J. and Bargon, J. (1997). Parahydrogen induced polarization. *Progress in Nuclear Magnetic Resonance Spectroscopy*, 31(4):293–315.

[Nelson et al., 2012] Nelson, S. J., Kurhanewicz, J., Vigneron, D. B., Larson, P., Harzstarck, A., Ferrone, M., van Criekinge, M., Chang, J., Bok, R., Park, I., et al. (2012). Proof of concept clinical trial of hyperpolarized c-13 pyruvate in patients with prostate cancer. In *Proceedings of the 20th Annual Meeting of ISMRM*, volume 274.

[Nieminen et al., 2011] Nieminen, J. O., Vesanen, P. T., Zevenhoven, K. C., Dabek, J., Hassel, J., Luomahaara, J., Penttilä, J. S., and Ilmoniemi, R. J. (2011). Avoiding eddy-current problems in ultra-low-field mri with self-shielded polarizing coils. *Journal of Magnetic Resonance*, 212(1):154–160.

[Norquay et al., 2013] Norquay, G., Parnell, S. R., Xu, X., Parra-Robles, J., and Wild, J. M. (2013). Optimized production of hyperpolarized 129xe at 2 bars for in vivo lung magnetic resonance imaging. *Journal of Applied Physics*, 113(4):044908.

[Olaru et al., 2016] Olaru, A. M., Roy, S. S., Lloyd, L. S., Coombes, S., Green, G. G., and Duckett, S. B. (2016). Creating a hyperpolarised pseudo singlet state through polarisation transfer from para hydrogen under sabre. *Chemical Communications*.

[Oros and Shah, 2004] Oros, A.-M. and Shah, N. J. (2004). Hyperpolarized xenon in nmr and mri. *Physics in medicine and biology*, 49(20):R105.

[Overhauser, 1953] Overhauser, A. W. (1953). Polarization of nuclei in metals. *Physical Review*, 92(2):411.

[Owers-Bradley et al., 2013] Owers-Bradley, J. R., Horsewill, A. J., Peat, D. T., Goh, K. S., and Gadian, D. G. (2013). High polarization of nuclear spins mediated by nanoparticles at millikelvin temperatures. *Physical Chemistry Chemical Physics*, 15(25):10413–10417.

[Packard and Varian, 1954] Packard, M. and Varian, R. (1954). Free nuclear induction in the earths magnetic field. In *Physical Review*, volume 93, pages 941–941. AMERICAN PHYSICAL SOC ONE PHYSICS ELLIPSE, COLLEGE PK, MD 20740-3844 USA.

[Pellegatti et al., 2008] Pellegatti, P., Raffaghello, L., Bianchi, G., Piccardi, F., Pistoia, V., and Di Virgilio, F. (2008). Increased level of extracellular

atp at tumor sites: in vivo imaging with plasma membrane luciferase. *PLoS One*, 3(7):e2599.

[Pieroni et al., 2014] Pieroni, M., Wan, B., Cho, S., Franzblau, S. G., and Costantino, G. (2014). Design, synthesis and investigation on the structure–activity relationships of n-substituted 2-aminothiazole derivatives as anti-tubercular agents. *European journal of medicinal chemistry*, 72:26–34.

[Pileio et al., 2013] Pileio, G., Bowen, S., Laustsen, C., Tayler, M. C., Hill-Cousins, J. T., Brown, L. J., Brown, R. C., Ardenkjaer-Larsen, J. H., and Levitt, M. H. (2013). Recycling and imaging of nuclear singlet hyperpolarization. *Journal of the American Chemical Society*, 135(13):5084–5088.

[Pileio et al., 2008] Pileio, G., Carravetta, M., Hughes, E., and Levitt, M. H. (2008). The long-lived nuclear singlet state of 15n-nitrous oxide in solution. *Journal of the American Chemical Society*, 130(38):12582–12583.

[Pravica and Weitekamp, 1988] Pravica, M. G. and Weitekamp, D. P. (1988). Net nmr alignment by adiabatic transport of parahydrogen addition products to high magnetic field. *Chemical physics letters*, 145(4):255–258.

[Prisner and Koeckenberger, 2008] Prisner, T. and Koeckenberger, W. (2008). Dynamic nuclear polarization: new experimental and methodology approaches and applications in physics, chemistry, biology and medicine. *Applied Magnetic Resonance*, 34(3):213–218.

[Purcell et al., 1946] Purcell, E. M., Torrey, H., and Pound, R. V. (1946). Resonance absorption by nuclear magnetic moments in a solid. *Physical review*, 69(1-2):37.

[Ramadan et al., 1998] Ramadan, U. A., Markkola, A. T., Halavaara, J., Tanttu, J., Häkkinen, A.-M., and Aronen, H. J. (1998). On-and off-resonance spin-lock mr imaging of normal human brain at 0.1 t: possibilities to modify image contrast. *Magnetic resonance imaging*, 16(10):1191–1199.

[Roberts and Dabbs, 1961] Roberts, L. D. and Dabbs, J. (1961). Nuclear orientation. *Annual review of nuclear science*, 11(1):175–212.

[Robinson et al., 2006] Robinson, J. N., Coy, A., Dykstra, R., Eccles, C. D., Hunter, M. W., and Callaghan, P. T. (2006). Two-dimensional nmr

spectroscopy in earths magnetic field. *Journal of Magnetic Resonance*, 182(2):343–347.

[Rossini et al., 2013] Rossini, A. J., Zagdoun, A., Lelli, M., Lesage, A., Copéret, C., and Emsley, L. (2013). Dynamic nuclear polarization surface enhanced nmr spectroscopy. *Accounts of chemical research*, 46(9):1942–1951.

[Rovedo et al., 2016] Rovedo, P., Knecht, S., Bäumlisberger, T., Cremer, A. L., Duckett, S. B., Mewis, R. E., Green, G. G., Burns, M. J., Rayner, P. J., Leibfritz, D., et al. (2016). Molecular mri in the earth's magnetic field using continuous hyperpolarization of a biomolecule in water. *The Journal of Physical Chemistry B*.

[Roy et al., 2016a] Roy, S. S., Norcott, P., Rayner, P. J., Green, G. G., and Duckett, S. B. (2016a). A hyperpolarizable 1h magnetic resonance probe for signal detection 15 minutes after spin polarization storage. *Angewandte Chemie International Edition*, 55(50):15642–15645.

[Roy et al., 2016b] Roy, S. S., Rayner, P. J., Norcott, P., Green, G. G., and Duckett, S. B. (2016b). Long-lived states to sustain sabre hyperpolarised magnetisation. *Physical Chemistry Chemical Physics*, 18(36):24905–24911.

[Sarkar et al., 2008] Sarkar, R., Ahuja, P., Vasos, P. R., and Bodenhausen, G. (2008). Measurement of slow diffusion coefficients of molecules with arbitrary scalar couplings via long-lived spin states. *ChemPhysChem*, 9(16):2414–2419.

[Sarkar et al., 2007] Sarkar, R., Vasos, P. R., and Bodenhausen, G. (2007). Singlet-state exchange nmr spectroscopy for the study of very slow dynamic processes. *Journal of the American Chemical Society*, 129(2):328–334.

[Shchepin et al., 2016] Shchepin, R. V., Barskiy, D. A., Mikhaylov, D. M., and Chekmenev, E. Y. (2016). Efficient synthesis of nicotinamide-1-15n for ultrafast nmr hyperpolarization using parahydrogen. *Bioconjugate chemistry*, 27(4):878–882.

[Spannring et al., 2016] Spannring, P., Reile, I., Emondts, M., Schleker, P. P., Hermkens, N. K., van der Zwaluw, N. G., van Weerdenburg, B. J., Tinnemans, P., Tessari, M., Blümich, B., et al. (2016). A new ir-nhc catalyst for

signal amplification by reversible exchange in d2o. *Chemistry-A European Journal*, 22(27):9277–9282.

[Tayler and Levitt, 2011] Tayler, M. C. and Levitt, M. H. (2011). Singlet nuclear magnetic resonance of nearly-equivalent spins. *Physical Chemistry Chemical Physics*, 13(13):5556–5560.

[Tayler et al., 2010] Tayler, M. C., Marie, S., Ganesan, A., and Levitt, M. H. (2010). Determination of molecular torsion angles using nuclear singlet relaxation. *Journal of the American Chemical Society*, 132(24):8225–8227.

[Tayler et al., 2016] Tayler, M. C., Sjolander, T. F., Pines, A., and Budker, D. (2016). Nuclear magnetic resonance at millitesla fields using a zero-field spectrometer. *Journal of Magnetic Resonance*.

[Thompson and Brown, 1962] Thompson, D. D. and Brown, R. J. (1962). Note on the earth's field proton free-precession signal of fluorobenzene. *The Journal of Chemical Physics*, 36(10):2812–2812.

[Thompson et al., 1964a] Thompson, D. D., Brown, R. J., and Bloom, M. (1964a). Nuclear free precession in very low magnetic fields. *The Journal of Chemical Physics*, 40(10):3076–3079.

[Thompson et al., 1964b] Thompson, D. D., Brown, R. J., and Runge, R. J. (1964b). Dynamic nuclear polarization of liquids in very weak fields. *Physical Review*, 136(5A):A1286.

[van Beek et al., 2004] van Beek, E. J., Wild, J. M., Kauczor, H.-U., Schreiber, W., Mugler, J. P., and de Lange, E. E. (2004). Functional mri of the lung using hyperpolarized 3-helium gas. *Journal of Magnetic Resonance Imaging*, 20(4):540–554.

[Vasos et al., 2009] Vasos, P., Comment, A., Sarkar, R., Ahuja, P., Jannin, S., Ansermet, J.-P., Konter, J., Hautle, P., Van den Brandt, B., and Bodenhausen, G. (2009). Long-lived states to sustain hyperpolarized magnetization. *Proceedings of the National Academy of Sciences*, 106(44):18469–18473.

[Vazquez-Serrano et al., 2006] Vazquez-Serrano, L. D., Owens, B. T., and Buriak, J. M. (2006). The search for new hydrogenation catalyst motifs based on n-heterocyclic carbene ligands. *Inorganica chimica acta*, 359(9):2786–2797.

[Viale and Aime, 2010] Viale, A. and Aime, S. (2010). Current concepts on hyperpolarized molecules in mri. *Current opinion in chemical biology*, 14(1):90–96.

[Warren et al., 2009] Warren, W. S., Jenista, E., Branca, R. T., and Chen, X. (2009). Increasing hyperpolarized spin lifetimes through true singlet eigenstates. *Science*, 323(5922):1711–1714.

[Westbrook and Roth, 2013] Westbrook, C. and Roth, C. K. (2013). *MRI in Practice*. John Wiley & Sons.

[Wild et al., 2003] Wild, J. M., Paley, M. N., Kasuboski, L., Swift, A., Fichele, S., Woodhouse, N., Griffiths, P. D., and van Beek, E. J. (2003). Dynamic radial projection mri of inhaled hyperpolarized 3he gas. *Magnetic resonance in medicine*, 49(6):991–997.

[Wild et al., 2002] Wild, J. M., Paley, M. N., Viallon, M., Schreiber, W. G., van Beek, E. J., and Griffiths, P. D. (2002). k-space filtering in 2d gradient-echo breath-hold hyperpolarized 3he mri: spatial resolution and signal-to-noise ratio considerations. *Magnetic resonance in medicine*, 47(4):687–695.

[Zotev et al., 2007] Zotev, V. S., Matlachov, A. N., Volegov, P. L., Sandin, H. J., Espy, M. A., Mosher, J. C., Urbaitis, A. V., Newman, S. G., and Kraus, R. H. (2007). Multi-channel squid system for meg and ultra-low-field mri. *Applied Superconductivity, IEEE Transactions on*, 17(2):839–842.

[Zotev et al., 2008] Zotev, V. S., Matlashov, A. N., Volegov, P. L., Savukov, I. M., Espy, M. A., Mosher, J. C., Gomez, J. J., and Kraus Jr, R. H. (2008). Microtesla mri of the human brain combined with meg. *Journal of Magnetic Resonance*, 194(1):115–120.